

THESIS FOR THE DEGREE OF DOCTOR OF PHILOSOPHY

Shape Control Synthesis and Microstructure Studies of Metal  
Nanoparticles

XIN WEN



**CHALMERS**  
UNIVERSITY OF TECHNOLOGY

Department of Chemistry and Chemical Engineering

CHALMERS UNIVERSITY OF TECHNOLOGY

Gothenburg, Sweden 2020

# Shape Control Synthesis and Microstructure Studies of Metal Nanoparticles

XIN WEN

ISBN 978-91-7905-387-1

© XIN WEN, 2020.

Doktorsavhandlingar vid Chalmers tekniska högskola

Ny serie nr 4854

ISSN 0346-718X

Department of Chemistry and Chemical Engineering

Division of Applied Chemistry

Chalmers University of Technology

SE-412 96 Gothenburg

Sweden

Telephone + 46 (0)31-772 1000

Cover:

[Metal nanoparticles synthesized with colloidal-chemical synthesis methods and characterized with transmission electron microscopy]

Printed by Chalmers Reproservice

Gothenburg, Sweden 2020

# Abstract

Shape Control Synthesis and Microstructure Studies of Metal Nanoparticles

Xin Wen

Department of Chemistry and Chemical Engineering

Chalmers University of Technology

Gothenburg, Sweden

Metal nanoparticles have been extensively studied in recent years due to their unique chemical, biological and physical properties. Gold (Au) and palladium (Pd) nanoparticles are two of the most popular materials because Au nanoparticles have a strong localized surface plasmon resonance effect and Pd nanoparticles have high hydrogen adsorption and chemical catalytic capacities. In the colloidal-chemical synthesis of gold (Au) and palladium (Pd) nanoparticles, capping agents are widely used to control the shape and size of nanoparticles. Capping agents are usually surfactants, polymers, organic ligands and dendrimers. In this work, an anionic surfactant, sodium oleate (NaOL) was mixed with common capping agents such as hexadecyltrimethylammonium bromide (CTAB), hexadecyltrimethylammonium chloride (CTAC) and polyvinylpyrrolidone (PVP) in order to tune the shapes of nanoparticles. Three mixtures of capping agent: CTAB-NaOL, CTAC-NaOL, and PVP-NaOL were applied to the synthesis of Pd nanoparticles, resulting in the formation of Pd nanodendrites under proper circumstances including temperature, pH value and ratio between the capping agents. The large surface area makes Pd nanodendrites advantageous in catalytic applications. However, the application of CTAB-NaOL mixture in the growth of Au nanorods plays a remarkably different role. It increased the rod-shape yield and narrowed the aspect ratio of Au nanorods. A growth-induced strain was discovered in the Au nanorods, leading to slight bending in a large percentage ( $\approx 47\%$ ) of the Au nanorods.

A variety of techniques were used to investigate the microstructure and properties of Au and Pd nanoparticles. Transmission electron microscopy including selected area electron diffraction and Kikuchi pattern methods, energy dispersive X-ray spectroscopy, and scanning transmission electron microscopy were employed to study microstructure and elemental composition. Ultraviolet-visible spectroscopy, dynamic light scattering and conductivity measurements were used to characterize the growth kinetics of metal nanoparticles. Through these techniques, the effects of the capping agent ratio, pH value and precursor types on the growth of Pd nanodendrites were investigated. Additionally, the growth-induced strain in Au nanorods was studied as well. Investigations of the shapes and microstructure of metal nanoparticles have the potential to expand their applications in the fields of surface plasmonic sensing and catalysis.

**Keyword:** Gold nanorod, palladium nanodendrite, transmission electron microscopy, seed mediated growth, hexadecyltrimethylammonium bromide, hexadecyltrimethylammonium chloride, polyvinylpyrrolidone, sodium oleate.

# Acknowledgement

The finalisation of this thesis is one of the most impressed moments during my PhD studies because it is a conclusion of all the exploration, study and progress for the last four years. During these four years I have lots of fun and also challenges. I am lucky to be helped and supported very much by supervisors, colleagues, friends and families. Their help and companies encourage me to overcome difficulties and keep optimistic.

First, I would like to express my sincere gratitude to my supervisor, Prof. Kasper Moth-Poulsen, who has continuously supported me during the whole PhD period. I really appreciate that you gave me the chance to join your group and start the amazing PhD journey in Sweden. Your guidance, knowledge and patience helped me in all the time of research and writing of this thesis. You set a good example for me to be an excellent researcher. Besides main supervisor, I would like to thank my co-supervisor, Prof. Eva Olsson, for all her guidance on my studies in these four years. Your immense knowledge and plentiful experience provide me many precious advices. I really enjoyed the time when we discussed about work and also had fun in your group activities. I also would like to thank my third supervisor, Dr. Sarah Lerch. You gave me very practical suggestions not only on the experiments but also other problems which commonly happen on PhD students. You always have methods to cheer me up when I am frustrated. I also would like to express my thanks to my examiner, Prof. Martin Andersson, for your precious advices on my projects and assistances in keeping my PhD progress.

Thanks to my work mates in Kasper's groups for all your help and companies, especially Zhihang Wang, Jessica Orrego Hernandez, and the nano team members: Robson Rosa Da Silva, Alicja Stolas and Anna Pekkari. I am very happy to work with you all and share the happiness on both work and life. There are lots of good memories in the lab, lunchroom and office, which make the research work much fun. I also need to thank our administrator Lotta Pettersson. You are kind and nice to us. No matter what questions I asked, you always answer them patiently. You also encourage me to express myself bravely. You are the best administrator I know. I would like to give my thanks to all colleague in Applied Chemistry on 8th Floor for all your kindness. Additionally, I would also like to express my gratitude to all colleagues in Eva's group and Research Engineer Stefan Gustafsson and Ludvig De Knoop for the help on electron microscopy. I also really enjoy the activities together with you all. My thanks also go to all my collaborators for your work and time on the projects.

In addition, I would like to express my sincere gratitude to my friends Zhaojun Li and Gaowa Naren. It is my honor to meet you both in Sweden. Thanks for being the ones I can always rely on. You are not only good friends in life but also great

partners for the adventure of PhD. There are also many friends who are getting along with me for a short time, but you make my life more colorful during the last four years. Thanks for your showing up and sharing the happiness with me.

I would like to thank my boyfriend Jonathan Johansson. It is my luck to meet you at a proper time in a proper place. Thanks for your understanding and supporting on my work. I'm so grateful that you're in my life.

At last, I would express my deepest appreciation for my parents. Thanks for your cultivation and constantly supports, which encourage me to go ahead. You are always the happiest for my happiness and the strongest shield for me when I feel frustrated. I love you and wish you to be happy and healthy all the time. (我要向我的父母表达我最深切的感谢。感谢你们的培养和一直以来的支持，这些给了我前进的勇气。你们总是在我幸福时最为我开心的人，也是我失意时最坚实的后盾。我爱你们，希望你们永远健康快乐！)

# Publications and Manuscripts

Following papers are included in this thesis:

- Paper I**      **Synthesis of Palladium Nanodendrites Using a Mixture of Cationic and Anionic Surfactants**  
Xin Wen, Sarah Lerch, Zhihang Wang, Bassem Aboudiab, Ali Reza Tehrani-Bagha, Eva Olsson, Kasper Moth-Poulsen. *Langmuir*, 2020, 36, 7, 1745-1753.
- Paper II**      **Growth-Induced Strain in Single Crystal Gold Nanorods**  
Xin Wen, Torben Nilsson Pingel, Lunjie Zeng, Gabriel Sanchez-Santolino, Shun Kondo, Nestor Zaluzec, Naoya Shibata, Yuichi Ikuhara, Sarah Lerch, Kasper Moth-Poulsen, Eva Olsson. *Manuscript*.
- Paper III**      **The Effect of the Pd Precursors on the Shape of Ag-Pd Alloy Nanoparticles Using Ag Nanocubes as Seeds**  
Xin Wen, Seyed Amirabbas Nazemi, Robson Rosa da Silva, Kasper Moth-Poulsen. *Manuscript*.
- Paper IV**      **Performance of Palladium Nanodendrites Stabilized by Polyvinylpyrrolidone and Sodium Oleate in Sonogashira Reactions**  
Xin Wen, Jessica Orrego Hernandez, Sarah Lerch, Alicja Stolas, Eva Olsson, Kasper Moth-Poulsen. *Manuscript*.

My contributions to the appended papers:

- Paper I**      I performed the synthesis of palladium nanodendrites, TEM images and absorbance spectrum. I measured the size, zeta potential and yield of palladium nanoparticles. I wrote the first version of the paper and refined it in collaboration with all authors. The conductance was measured by Bassem Aboudiab. The experiment design, discussion and modification were completed with my co-authors.
- Paper II**      I performed the synthesis of gold nanorods, Kikuchi and diffraction patterns, low magnification TEM images, intensity profiles, absorbance spectra, size and aspect ratio statistics of gold nanorods and part of EDS results. I wrote the manuscript of this paper. The high-resolution STEM image of the entire gold nanorod

was taken by co-authors. EDS mappings were performed by Nestor Zaluzec. Bonding angle calculations and some EDS measurements were performed by Torben Nilsson Pingel and GPA strain distribution was analyzed by Lunjie Zeng. The discussion and modification were done with my co-authors.

**Paper III** I did the EDS measurements and part of the synthesis of Pd nanodendrites. I wrote the manuscript. Absorbance spectrum, part of TEM images and a large part of the synthesis were performed by Seyed Amirabbas Nazemi and Robson Rosa da Silva.

**Paper IV** I performed the synthesis experiments and TEM characterization. I wrote the manuscript. The preliminary catalytic The Sonogashira reaction was performed by Jessica Orrego Hernandez.

### **Publications which are not included in this thesis:**

**Paper A** **Constructing a Library of Metal and Metal-Oxide Nanoparticle Heterodimers through Colloidal Assembly**  
Tina A. Gschneidtner, Sarah Lerch, Erik Olsén, Xin Wen, Amelia C. Y. Liu, Alicja Stolaś, Joanne Etheridge, Eva Olsson, Kasper Moth-Poulsen. *Nanoscale*, 2020,12, 11297–11305.

**Paper B** **Macroscopic Heat Release in a Molecular Solar Thermal Energy Storage System**  
Zhihang Wang, Anna Roffey, Raul Losantos, Anders Lennartson, Martyn Jevric, Anne U. Petersen, Maria Quant, Ambra Dreos, Xin Wen, Diego Sampedro, Karl Börjesson and Kasper Moth-Poulsen. *Energy Environ. Sci.*, 2019, 12, 187-193.

**Paper C** **A Non-Conjugated Polymer Acceptor for Efficient and Thermally Stable All-Polymer Solar Cells**  
Qunping Fan, Wenyan Su, Shanshan Chen, Tao Liu, Wenliu Zhuang, Ruijie Ma, Xin Wen, Zhenghui Luo, Xia Guo, Lintao Hou, Kasper Moth-Poulsen, Yu Li, Changduk Yang, Donghong Yu, He Yan, Maojie Zhang, Ergang Wang. *Angewandte Chemie*, 2020, 132, 20007-20012.

# Nomenclature & Abbreviations

AA	L-ascorbic acid
ADF	Annular dark field
CF <sub>3</sub> COOAg	Silver trifluoroacetate
Ag	Silver
AgNO <sub>3</sub>	Silver nitrate
Au	Gold
bfp	Back focal plane
Br <sup>-</sup>	Bromide ion
CAC	Critical association concentration
CMC	Critical micelle concentration
CPP	Critical packing parameter
CTAB	Hexadecyltrimethylammonium bromide
CTAC	Hexadecyltrimethylammonium chloride
CTA <sup>+</sup>	Hexadecyltrimethylammonium ion
DLS	Dynamic light scattering
EDS	Energy dispersive X-ray spectroscopy
EG	Ethylene glycol
FCC	Face centered cubic
FFT	Fast Fourier transform
GPA	Geometric phase analysis
HAuCl <sub>4</sub>	Hydrogen tetrachloroaurate(III) trihydrate
HCl	Hydrochloric acid
HLB	Hydrophilic-lipophilic balance
HNO <sub>3</sub>	Nitric acid
H <sub>2</sub> PdCl <sub>4</sub>	Dihydrogen tetrachloropalladate(II)
HRSTEM	High-resolution scanning transmission electron microscopy

LSPR	Localized surface plasmon resonance
$M_n$	The number average molecular weight
$M_w$	The weight average molecular weight
$\text{NaBH}_4$	Sodium borohydride
NaHS	Sodium hydrosulfide hydrate
NaOH	Sodium hydroxide
NaOL	Sodium oleate
$\text{Na}_2\text{PdCl}_4$	Sodium tetrachloropalladate(II)
NaST	Sodium stearate
NMR	Nuclear magnetic resonance
$\text{OL}^-$	Oleate ion
Pd or $\text{Pd}^0$	Palladium
$\text{Pd}^{2+}$	Palladium(II) ion
$\text{Pd}(\text{acac})_2$	Palladium(II) acetylacetonate
$\text{PdCl}_2$	Palladium(II) chloride
PVP	Polyvinylpyrrolidone
SAD aperture	Selected-area diffraction aperture
SAED	Selected area electron diffraction
SEM	Scanning electron microscopy
STEM	Scanning transmission electron microscopy
TEM	Transmission electron microscopy
$T_K$	Krafft temperature
UV-Vis spectroscopy	Ultraviolet-visible spectroscopy
$\alpha_{\text{CTAB}}$	The molar ratio of CTAB and the binary surfactant mixture
$\beta$	Interaction parameter

# Contents

<b>Abstract</b> .....	i
<b>Acknowledgement</b> .....	iii
<b>Publications and Manuscripts</b> .....	v
<b>Nomenclature &amp; Abbreviations</b> .....	vii
<b>Chapter 1 Introduction</b> .....	1
1.1 Thesis Outline.....	2
<b>Chapter 2 Noble Metal Nanoparticles</b> .....	5
2.1 Synthesis of Noble Metal Nanoparticles .....	5
2.1.1 Seed-mediated growth method .....	6
<b>2.1.1.1</b> Core-shell metal nanoparticles .....	7
<b>2.1.1.2</b> Hollow metal nanoparticles .....	7
2.1.2 One-step seedless method.....	8
2.1.3 Nucleation and growth theory .....	8
<b>2.1.3.1</b> Classical nucleation theory .....	8
<b>2.1.3.2</b> LaMer’s nucleation theory.....	10
<b>2.1.3.3</b> Other theories .....	11
2.2 Localized Surface Plasmon Resonance .....	12
2.3 Catalytic Properties .....	13
<b>Chapter 3 Capping Agents</b> .....	15
3.1 Structure of Capping Agents .....	15
3.1.1 Structure of surfactants.....	15
3.1.2 Structure of polymers .....	16
3.1.3 Stabilization of nanoparticles by capping agents.....	17
3.1.4 Chemical structures of the applied capping agents.....	18
3.2 Properties of Surfactants.....	19

3.2.1 Critical micelle concentration.....	19
3.2.2 Critical packing parameter.....	19
3.2.3 Krafft temperature .....	21
3.2.4 Hydrophilic-lipophilic balance .....	21
3.3 Properties of Polymers .....	21
3.3.1 Molecular weight.....	21
3.3.2 Cloud point and critical point .....	22
3.3.3 Properties of Polyvinylpyrrolidone .....	22
3.4 Mixture of Two Capping Agents.....	22
3.4.1 Mixture of two surfactants.....	22
3.4.2 Mixture of a surfactant and a polymer.....	24
3.5 Adsorption on Solid Surfaces .....	25
3.5.1 Adsorption of surfactants on solid surfaces.....	25
3.5.2 Adsorption of polymers on solid surfaces .....	26
<b>Chapter 4 Transmission Electron Microscopy Techniques .....</b>	<b>29</b>
4.1 Transmission Electron Microscopy .....	29
4.2 Diffraction and Image Modes.....	29
4.3 Kikuchi Pattern.....	33
4.4 Energy Dispersive X-ray Spectroscopy.....	36
4.5 Scanning Transmission Electron Microscopy .....	38
4.6 Electron Beam Damage .....	38
4.7 Miller Indices.....	38
<b>Chapter 5 Experimental Methods.....</b>	<b>41</b>
5.1 Materials .....	41
5.1.1 Preparation of $\text{H}_2\text{PdCl}_4$ solution .....	41
5.1.2 Preparation of $\text{Pd}(\text{acac})_2$ solution .....	42
5.1.3 Preparation of aqua regia.....	42
5.2 Synthesis of Pd Nanodendrites Stabilized by CTAB and NaOL.....	42

5.2.1 Seed solution .....	42
5.2.2 Growth solution .....	42
5.2.3 Preparation of TEM sample.....	43
5.3 Synthesis of Hollow Ag-Pd Nanoparticles Stabilized by CTAC and NaOL	43
5.3.1 Ag seed solution .....	43
5.3.2 Growth solution of hollow Ag-Pd nanodendrites.....	44
5.3.3 Growth solution of hollow Ag-Pd spiky-nanoboxes .....	44
5.3.4 Preparation of TEM sample.....	44
5.4 Synthesis of Pd Nanodendrites Stabilized by PVP and NaOL .....	45
5.4.1 Preparation of TEM sample.....	45
5.5 Synthesis of Au Nanorods Stabilized by CTAB and NaOL.....	45
5.5.1 Seed solution .....	46
5.5.2 Growth solution .....	46
5.5.3 Preparation of TEM sample.....	46
5.6 Characterization.....	47
5.6.1 Transmission electron microscopy .....	47
5.6.2 Ultraviolet-visible spectroscopy .....	47
5.6.3 Dynamic light scattering and zeta potential measurements.....	47
<b>Chapter 6 Effects of Surfactant Ratios on the Growth of Pd Nanoparticles</b> .	<b>49</b>
<b>Chapter 7 Effects of Seeds and Precursors on the Growth of Pd Nanoparticles</b>	<b>61</b>
<b>Chapter 8 Effects of pH on the Growth of Pd Nanoparticles</b> .....	<b>67</b>
<b>Chapter 9 Growth-Induced Strain in Au Nanorods</b> .....	<b>71</b>
<b>Chapter 10 Discussion and Conclusions</b> .....	<b>81</b>
<b>References</b> .....	<b>85</b>



# Chapter 1 Introduction

In 1856, English scientist Michael Faraday created a ruby red colloidal gold solution in a basement laboratory of the Royal Institution, which is considered as the starting of modern nanomaterial science<sup>1-2</sup>. In the past 160 years, nanotechnology has developed rapidly. Nowadays, noble metal nanoparticles can be synthesized through various routes such as electron beam lithography, nano-templating, atomic layer deposition, laser ablation and colloidal-chemical synthesis<sup>3-7</sup>. The size of these metal nanoparticles is controllable and a variety of shapes are created. These noble metal nanoparticles are widely used in both scientific research and industrial fields because they have special optical, electrical, chemical and magnetic properties compared to their corresponding bulk materials, making them potential candidates for applications in biological, physical and chemical fields<sup>8</sup>.

Gold (Au) is one of the most popular metal materials. Au nanoparticles have strong absorption of light at certain wavelengths, known as the localized surface plasmon resonance (LSPR)<sup>9</sup>. The absorption wavelength is related to the shape and size of the Au nanoparticles<sup>9</sup>. Based on the property of LSPR, Au nanoparticles can be used for optical sensing, photothermal activation of chemical reactions and photothermal drug release<sup>10-11</sup>. Another popular material is palladium (Pd). Pd nanoparticles have not only high absorption capacity of hydrogen gas but also unique chemical catalytic properties for cross coupling, asymmetric synthesis and alkylation reactions<sup>12-13</sup>. Therefore, they can be used for hydrogen sensing, or as hydrogen storage materials and catalysts of organic synthesis including Sonogashira, Stille, Heck and Suzuki–Miyaura reactions<sup>14-15</sup>. Therefore, a variety of research focuses on the synthesis and applications of Au and Pd nanoparticles.

Even though many studies have been done, the further exploration of new shapes of Au and Pd nanoparticles to optimize material function and meet diversified applications is still in highly demand. This is because the catalytic, optical and electromagnetic properties of nanoparticles are strongly influenced by their size, shape and surface morphology<sup>16-17</sup>. For example, Au nanorods have a longitudinal absorption band and a transverse absorption band of light due to surface plasmon resonance, while Au nanospheres have only one absorption band, demonstrating the importance of the shape for LSPR based techniques<sup>18</sup>. In the catalytic applications of Pd nanoparticles, a large surface to volume ratio can improve Pd utilization efficiency. Therefore, compared to Pd nanocubes, Pd nanoparticles with dendritic or porous surface morphology may have a higher catalytic activity<sup>19</sup>.

One of the common methods to produce nanoparticle is colloidal-chemical synthesis because this method provides well established, straight-forward and simple approaches to obtain nanoparticles with unique shapes<sup>20</sup>. In colloidal-chemical

synthesis, metal precursors, surfactants or polymers as capping agents to stabilize particle size and shape, reducing agents and solvents to act as a reaction medium are mixed together and aged under a certain conditions to grow metal nanoparticles<sup>7, 20</sup>. In the synthesis, parameters such as precursors, surfactants, and growth conditions such as pH value and temperature are tunable<sup>21-22</sup>. Various shapes of metal nanoparticles can be fabricated with colloidal-chemical synthesis.

## 1.1 Thesis Outline

The introduction above presents the significant development and importance of metal nanoparticles. In the broad nanoscience field, this thesis focuses on the study of shape control in colloidal-chemical synthesis by using surfactant-surfactant or surfactant-polymer mixtures as capping agents. There are many research questions coming out.

1. Since capping agents are used to stabilize nanoparticle shape and size, is it possible to create specific shape by mixing two different capping agents?
2. What is the optimal ratio of two capping agents?
3. Is the shape of metal nanoparticles also influenced by other parameters such as types of metal precursors and pH value?
4. What is the microstructure of the metal nanoparticles?

Aim of the thesis was to control the shape of Au and Pd nanoparticles during their synthetic process to optimize the performance of nanoparticles in a variety of applications. In this thesis, it was studied a negatively charged surfactant, sodium oleate (NaOL), which was added in the traditional colloidal-chemical synthesis to assist classical capping agents in directing the growth of Au and Pd nanoparticles. The surfactant mixture of NaOL and hexadecyltrimethylammonium bromide (CTAB) improved efficiently the yield and narrowed the size distribution of Au nanorods<sup>23</sup> and resulted in a dendritic shape with a large surface to volume ratio in the synthesis of Pd nanoparticles. The surfactant mixture of NaOL and hexadecyltrimethylammonium chloride (CTAC), and the binary mixture of NaOL and polyvinylpyrrolidone (PVP) both assisted in forming Pd nanodendrites as well. Furthermore, we investigated the effects of the surfactant molar ratio between CTAB and NaOL, and the pH value of the mixture of PVP and NaOL on the formation of Pd nanodendrites to optimize the synthetic methods. Additionally, the method with optimal molar ratio between CTAC and NaOL for nanodendrite synthesis was successfully applied in the synthesis of hollow Ag-Pd nanodendrites, which have an even larger surface to volume ratio than solid Pd nanodendrites. Finally, the catalytic activity of Pd nanodendrites stabilized by PVP and NaOL was tested in the Sonogashira reaction and it was shown that these Pd nanodendrites had catalytic activity.

Transmission electron microscope (TEM) can image samples at an atomic resolution. It is ideal for the observation of the microstructure of nanoparticles. All the metal nanoparticles synthesized in this thesis were imaged by TEM. Additionally, selected area electron diffraction (SAED) and Kikuchi pattern in TEM were used to identify metal crystal structures. High-resolution images of the nanoparticles were taken from a high-resolution scanning transmission electron microscope (HRSTEM). Energy dispersive X-ray spectroscopy (EDS) in TEM was used to analyze elemental distribution in nanoparticles. These techniques were particularly utilized in the analysis of crystal structure and facets of Au nanorods and helped us discover that a large percentage of these Au nanorods were slightly bent due to the existence of growth-induced lattice strain. In addition to TEM, scanning electron microscopy (SEM), ultraviolet–visible (UV–vis) spectrometry, dynamic light scattering and conductance measurements assisted in the characterization of the properties of metal nanoparticles and reaction solutions in this thesis.



## Chapter 2 Noble Metal Nanoparticles

In this chapter, the background of noble metal nanoparticles, including synthetic methods, physical properties and applications are introduced. In the first section, the general methods of making nanoparticles, including the seed-mediated growth used in our experiments and growth theory are presented. Since Au and Pd nanoparticles were synthesized and studied in this thesis, it is necessary to understand their important properties. In the second and third sections, the LSPR of Au nanoparticles and the catalytic properties of Pd nanoparticles are described.

### 2.1 Synthesis of Noble Metal Nanoparticles

A metal nanoparticle is defined as a metal particle with an average diameter between 1 nm to 100 nm<sup>24</sup>. The nanoscale size gives nanoparticles unique characteristics including high surface-to-volume ratio, tunability of surface functionalization and spatial confinement of electrons, phonons, and electric fields<sup>25-26</sup>. Compared to their corresponding bulk materials, metal nanoparticles have markedly different physical and chemical properties, which makes them attract extensive attention<sup>8</sup>. Noble metal nanoparticles have been applied in human history since several thousand years ago. Gold, silver and copper nanoparticles were added in stained glass, ceramicists and cups to create beautiful colors by our ancestors<sup>27-28</sup>. However, it was not until 1850s that metal nanoparticles, a ruby gold colloid, were made in a lab by Michael Faraday for the first time, which started modern nanomaterial science<sup>1</sup>. In the past 160 years, synthetic methods of metal nanoparticles have been developed rapidly.

The preparation of noble metal nanoparticles is usually classified into top-down and bottom-up approaches<sup>3</sup>. In the top-down approach, macroscopic materials are reduced to nanoscale particles by physical or chemical methods, while in bottom-up approach, atoms or molecules are assembled to build up nanoparticles<sup>25</sup>. Top-down approaches include lithographic methods to create ordered nano-structure patterns by using light, electrons or electrostatic forces to remove parts of the bulk material, laser ablation methods to ablate bulk material by laser in an aqueous solution, and spray-pyrolysis methods to evaporate micron-size metal precursor droplets by flame or ultrasonic to form metal or metallic oxide nanoparticles<sup>3, 5-6, 25, 29</sup>. Top-down approaches are advantageous due to the simple and scale-up production processes but the nanoparticles made in this approach can have imperfect surfaces and nanostructures, which affects their chemical and physical properties<sup>25</sup>. Compared to top-down approaches, bottom-up methods can produce nanoparticles with fewer structure defects, better control of size and shape and more homogenous chemical composition. Therefore, this approach is widely used in scientific research. Bottom-up approaches include electrochemical methods where a metal plate anode converts into metallic ions by electrolysis in surfactant solution and is reduced

around the cathode to form nanoparticles, photochemical reduction where ultraviolet light stimulates electron transfer between metal ions and the copolymer or surfactant micelle template to reduce metal ions to nanoparticles, and colloidal-chemical synthesis where metal precursors stabilized by surfactants or polymers are reduced to metal nanoparticles by chemical reducing agents in solution<sup>3, 20</sup>. Colloidal-chemical synthesis, which is the focus point of the thesis, is one of the most widely used methods in the synthesis of Au and Pd nanoparticles. More specifically, seed-mediated growth and one-step seedless methods are two popular colloidal-chemical synthesis approaches.

### **2.1.1 Seed-mediated growth method**

Seed-mediated growth is a versatile method for the synthesis of noble metal nanoparticles because of many advantages. In seed-mediated growth, the experimental process is simple, reaction conditions are achievable in an average laboratory, reaction rates are relatively fast, the size and shape of nanoparticles can be easily controlled and complex nanostructures such as core-shell nanoparticles can be synthesized<sup>30-31</sup>.

Typical seed-mediated growth involves two steps: nucleation of tiny metal particles as seeds and subsequent growth of seeds into larger nanoparticles. In a solution containing capping agents, metal precursors are rapidly reduced by a reducing agent and nucleated to form a high concentration of tiny metal seeds. After that, a certain amount of seed solution is injected into a growth solution containing metal precursors, reducing agents and capping agents to continuously grow into nano-sized particles<sup>32</sup>. In the synthesis aiming to obtain large particles, the metal nanoparticles in the growth solution are used as seeds to grow in a second growth solution. This process can be repeated several times until the particles reach desired size<sup>33-34</sup>.

In general, metal precursors, reducing agents and capping agents are necessary for both seed and growth solutions. Metal precursors are usually water-soluble metal salts to provide metal ions. Reducing agents such as L-ascorbic acid (AA) or sodium borohydride (NaBH<sub>4</sub>) are employed to reduce metal ions to atoms. Capping agents, including surfactants, polymers, dendrimers and ligands, cover the surface of metal seeds and nanoparticles to direct the growth of seeds, control the shape and size of nanoparticles and stabilize nanoparticles in solutions<sup>35-38</sup>. Beyond these basic reagents, other chemicals that can direct the shape of nanoparticles are selectively added in the growth solutions as well. For example, silver nitrate (AgNO<sub>3</sub>) is widely used in the growth of Au nanorods because it improves the nanorod yield and controls the aspect ratio of Au nanorods<sup>39</sup>. The morphology of metal nanoparticles can also be tuned by adding halide ions, especially Br<sup>-</sup> and Cl<sup>-</sup> ions<sup>40</sup>.

Most of seed-mediated growth syntheses happen in aqueous solutions but organic solvents such as ethylene glycol and organic amines are employed for syntheses containing non-water-soluble reagents<sup>41-42</sup>. In seed-mediated growth, types and concentrations of reagents, injection rates and order of reagents, reaction temperature, pH value and incubation time are all important parameters for the reaction<sup>43</sup>. The size, shape and yield of metal nanoparticles can be tuned by controlling one or several of these parameters. Additionally, because the reaction is very sensitive, it is critical to keep clean reaction containers, solutions and tools involved in the experiment in order to prevent the negative effects of impurities<sup>43</sup>.

Through the seed-mediated growth method, we can not only synthesize metal nanoparticles with spherical, cubic, triangular, dendritic, rod-like and star-like shapes but also core-shell and hollow nanostructures<sup>44-50</sup>.

#### **2.1.1.1 Core-shell metal nanoparticles**

Core-shell metal nanoparticles are a type of multiple-phasic material consisting of an core structure and at least one shell layer that are composed of different materials<sup>51</sup>. Core-shell metal nanoparticles can be synthesized by seed-mediated growth methods. Instead of using a single metal source, different metal precursors are employed in the seed and growth solutions, which creates the nanoparticles with composite properties of both metal materials<sup>52</sup>. This method is versatile and powerful to combine a wide range of metal types together, such as Au@Ag, Pd@Ag and Au@Pd@Pt<sup>53-55</sup>. During the synthesis, the size and shape of core particles and the thickness and morphology of shell structure can be easily controlled by tuning the growth parameters<sup>56-57</sup>.

#### **2.1.1.2 Hollow metal nanoparticles**

Hollow metal nanoparticles have both inner and outer surface, making them advantageous in catalytic applications. One of the most popular methods to synthesize hollow metal nanoparticles is the double template method, which is based on seed-mediated growth. In this method, seeds used as a hard template are added in the growth solution. As the reduced metal precursors continuously grow on the seed surface, at the same time, a galvanic replacement reaction between ionic metal precursors and the seeds occurs, where the seed atoms are oxidized to ions again<sup>58</sup>. This requires the seed metal to have a lower redox potential than the growth metal in order to exchange electrons with metal precursor ions in growth solutions<sup>59</sup>. Because Ag is easily oxidized and comparatively cheap, it is usually employed as the seed metal in synthesis of hollow noble metal nanoparticles, especially Au, Pt and Pd<sup>60-62</sup>. Another component of the double template method is the capping agent used to direct and stabilize the shape and size of hollow metal nanoparticles<sup>58</sup>.

### **2.1.2 One-step seedless method**

One-step seedless method combines the nucleation and growth processes in one solution, containing metal precursors, reducing agents and capping agents. The seedless growth process is even faster and simpler than seed-mediated growth and fabricates nanoparticles with high yield and typically high polydispersion<sup>63-64</sup>. However, since the one-step seedless method has less tunability than seed-mediated growth, it is usually used to synthesize nanoparticles with comparatively simple shape and compositions, and small size.

### **2.1.3 Nucleation and growth theory**

Since both seed-mediated growth and one-step seedless methods are processes to nucleate and grow metal nanoparticles, it is important to understand the fundamental nucleation and growth theory for the development of metal nanoparticle synthesis. The investigation of nucleation and growth theory has occurred over a long period of time and several models have been built. At the end of 19<sup>th</sup> century, Wilhelm Ostwald, a German chemist, made a significant achievement on the explanation of colloidal metal nanoparticle behaviors with his Ostwald ripening<sup>65</sup>. In the early 20<sup>th</sup> century, classical nucleation theory, which describes nucleation kinetics of a new structure or a new thermodynamic phase was first established by Volmer and Weber and then developed by Becker and Döring, Frenkel, and other researchers<sup>66-68</sup>. Later, in 1950s, this theory was transformed into LaMer's nucleation theory to describe the formation of colloidal nanoparticles by LaMer and coworkers<sup>69</sup>. In recent decades, new nucleation and growth theories of nanoparticles such as Finke-Watzky two step mechanism, coalescence and orientated attachment and intraparticle ripening have been developed<sup>70</sup>. However, the formation mechanism of nanoparticles is still controversial because there is no model that could describe the evolution of the nanoparticle size and shape in detail<sup>71</sup>.

#### **2.1.3.1 *Classical nucleation theory***

Classical nucleation theory is the most widely accepted theoretical model for the nucleation kinetics of a new thermodynamic phase and a majority of theoretical researches on nucleation are on the basis of classical nucleation theory. Classical nucleation theory is derived from supersaturated vapors and extended to liquid–solid equilibrium systems<sup>67, 72</sup>. Macroscopic quantities such as the surface energy are applied to predict approximately the nucleation rate<sup>71-72</sup>. In this theory, the nucleation is classified as homogeneous or heterogeneous nucleation. Homogeneous nucleation occurs randomly and spontaneously in the parent phase without any favorable sites, while heterogeneous nucleation forms on a surface between two phases such as impurities and container surfaces. Heterogeneous

nucleation happens much more often than homogeneous nucleation, but the latter has a simpler formation mechanism.

In homogeneous nucleation, the Gibbs free energy of a spherical nucleus consists of a negative bulk free energy and a positive surface free energy, as shown in Eqn (2.1).

$$\Delta G = -\frac{4}{3}\pi r^3 |\Delta G_V| + 4\pi r^2 \sigma \quad (2.1)$$

In this equation,  $\Delta G$  is the nucleus Gibbs free energy,  $r$  is the radius of the spherical nucleus,  $\Delta G_V$  is the difference in Gibbs bulk free energy per unit volume and  $\sigma$  is the surface tension of the nucleus surface.

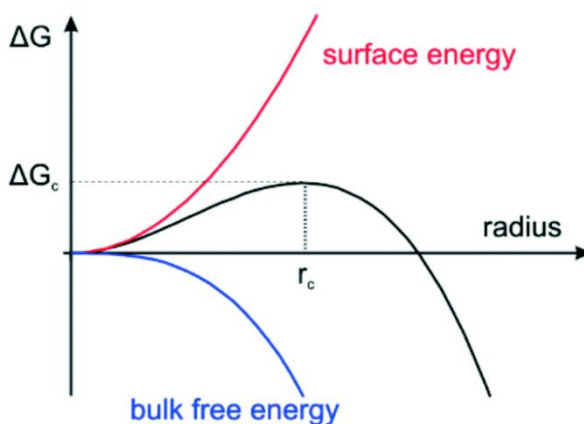


**Figure 2.1.** Diagram depicting the dependence of the nucleus Gibbs free energy ( $\Delta G$ ) on the nucleus radius ( $r$ ) according to homogeneous nucleation in classical nucleation theory. The black curve is Gibbs free energy, the blue curve is bulk free energy and the red curve is surface free energy. Reproduced from Reference Polte, J., *Fundamental Growth Principles of Colloidal Metal Nanoparticles – A New Perspective*. *CrystEngComm* 2015, 17, 6809-6830, with the permission from the Royal Society of Chemistry<sup>71</sup>.

The schematic of this equation has been displayed in Figure 2.1. It shows that there is a critical radius ( $r_c$ ) for the spherical nucleus, where the Gibbs free energy reaches a maximum value ( $\Delta G_c$ ), due to the superposition of bulk free energy and surface free energy. The  $\Delta G_c$  forms a nucleation barrier. When the radius of a nucleus is smaller than  $r_c$ , the growth is unfavorable, while the growth of a nucleus with a radius larger than  $r_c$  is favorable and nucleation occurs.

In heterogeneous nucleation, part of the nucleus surface area is attached to a two-phase interface such as the container surface or impurities in the solution, leading to a smaller exposed surface area than that of the spherical nuclei in homogeneous nucleation. Therefore, the surface free energy of nuclei in heterogeneous nucleation

is lower, which decreases the Gibbs free energy. This lower energy barrier makes heterogeneous nucleation occur more easily and often than homogeneous nucleation.

Classical nucleation theory only discusses the nucleation process and the subsequent growth is considered as a separate process. The growth of nuclei can be explained by a variety of theories such as aggregation, diffusion limited growth or Oswald ripening<sup>71</sup>.

### 2.1.3.2 LaMer's nucleation theory

LaMer and his coworkers transformed the classical nucleation theory into LaMer's nucleation, which is the only widely accepted theory to describe the nucleation and growth of colloidal nanoparticles<sup>71,73</sup>. This theory is suitable for both seed-mediated growth and one-step seedless growth processes. The schematic of LaMer's nucleation theory is displayed in Figure 2.2 and in this model, the nucleation and growth are separated in the formation of nanoparticles.

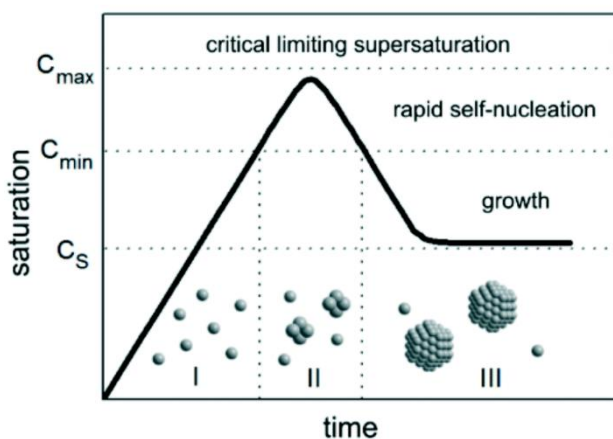


**Figure 2.2.** Schematic of LaMer's nucleation theory. The curve describes the change of the monomer concentration according to time. Reproduced from Reference Polte, J., *Fundamental Growth Principles of Colloidal Metal Nanoparticles – A New Perspective*. CrystEngComm 2015, 17, 6809-6830, with the permission from the Royal Society of Chemistry<sup>71</sup>.

In Figure 2.2, the process of nucleation and growth through LaMer's mechanism is divided into three time periods. In Period I, the concentration of free monomer, metal atom, is increasing rapidly, which results from a rapid reduction of metal precursor ions into atoms in the synthesis of metal nanoparticles. When the concentration of free monomers reaches a critical supersaturation level ( $C_s$ ), the occurrence of homogeneous nucleation is possible, but the possibility and nucleation rate are low. Then, the free monomer concentration continues to increase until reaching  $C_{min}$ , the minimum concentration for rapid self-nucleation. In Period

II, self-nucleation bursts occur in the free monomers because the maximum of the Gibbs free energy barrier for nucleation is overcome when the monomer concentration reaches supersaturation. Because the instant appearance of abundant nuclei consumes a great number of free monomers, the monomer concentration starts to decrease after reaching a maximum value. When the monomer concentration becomes lower than  $C_{\min}$  again, supersaturation is relieved and self-nucleation is terminated. In Period III, the number of nuclei does not increase anymore. Instead, the growth occurs by diffusion of the remaining free monomers towards nuclei surfaces.

In the one-step seedless method, the nucleation and growth of metal nanoparticles occur in the same solution, following LaMer's nucleation theory. In seed-mediated growth, nucleation and initial growth mainly occur in a seed solution and later, further growth continues in a growth solution. Additionally, the nucleation and growth rates can be tuned by controlling reaction parameters such as types and concentration of reducing agents and reaction temperature.

### 2.1.3.3 Other theories

In addition to LaMer's nucleation, several theories below are applied to describe the formation of nanoparticles as well.

Ostwald ripening theory, established by Wilhelm Ostwald in 1890s, describes the change of a heterogeneous structure as a function of time. In this theory, molecules or atoms on the surface of a cluster are energetically less stable than those inside of a cluster, so a larger cluster with a lower surface-volume ratio is more stable and energetically favorable than a smaller cluster. In the synthesis of nanoparticles, smaller nuclei, which have higher solubility and surface energy, are redissolved in the solution and in turn, larger nuclei are supported to grow into nanoparticles<sup>70</sup>.

Coalescence and oriented attachment both describe the growth process of crystal nuclei through a spontaneous self-attachment mechanism of adjacent crystal particles<sup>70</sup>. Oriented attachment occurs in the particles that have a common crystallographic orientation, leading to a planar interface joining, whereas, coalescence has no specific preference of orientation<sup>70</sup>. The driving force of oriented attachment is surface energy reduction<sup>74</sup>. Small crystal clusters are favored to assemble to decrease surface energy of the entire system by removing highly energetic grain boundaries<sup>74</sup>. This phenomenon has been discovered in platinum and titania crystallites<sup>74-75</sup>.

Intraparticle ripening elucidates a shape evolution during the growth of nanocrystals at low crystal monomer concentration<sup>76</sup>. When the different facets of nanocrystals have different surface energies, the facets with the higher energy are dissolved but the facets with low energy continue growing, resulting in an intraparticle diffusion<sup>70</sup>. Further, shape control and evolution can be achieved by this process.

Additional theories, such as the Fink-Watzky two step mechanism, exist for specific metals or synthetic conditions, but are out of the scope of this thesis<sup>77-78</sup>.

## 2.2 Localized Surface Plasmon Resonance

Localized surface plasmon resonance (LSPR) is a common optical characteristic of conductive nanosized particles, such as metallic nanoparticles, with a diameter equal to or smaller than the wavelength of incident light. When a beam of incident light goes through the metallic nanoparticles, the electric field of the incident light at a certain frequency excites coherent oscillations of the free conduction electrons in the metallic nanoparticles<sup>79</sup>. This natural resonance frequency is identified as the LSPR, which is related to the effective electron mass, density of electrons and charge distribution of the materials. Figure 2.3 (a) shows how the LSPR of a metal sphere is excited. The excitation of the LSPR enhances light absorption and scattering of metallic nanoparticles<sup>80</sup>. As shown in Figure 2.3 (b) the incident light is absorbed when its frequency matches with the natural resonance frequency of metal nanoparticles. For metal nanospheres, there is only one absorption band. However, metal nanorods such as Au nanorods have electrons oscillations along both longitudinal and transverse directions, as shown in Figure 2.3 (c), resulting in two different absorption bands in the absorption spectrum in Figure 2.3 (d).

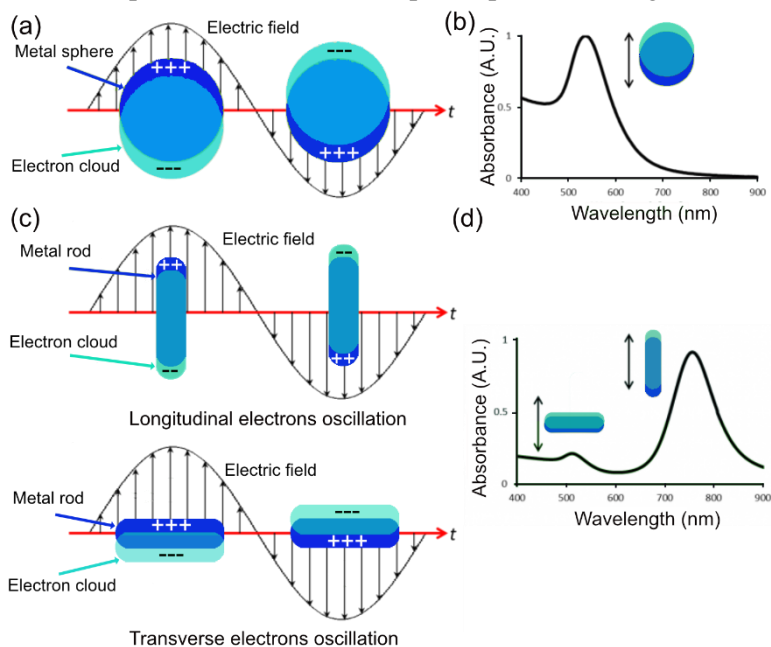


**Figure 2.3.** (a) Schematic illustration of LSPR for a metal nanosphere. (b) A typical absorption spectrum of metal nanospheres. (c) Schematic illustration of LSPR for a metal nanorod. (d) A typical absorption spectrum of metal nanorods.

## 2.3 Catalytic Properties

In the last 30 years, various forms of Pd such as Pd nanoparticles, Pd complexes and Pd oxides have been utilized as catalysts in carbon-carbon coupling reactions. Especially, Richard F. Heck, Ei-ichi Negishi and Akira Suzuki were awarded the Nobel Prize in Chemistry 2010 for their contributions on Pd-catalyzed cross coupling in organic synthesis<sup>81</sup>. Carbon-carbon coupling reactions are some of the most important methodologies for the synthesis of organic molecules and include the Sonogashira, Suzuki, Heck and Stille reactions<sup>82</sup>. In typical Pd(0) catalytic cycles, Pd is activated to form reactive Pd(0) compounds under reaction conditions first. This is a necessary condition for second step. Then, the oxidative addition with vinyl or aryl halide is inserted in the active Pd(0) forming a Pd(II) complex. After that, the Pd(II)-halide complex is involved in the transmetalation or beta-hydride elimination process to generate the compound where two separate coupling fragments are combined on the Pd(II)-halide complex. In the last step, the Pd(II) complex is reduced to release the C-C coupling product and regenerate the initial active Pd(0) again<sup>82</sup>.

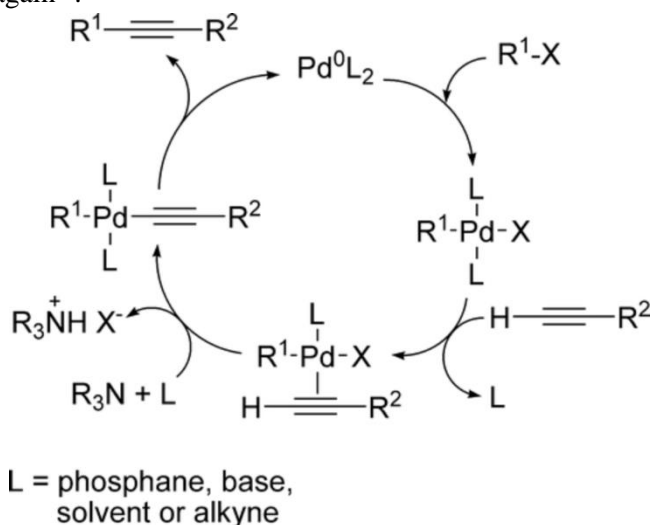


**Figure 2.4.** Mechanism for the Pd-catalyzed Sonogashira reaction. (Reproduced from Reference 83 with the permission from Chinchilla, R.; Nájera, C., *The Sonogashira Reaction: A Booming Methodology in Synthetic Organic Chemistry*. Chemical Reviews 2007, 107 (3), 874-922. Copyright 2007, American Chemical Society)

The Sonogashira coupling reaction, one of the most common carbon-carbon coupling reactions, forms the carbon-carbon bond between a vinyl or aryl halide and a terminal alkyne<sup>83</sup>. A general mechanism for the Pd-catalysed Sonogashira reaction is shown in Figure 2.4. The Pd catalytic cycle is initiated by inserting the oxidative addition with the vinyl or aryl halide in the active  $[\text{Pd}(0)\text{L}_2]$  forming a  $[\text{Pd}(\text{II})\text{R}^1\text{X}]$  complex. In the second step, an alkyne-Pd(II) complex is produced by a reversible

$\pi$ -coordination of the alkyne. Then, the alkyne is deprotonated by the amine, forming coordination between the acetylene ligand and the Pd metal. At last, the Pd(II) complexes release the final products, and at the same time, the Pd(II) ion is reduced to the initial active  $[\text{Pd}(0)\text{L}_2]$ <sup>84-85</sup>.

# Chapter 3 Capping Agents

Surfactants and polymers are used as capping agents to stabilize shape and size of Au and Pd nanoparticles in our experiments. In order to understand how capping agents influence the shape, it is important to introduce the basic theory of the surfactants and polymers. In this chapter, chemical structures of the capping agents (surfactants and polymers) used in this thesis are introduced. After that, the basic theory of surfactants and polymers as capping agents, their properties, and the adsorption of capping agents on solid surfaces, including the surface of metal nanoparticles, are presented.

## 3.1 Structure of Capping Agents

### 3.1.1 Structure of surfactants

Surfactants, short for surface-active agents, are a class of compounds that can lower the interfacial tensions between a liquid phase and another phase, which could be a liquid, a solid or a gas. Due to this property, surfactants are widely used as wetting agents, detergents and emulsifiers in industrial and consumer products, including familiar commodities: shampoos, multi-surface sprays and dish detergents<sup>86</sup>. In general, surfactants are amphiphilic molecules, consisting of both hydrophilic polar head groups, which attract water, and hydrophobic tails, which repel water<sup>87</sup>. These two opposite tendencies of head and tail groups compel the surfactants to move to the interfaces between water and the second phase. The hydrophilic part remains immersed in the water and the hydrophobic part orients towards the second phase such as oil, air or a solid surface. Through adsorbing at the interface, surfactants decrease the surface tension of water. A good surfactant is supposed to have a low solubility in any bulk phases but a strong tendency towards the interfaces<sup>88</sup>.

Surfactant tails usually have similar features, which could be hydrocarbon, polydimethylsiloxane or fluorocarbon chains<sup>88</sup>. Generally, surfactants are classified according to the charge of their head groups into nonionic, anionic, cationic and zwitterionic surfactants. Anionics are considered as the largest class of surfactants. Nearly 70% of the surfactants typically consumed are made of anionics<sup>88</sup>. Nonionics are the second largest class and usually compatible with all other types of surfactants. Cationics are the third largest class. Due to negatively charged surfaces for most solid materials, cationics can adsorb strongly at most solid surfaces such as metal nanoparticles. As the smallest class of surfactants, zwitterionics contain both cationic and anionic groups on the same molecule, where the cationic group is usually ammonium<sup>88</sup>.

The status of a surfactant in an aqueous solution depends on its concentration. When the concentration of the surfactant is very low, it only exists as unimers in the solution. As the concentration is increased above the critical micelle concentration (CMC) of the surfactant, self-assembled aggregation of unimers begins, forming micelles. Different geometrical morphologies of surfactant molecules result in a variety of self-assembly structures. The classical structures include the spherical micelle, cylindrical micelle, lamellar phase, reversed micelle, bicontinuous cubic structure and bilayer vesicle, shown in Figure 3.1<sup>88</sup>.

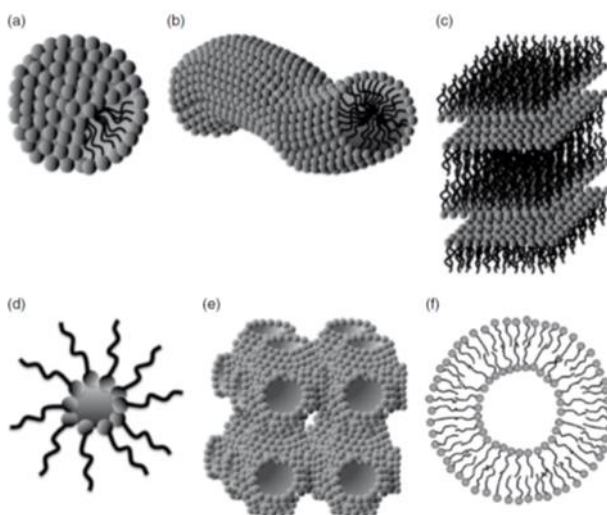


**Figure 3.1.** Classical self-assembly structures of surfactants: (a) spherical micelle; (b) cylindrical micelle; (c) lamellar phase; (d) reversed micelle; (e) bicontinuous cubic structure; (f) bilayer vesicle. (Reproduced from Reference 88. Copyright (2014) Wiley. Used with permission from Kronberg, B.; Holmberg, K.; Lindman, B., *Surfactant Self-Assembly: General Aspects and Spherical Micelles*, Surface Chemistry of Surfactants and Polymers. Wiley)

### 3.1.2 Structure of polymers

Polymers are macromolecules which are built up of repetitive small chemical units, known as monomers. The configuration of a polymer is classified as linear, branched or cross-linked structures according to the physical arrangement of monomer side chains, as shown in Figure 3.2. If the polymer consists of only one type of monomer, it is called a homopolymer. Whereas, if the polymer contains two or more types of monomers, it is called a copolymer. According to the approaches of acquisition, polymers are divided into biological macromolecules from nature, including proteins and nucleic acids, and nonbiological macromolecules from synthesis, containing common plastics. For nonbiological polymers, the synthesis is carried out through a polymerization of the monomers. Therefore, properties of the

polymer are influenced deeply by monomer properties. Based on the polarity of monomers, nonbiological polymers are categorized into polar, nonpolar and ionized polymers<sup>88</sup>. Since many polymers can disperse well in aqueous solutions and adsorb at solid surfaces, some of the polymers present similar behaviors as surfactants to stabilize metal nanoparticles. Additionally, compared to surfactants, a polymer can be easily modified by adding or removing functional groups, such as hydrophobic and hydrophilic chains. It is possible to design a proper polymer for stabilization of specific nanoparticles<sup>88</sup>.

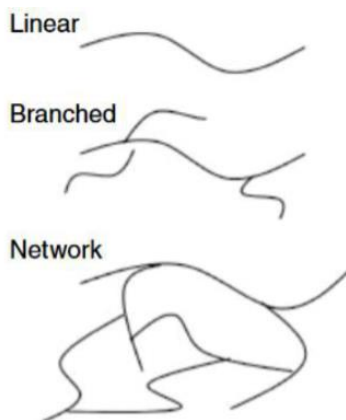


**Figure 3.2.** Categories of polymers by structure. (Reproduced from Reference 88. Copyright (2014) Wiley. Used with permission from Kronberg, B.; Holmberg, K.; Lindman, B., *Polymers in Solution, Surface Chemistry of Surfactants and Polymers*. Wiley)

### 3.1.3 Stabilization of nanoparticles by capping agents

The electrostatic interaction and hydrophobic effect are two fundamental forces in surface and colloid chemistry. They are also the driving forces for surfactants and polymers to stabilize metal nanoparticles in aqueous solutions. Electrostatic interactions happen between an ionic capping agent and a charged particle surface. If they have opposite charges, electrostatic interactions drive the capping agent towards the particle surface. If they have the same charge, the capping agent resists close interaction with the particle surface. Additionally, hydrophobic effect is the major driving force for water-insoluble surfactants or polymers to move to an interface, such as the particle surfaces. In some conditions, both electrostatic interactions and hydrophobic effects exist and govern the system together.

When metal nanoparticles are in an aqueous solution containing charged surfactants or polymers, their surface is wrapped by a layer of the charged capping agents. When two metal nanoparticles get close, the increase of electrostatic repulsion between their wrapping layers counterbalances the attractive Van der Waals force

and pushes the particles away, which ensures the stability of dispersed metal nanoparticles by electrostatic stabilization<sup>88</sup>.

If two polymer-stabilized nanoparticles are repulsed by repulsive entropic and osmotic forces, it is called steric stabilization. When two polymer-stabilized nanoparticles get close, in the region where polymer tails from both particles overlap, the ligand concentration increases, resulting in an osmotic inflow and ligand entropy decreases to form the repulsive forces<sup>88</sup>.

### 3.1.4 Chemical structures of the applied capping agents

Chemical structures of the capping agents used in this thesis are shown in Figure 3.3. Hexadecyltrimethylammonium bromide (CTAB,  $C_{19}H_{42}BrN$ ) and hexadecyltrimethylammonium chloride (CTAC,  $C_{19}H_{42}ClN$ ) are cationic surfactants with the same positively charged cationic chains but different halide counterions. Both CTAB and CTAC are common surfactants for the synthesis of metal nanoparticles. CTAC has a higher water solubility than CTAB at room temperature. Polyvinylpyrrolidone (PVP) is a water-soluble nonionic polymer widely used in the synthesis of metal nanoparticles. Sodium oleate (NaOL,  $C_{18}H_{33}NaO_2$ ) and sodium stearate (NaST,  $C_{18}H_{35}NaO_2$ ) are anionic surfactants. They have the same head group and the same number of carbons in the tails, but NaOL contains a carbon-carbon double bond in its tail.

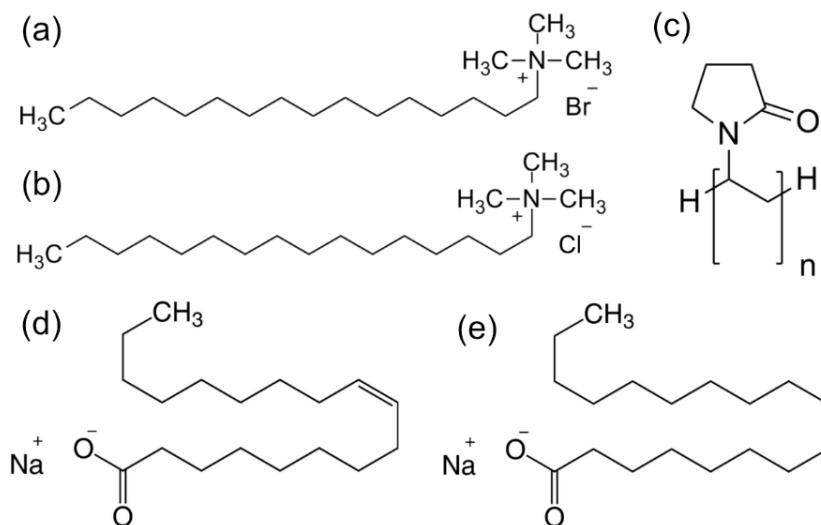


**Figure 3.3.** Chemical structures. (a) Hexadecyltrimethylammonium bromide. (b) Hexadecyltrimethylammonium chloride. (c) Polyvinylpyrrolidone. (d) Sodium oleate. (e) Sodium stearate.

## 3.2 Properties of Surfactants

### 3.2.1 Critical micelle concentration

Critical micelle concentration (CMC) is the concentration at which surfactants start to form micelles. As shown in Figure 3.4 (a), above the CMC, the concentration of surfactant monomers is stable and all additional surfactants form micelles in aqueous solutions. CMC is an important characteristic because properties of a surfactant solution, including surface tension, osmotic pressure, turbidity, conductivity and solubility, have obvious changes at CMC, as shown in Figure 3.4. (b). For example, the surface tension decreases drastically with the increase of surfactant concentration before reaching the CMC, but the surface tension is a relatively constant value after reaching the CMC. There is an apparent turning point at the CMC. Therefore, CMC can be measured by testing surface tension or other physical properties that have turning points. The value of CMC depends on temperature, pressure and chemical structure. As the alkyl chain length increases, the CMC value reduces. Ionic surfactants usually have higher CMC than nonionic surfactants. However, the influence of temperature on CMC differs with surfactant type. Ionic surfactants are usually independent of temperature. Additionally, the CMC of ionic surfactants can be reduced by adding salts as well<sup>88</sup>.

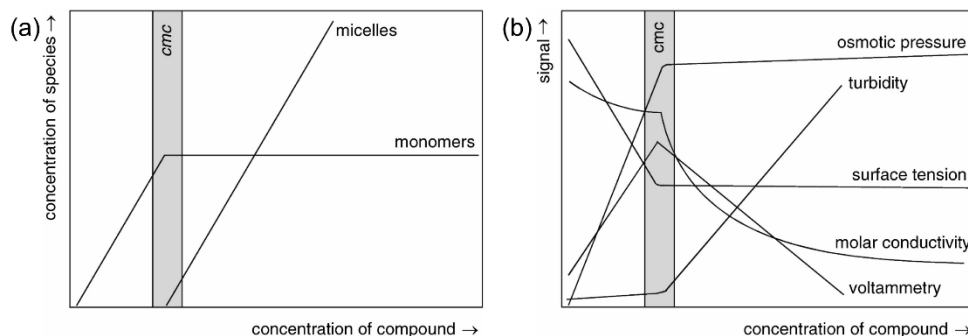


**Figure 3.4.** (a) Illustration of CMC based on concentration of micelles and monomers relative to the surfactant concentration. (b) Representation of concentration-dependent properties of a surfactant solution. Reproduced from Reference Nesměrák, K.; Němcová, I., Determination of Critical Micelle Concentration by Electrochemical Means. Analytical Letters 2006, 39 (6), 1023-1040 with the permission from Taylor & Francis<sup>89</sup>.

### 3.2.2 Critical packing parameter

Critical packing parameter (CPP) is an important parameter for self-assembled aggregation. It is a ratio that describes the geometry of a single surfactant molecule and is generally used to deduce the micelle structure of a given surfactant. CPP relates to the head group area, carbon chain volume and chain length, defined as:

$$CPP = v/(al_{max}) \quad (3.1)$$

In this formula,  $v$  stands for the volume of a single surfactant tail,  $a$  represents the effective head group area and  $l_{max}$  is the length of the extended alkyl chain<sup>90</sup>. Figure 3.5. (a) describes CPP in a schematic, where a surfactant molecule is a unit of the micelle. The micelle radius  $R_{mic}$  is usually less than or equal to  $l_{max}$ .

Figure 3.5. (b) depicts the relation between the CPP and aggregation structures. When  $CPP < \frac{1}{3}$ , surfactants prefer forming spherical micelles. At  $\frac{1}{3} < CPP < \frac{1}{2}$ , surfactants start to form cylindrical structures. When  $CPP = 1$ , Lamellar phases are formed. As  $CPP > 1$ , surfactants form reversed structures. In addition to geometrical factors, aggregation structures are also influenced by temperature, concentration, cosolute and the interaction between the head groups<sup>88</sup>.

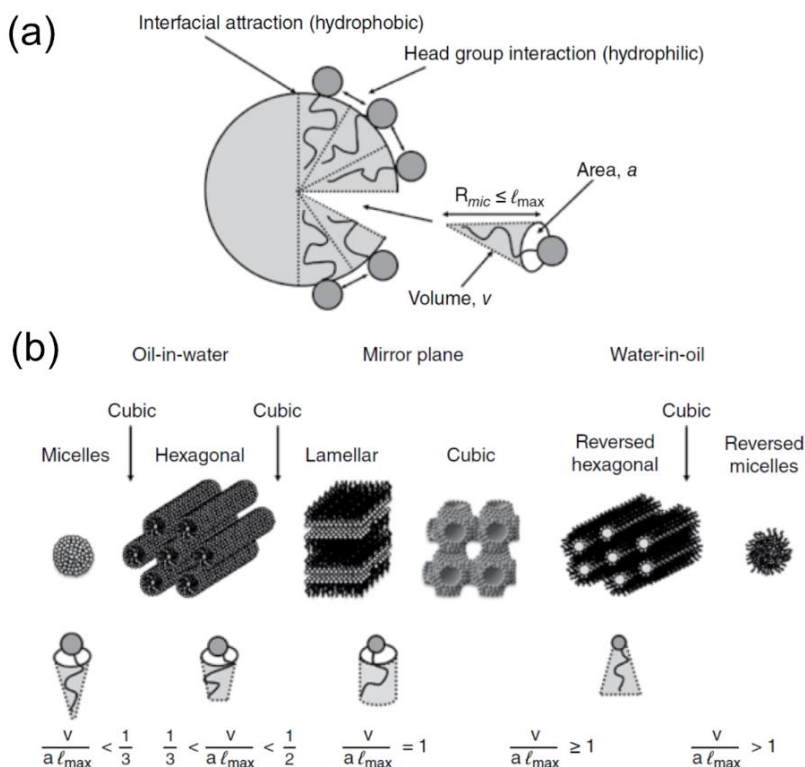


**Figure 3.5.** (a) Schematic of the CPP based on the geometrical consideration. (b) CPP values of surfactant molecules correlate to aggregation structures for geometrical packing factors. (Reproduced from (a) Reference 91, (b) References 88. (a) Was published in Publication Intermolecular and Surface Forces, Israelachvili, J. N., Soft and Biological Structures, p535-576, Copyright Elsevier (2011). (b) Copyright (2014) Wiley. Used with permission from Kronberg, B.; Holmberg, K.; Lindman, B., Surfactant Self-Assembly: Beyond the Spherical Micelle, Surface Chemistry of Surfactants and Polymers. Wiley)

### 3.2.3 Krafft temperature

Krafft temperature ( $T_K$ ), also known as the Krafft point, is the temperature at which the solubility of a surfactant in a solution is equal to its CMC and above which the solubility of the surfactant increases sharply<sup>88,91</sup>.

### 3.2.4 Hydrophilic-lipophilic balance

Hydrophilic-lipophilic balance (HLB) is a measure of hydrophilic or lipophilic tendency of a surfactant between water and oil, calculated by the values from different regions of the surfactant molecule. The HLB number is in a range of 0 to 20, corresponding to a tendency from lipophilicity to hydrophilicity. The HLB number is a widely used indicator to evaluate the usability of a surfactant in a practical application<sup>92-93</sup>. Generally, surfactants with low HLB number are used for making water-in-oil emulsions and surfactants with high HLB numbers are used as emulsifiers for oil-in-water emulsions<sup>88</sup>.

## 3.3 Properties of Polymers

### 3.3.1 Molecular weight

Molecular weight is an important value for a polymer. It is impossible for a polymer to consist of the macromolecules with the exact same molecular weight. Therefore, a molecular weight average is used to evaluate the polydispersity of molecular weight. There are two methods, number average ( $M_n$ ) and weight average ( $M_w$ ), to calculate molecular weight averages<sup>88</sup>. The number average molecular weight is defined as:

$$M_n = \frac{\sum N_i M_i}{\sum N_i} \quad (3.2)$$

The weight average molecular weight is defined as:

$$M_w = \frac{\sum N_i M_i^2}{\sum N_i M_i} \quad (3.3)$$

In both formulas,  $N_i$  is the number of molecules with molecular weight  $M_i$ .

### 3.3.2 Cloud point and critical point

Cloud point is the temperature where phase separation occurs in a polymer solution with a certain concentration, making the solution turbid<sup>88</sup>. The critical point is the point where phase separation occurs, including critical temperature and critical composition. Critical temperature is the highest or lowest temperature at which phase separation of a polymer solution occurs and the corresponding polymer concentration is critical composition<sup>88</sup>.

### 3.3.3 Properties of Polyvinylpyrrolidone

Polyvinylpyrrolidone (PVP) is a nonionic and nontoxic polymer, consisting of the monomer N-vinylpyrrolidone, which is soluble in water, methanol, ethanol and other polar solvents<sup>94-95</sup>. In a PVP molecule, the pyrrolidone moiety component is hydrophilic and the alkyl group is hydrophobic, making the PVP become an excellent capping agent to stabilize metal nanoparticles<sup>96</sup>.

## 3.4 Mixture of Two Capping Agents

### 3.4.1 Mixture of two surfactants

In practical applications, two or more surfactant species are often mixed to reach synergistic effects with reference to characteristics of each individual surfactant. The CMC of a surfactant mixture depends on the CMCs of each individual surfactant. In ideal conditions, where there is no attractive or repulsive interaction between different species of surfactants, so-called no net interaction ( $\beta=0$ ), the mixture CMC of two surfactants is simply described as:

$$\frac{1}{CMC} = \frac{x_1}{CMC_1} + \frac{x_2}{CMC_2} \quad (3.4)$$

$CMC$  is the CMC value of the surfactant mixture.  $CMC_1$  and  $CMC_2$  are the CMC values of two individual surfactants.  $x_1$  and  $x_2$  are the corresponding molar fraction of two surfactants. Additionally, the molar fraction of surfactant 1 in the mixture micelle ( $x_1^m$ ) can be calculated as well by:

$$x_1^m = \frac{x_1 CMC_2}{x_1 CMC_2 + x_2 CMC_1} \quad (3.5)$$

Further, the molar fraction of surfactant 2 in the mixture micelle ( $x_2^m$ ) is obtained by:

$$x_2^m = \frac{x_2 CMC_1}{x_1 CMC_2 + x_2 CMC_1} \quad \text{or} \quad x_2^m = 1 - x_1^m \quad (3.6)$$

However, if a net interaction exists in the surfactant mixture system, where  $\beta < 0$  stands for attraction and  $\beta > 0$  represents for repulsion, an activity coefficient  $f_i$  is required in formulas (3.4) and (3.5):

$$\frac{1}{CMC} = \frac{x_1}{f_1 CMC_1} + \frac{x_2}{f_2 CMC_2} \quad (3.7)$$

and

$$x_1^m = \frac{x_1 f_2 CMC_2}{x_1 f_2 CMC_2 + x_2 f_1 CMC_1} \quad (3.8)$$

The relation between the activity coefficient and the net interaction is given by:

$$\ln f_1 = (x_2^m)^2 \beta \quad \text{and} \quad \ln f_2 = (x_1^m)^2 \beta \quad (3.9)$$

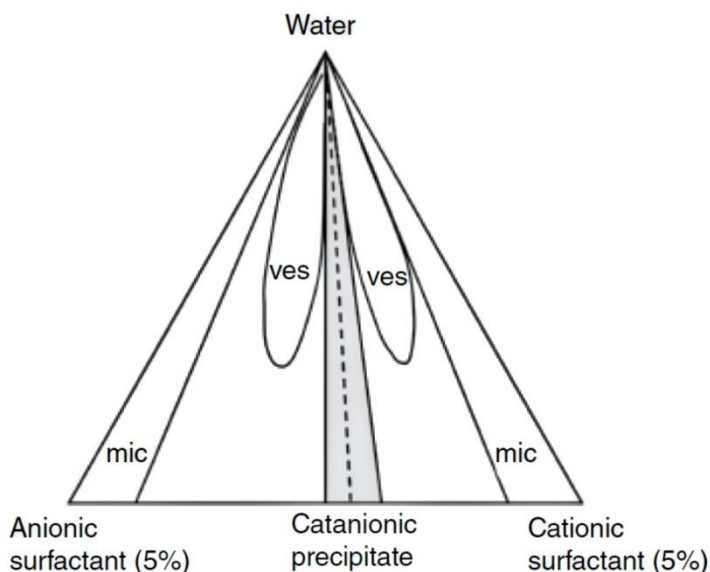


**Figure 3.6.** Phase diagram schematic for a mixture of cationic and anionic surfactants. (Reproduced from References 88 and 98. This figure was published in Publication Phase Science of Surfactants, 1 (5), Khan A., Current Opinion in Colloid & Interface Science, p614-623, Copyright Elsevier (1996). Copyright (2014) Wiley. Used with permission from Kronberg, B.; Holmberg, K.; Lindman, B., Mixed Surfactant Systems, Surface Chemistry of Surfactants and Polymers. Wiley)

Through the introduction of an anionic surfactant, it is possible to reduce the CMC of a cationic surfactant. Figure 3.6 shows a schematic phase diagram for a cationic and an anionic surfactant mixture. When the molar ratio of two surfactants is close to 1, the surfactant mixture system starts to form a catanionic precipitate. Increasing

the molar ratio of one of the surfactants results in the dissolution of the precipitate in the solution. When the molar amount of one surfactant is much higher than that of the other, the surfactant mixture forms micelles. Vesicles can be formed as well under a proper concentration and molar ratio of two surfactants<sup>88</sup>.

### 3.4.2 Mixture of a surfactant and a polymer

Mixtures of water-soluble polymers and surfactants have wide applications because the mixtures can have synergistic effects from both surfactants and polymers, achieving better colloidal stability, flocculation and emulsification. For example, the existence of a polymer can modify the performance of an a surfactant on surface tension. As shown in Figure 3.7, at low surfactant concentration, the mixture has a similar trend as the pure surfactant, but a lower surface tension value. However, the first difference occurs before reaching the CMC, where the surfactant micelles start to form on the polymer. This concentration is termed as critical association concentration (CAC). After CAC, there is a concentration region with a relatively constant surface tension. When the polymer becomes saturated with surfactant micelles, the second deviation occurs. Following that, the surface tension continuously reduces towards the same value as the surfactant-only system and the third change sets the system to form normal micelles in the solution<sup>88</sup>.

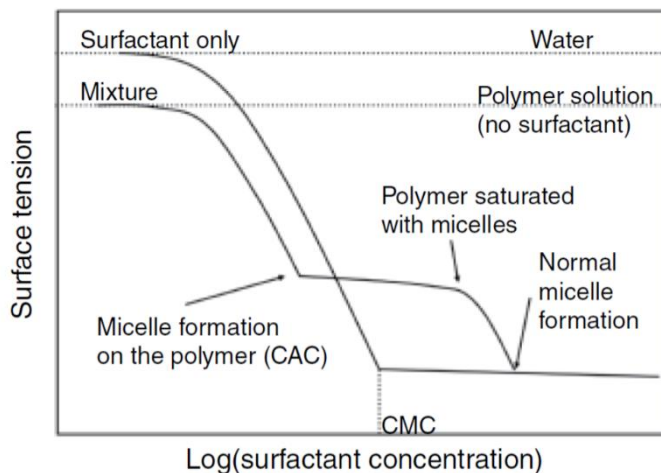


**Figure 3.7.** Schematic of surface tension curves for a mixed surfactant-polymer system and a surfactant system. (Reproduced from Reference 88. Copyright (2014) Wiley. Used with permission from Kronberg, B.; Holmberg, K.; Lindman, B., *Surfactant-Polymer Systems, Surface Chemistry of Surfactants and Polymers*. Wiley)

There are two conditions to bind surfactants and polymers. If a surfactant is ionic, it has attractive interaction with an oppositely charged polymer or a slightly hydrophobic nonionic polymer. If a polymer contains hydrophobic segments, it can bind with all types of surfactants by hydrophobic associations. A polymer with a

water-soluble backbone and hydrophobic groups has strong interactions with surfactants, as shown in Figure 3.8. When there is only a polymer in water, the polymer has weak aggregation due to hydrophobic association. As a low concentration of a surfactant is introduced in this system, the surfactant interacts strongly with the hydrophobic segments of the polymer resulting in a stronger association between different individual polymer chains and a higher viscosity. With a further increase in the surfactant concentration, the hydrophobic groups of the polymer becomes saturated and each surfactant micelle can only contain one polymer hydrophobic group leading to disappearance of surfactant-associated cross-links and a decreased viscosity<sup>88</sup>.

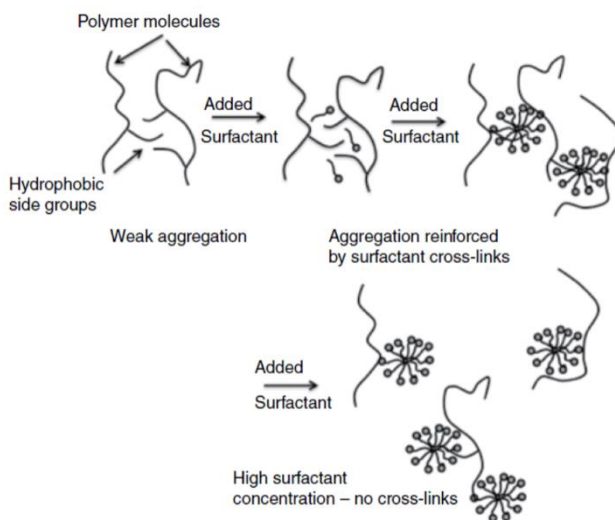


**Figure 3.8.** Depiction of the interaction between a hydrophobic-modified polymer and a surfactant. (Reproduced from Reference 88. Copyright (2014) Wiley. Used with permission from Kronberg, B.; Holmberg, K.; Lindman, B., *Surfactant–Polymer Systems*, *Surface Chemistry of Surfactants and Polymers*. Wiley)

## 3.5 Adsorption on Solid Surfaces

### 3.5.1 Adsorption of surfactants on solid surfaces

Surfactants have different adsorption behaviors on hydrophobic and hydrophilic solid surfaces. Figure 3.9 (a) shows the schematic of the adsorption of a surfactant on a hydrophobic surface, which is driven by two parts: interaction between surfactant hydrophobic chains and the solid surface, and interaction between different surfactant hydrophobic chains. The adsorption relates to the surfactant concentration. When the surfactant is at a very low concentration, its hydrophobic chains lay flat on the surface, driven by the hydrophobic effect. Whereas, when the

concentration is significantly increased, the surfactants are forced to stand up with the hydrophobic chain contacting with the solid surface to form a monolayer.

Figure 3.9 (b) illustrates the adsorption of a surfactant on a hydrophilic surface and this adsorption behavior relates to the surfactant concentration as well. At a low concentration, the surfactant molecules are laying down individually on the solid surface. If the surfactant is ionic and the solid surface is oppositely charged, the driving force of this adsorption is ion exchange. When the concentration of the surfactant increases to reach the critical surface association concentration, the surfactants start to self-assemble into micelles, where the head groups of the surfactants interact with the solid surface. As the concentration of the surfactant continuously increases above its CMC, a surfactant bilayer forms.

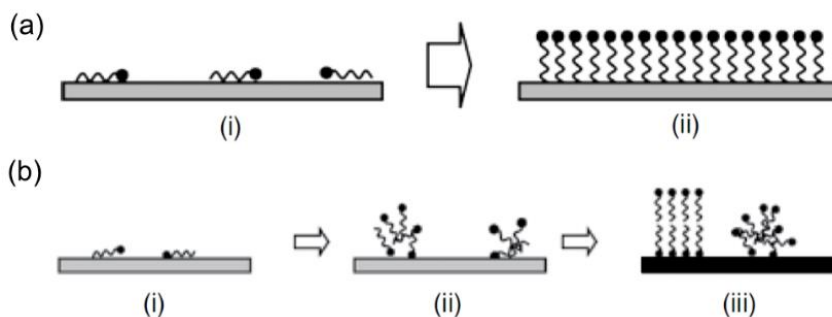


**Figure 3.9.** (a) Surfactant adsorption on a hydrophobic surface, where (i) is at a low concentration of the surfactant and (ii) is at a high concentration of the surfactant. (b) Surfactant adsorption on a hydrophilic surface, where the concentration of the surfactant is (i) low, (ii) middle and (iii) high. (Reproduced from Reference 88. Copyright (2014) Wiley. Used with permission from Kronberg, B.; Holmberg, K.; Lindman, B., *Surfactant Adsorption at Solid Surfaces, Surface Chemistry of Surfactants and Polymers*. Wiley)

Additionally, the efficiency of adsorption is associated with the CPP of a surfactant as well. Surfactants with different CPPs result in a variety of self-assembled structures including double layers, micelles and cylinders. Therefore, the surfactant aggregation structure on a solid surface can be controlled by tuning the length of hydrophobic chains, using surfactants with branched hydrocarbon tails or adding another type of surfactant<sup>88</sup>.

### 3.5.2 Adsorption of polymers on solid surfaces

Strong adsorption of a polymer on a solid surface is usually driven by an attraction between the polymer segments and the solid surface or a weak interaction between the solvent and the polymer. The adsorption of a polymer is related to its molecular weight and solubility. A polymer with high molecular weight and poor solubility has a stronger tendency to adsorb than that with low molecular weight and good solubility. Additionally, pH value also influences the adsorption strength of a

polyelectrolyte on a charged solid surface. In general, polymer adsorption is divided into three steps: (i) a polymer diffuses from the solvent to the solid surface, (ii) the polymer attaches to the surface and (iii) the polymer molecules rearrange to achieve the optimal attachment on the surface site.

Addition of a surfactant can alter adsorption behavior of a polymer by influencing its solubility. A surfactant can either increase or decrease the solubility of a polymer. Figure 3.10 illustrates that the adsorption of a surfactant-polymer mixture on a hydrophobic surface changes with an increase of the surfactant concentration. In the system with only polymers, shown in Figure 3.10 (i), the hydrophobic groups of the polymer attach strongly on the solid surface leading to a compact polymer conformation. When a surfactant is added, it forms micelles around the hydrophobic groups of the polymer and distributes on the solid surface, resulting in a decrease of the adsorbed amount of the polymer. With a continuous increase of the surfactant concentration, the formation of a surfactant monolayer on the solid surface and a saturated attachment of surfactant molecules on the hydrophobic groups of the polymer make the polymer desorb from the solid surface. However, for the polymer that has weak adsorption, addition of a surfactant with a proper concentration can strengthen polymer adsorption through good attachment of the surfactant with both the polymer and the solid surface<sup>88</sup>. For example, PVP molecules present no adsorption on an iron(III) oxide ( $\text{Fe}_2\text{O}_3$ ) surface but the addition of sodium dodecyl sulfate with proper concentration promotes the adsorption of PVP<sup>97</sup>.

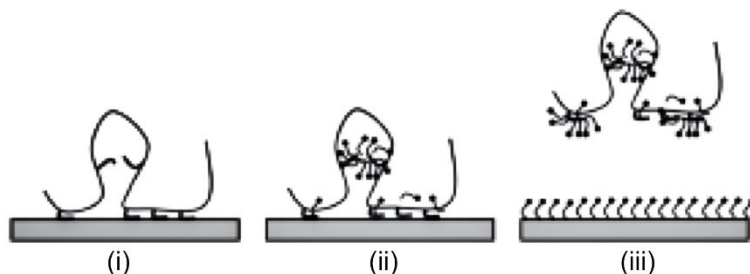


**Figure 3.10.** Schematic of the adsorption of a surfactant-polymer complex on a hydrophobic surface for: (i) only polymer; (ii) polymer with surfactant at low concentration; (iii) polymer with surfactant at high concentration. (Reproduced from Reference 88. Copyright (2014) Wiley. Used with permission from Kronberg, B.; Holmberg, K.; Lindman, B., *Surfactant–Polymer Mixtures at Interfaces*, *Surface Chemistry of Surfactants and Polymers*. Wiley)



# Chapter 4 Transmission Electron Microscopy Techniques

Microstructures of Pd and Au nanoparticles in this thesis were mainly investigated with transmission electron microscopy (TEM). In this chapter, TEM and additional techniques which use a transmission electron microscope are introduced. Miller indices, which are used to characterize crystal lattice planes and orientations, are presented as well. In this thesis, TEM images with various magnifications were used to study morphologies of metal nanoparticles. High-resolution TEM and scanning transmission electron microscopy were used to investigate microstructure and strain in the nanoparticles. The lattice structure of the metal nanoparticles was studied by selected area electron diffraction and Kikuchi patterns. The chemical composition of the metal nanoparticles was investigated by energy dispersive X-ray spectroscopy.

## 4.1 Transmission Electron Microscopy

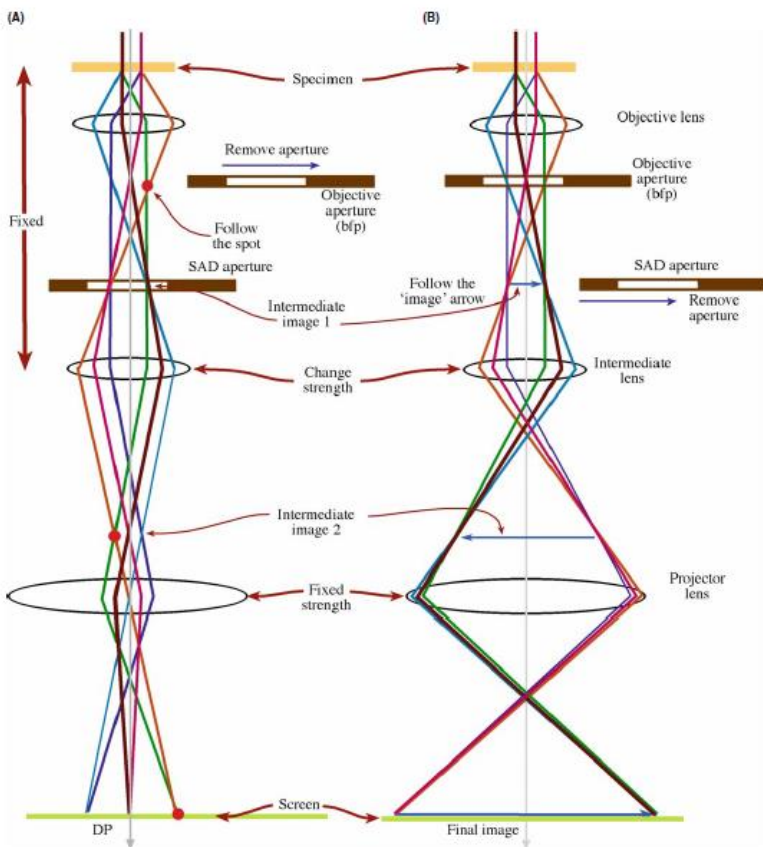
Transmission electron microscopy (TEM) is a modern microscopy technique where an electron beam is used to image specimens. The electron beam in TEM is accelerated by a high acceleration voltage generally ranging from 200 to 300 kV, leading to an extremely short wavelength (less than 3 pm)<sup>98</sup>. This wavelength is with an order of magnitude smaller than that utilized in optical microscopy, which operates in the visible light region (around 400 to 700 nm). Since the spatial resolution of a microscope is related to the wavelength of its light source, TEM can have a spatial resolution of around 0.1 nm, which is influenced by instabilities and lens aberration of the TEM as well<sup>98</sup>. Compared to an optical microscope, TEM can provide more detailed structure information for specimens. Therefore, TEM is widely used to study morphology, interface and internal atomic structure and composition.

During imaging, the electron beam is transmitted through the sample and the interaction with the sample generates an image. After that, the electrons containing the image information are magnified by several levels of electromagnetic lens and focused on an imaging device<sup>99</sup>. This process requires a sample thinner than 100 nm.

## 4.2 Diffraction and Image Modes

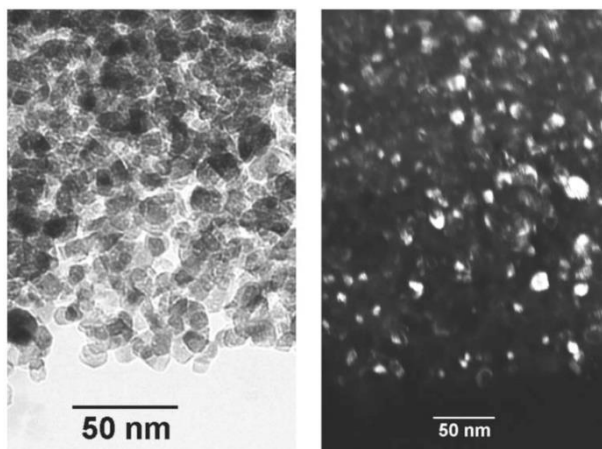
Diffraction and image modes are two basic operations in TEM, which can be switched by a button on the TEM console. The schematic of electron paths for both modes are displayed in Figure 4.1.

Figure 4.1 (a) describes the formation of selected area electron diffraction pattern (SAED), which is an important crystallographic technique. SAED is operated by inserting a selected-area diffraction (SAD) aperture to select the region to take diffraction patterns. When the incident electron beam with high energy is directed towards this selected region, most of the electrons pass through the sample but a fraction of the electrons are scattered by sample atoms, changing direction, an effect which is governed by the lattice structure of the sample. The electrons scattered by the same group of lattice planes are focused into a spot on the back focal plane (bfp) through the objective lens, forming regular patterns, called diffraction patterns, which contains the structure information of the sample region. In the TEM diffraction mode, the imaging-system lenses are adjusted to take the back focal plane as the object plane for the intermediate lens and finally project the diffraction pattern on the viewing screen to be recorded<sup>98</sup>.



**Figure 4.1.** Schematic of electron paths for (a) diffraction mode and (b) image mode. SAD represents selected-area diffraction and the bfp is short for the back focal plane. Reproduced from Williams, D. B.; Carter, C. B., 1996, *Transmission Electron Microscopy: A Textbook for Materials Science, Diffraction in TEM*, with the permission from Springer Nature<sup>98</sup>.

In Figure 4.1 (b), the incident electron beam is the same as the beam in the diffraction mode at the beginning interacting with the sample atoms and then the scattered and transmitted electron beams form not only a diffraction pattern on the back focal plane but also an image in an image plane, where the SAD aperture is set. In the TEM image mode, this image plane is selected for the intermediate lens as the objective plane through adjusting the imaging-system lenses and is projected on the viewing screen finally. Therefore, the correlation between a diffraction pattern and an image gives information about lattice planes and orientations<sup>98</sup>.



**Figure 4.2.** TEM images of mesoporous anatase powders. (a) Bright field image. (b) Dark field image. Reproduced from Kartini, I.; Meredith, P.; Costa, J. C. D. D.; Lu, G. Q., A Novel Route to the Synthesis of Mesoporous Titania with Full Anatase Nanocrystalline Domains. *Journal of Sol-Gel Science and Technology* 2004, 31, 185–189, with the permission from Springer Nature<sup>100</sup>.

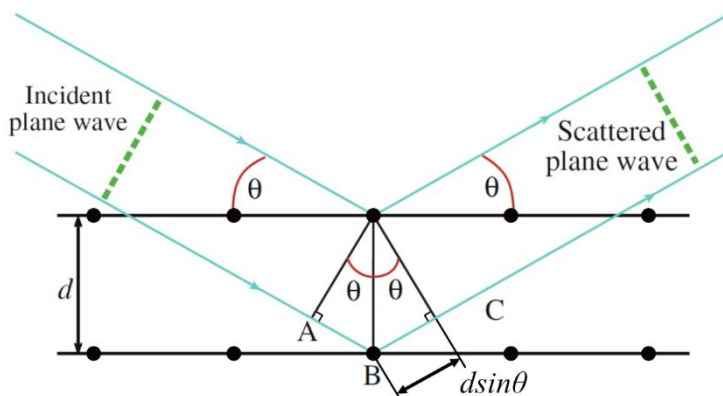


**Figure 4.3.** Schematic of Bragg's Law. Reproduced from Williams, D. B.; Carter, C. B., 1996, *Transmission Electron Microscopy: A Textbook for Materials Science*, Elastic Scattering, with the permission from Springer Nature<sup>98</sup>.

Additionally, the objective aperture set on the back focal plane can be inserted to allow either transmission or diffraction spots passing through. If only the

transmission spot is selected and diffraction spots are blocked by the aperture, the formed image is a bright field image, in which the region with strong effect on scattering electrons appears dark. Oppositely, the image formed only by diffraction spots is a dark field image, in which transmitted area and the region that do not scatter electrons for the selected diffraction spots present dark. Both bright field and dark field images enhance the image contrast through the filtration of some electrons. Especially, the dark field image can be used to study crystal defects and dislocations<sup>101</sup>. A comparison of bright field and dark field images from the same region is shown in Figure 4.2<sup>100</sup>.

A crystal is composed of an infinite number of highly ordered atoms with a geometrical shape. These atoms form flat lattice planes with characteristic orientations. A group of parallel lattice planes with a same spacing between two adjacent planes are a set of planes. When an electron beam is incident on a crystal in TEM, only the set of planes in a direction that satisfies Bragg's Law enhance the intensity of the scattered electron beam, resulting in diffraction. A diffraction pattern records the intensities of scattered electron beams on the back focal plane. Bragg's Law can be represented as:

$$2d \sin \theta = n\lambda \quad (4.1)$$

Where  $d$  is the interplanar distance of a set of lattice planes,  $\theta$  is defined as the Bragg angle, which is an angle between the incident electron beam and the diffracting lattice planes, as seen in Figure 4.3,  $n$  is a positive integer and  $\lambda$  is defined as the wavelength of the incident electron beam.

As shown in Figure 4.3, two parallel electron beams with a same wavelength are scattered by two atoms located in adjacent lattice planes, respectively. The lower electron beam travels an extra length of  $2d \sin \theta$  than the upper beam. If the path length difference is an integral multiple of the electron beam wavelength, two scattered electron beams still have the same phase, leading to constructive interference and giving rise to diffraction<sup>98</sup>.

Single crystals, polycrystals and amorphous materials have different characteristics on SAED patterns, as shown in Figure 4.4, which can provide quantitative data of lattice structure. In order to identify indices of lattice planes for diffraction spots of single crystal in Figure 4.4 (a), the distance between centers of a diffraction spot and the transmission spot is measured as  $r_i$  ( $i = 1, 2$  or  $3$ ) 1/nm. Then the value of  $(1/r_i)$  nm is the interplanar spacing of the lattice plane corresponding to the diffraction spot. If the diffraction pattern was taken from a known material, such as Pd crystal in Figure 4.4 (a), the indices of a lattice plane correlated to a diffraction spot in the diffraction pattern can be identified by comparing its interplanar spacing to the standard values of lattice planes for this material. If the distances between the transmission spot and three different diffraction spots,  $r_1$ ,  $r_2$  and  $r_3$ , the angle between  $r_1$  and  $r_2$ , and the angle between  $r_2$  and  $r_3$  are measured, the indices of the

entire diffraction pattern can be identified. In the polycrystalline diffraction pattern in Figure 4.4 (b), diffraction spots located on the same diffraction ring have the same indices. The radius of a diffraction ring,  $r$  1/nm, is measured and then its corresponding interplanar spacing is calculated by  $(1/r)$  nm. Comparing to the standard interplanar spacings of lattice planes for the material, which this diffraction pattern was taken from, the indices of the diffraction can be determined<sup>98</sup>.

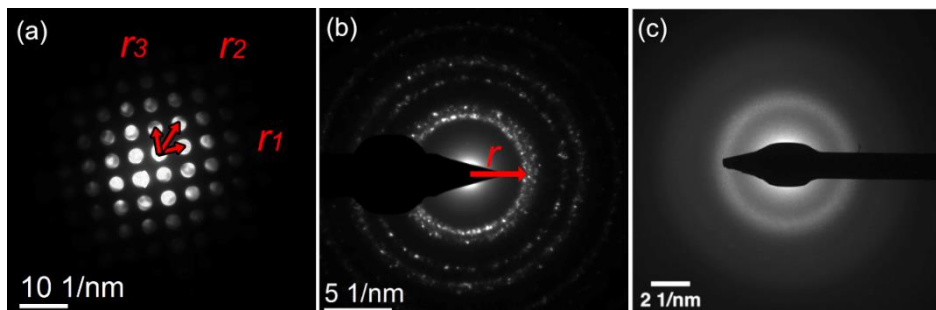


**Figure 4.4.** Diffraction patterns for: (a) Pd single crystal, where the red arrows start from the transmission spot and point to a diffraction spot. The distance between the transmission spot and diffraction spots are represented as  $r_1$ ,  $r_2$  and  $r_3$ , respectively. (b) Pd polycrystals, where the red arrow stands for the radius of the inner diffraction ring and its value is  $r$ . (c) Frozen amorphous electrolyte, which is a frozen mixture of lithium hexafluorophosphate ( $\text{LiPF}_6$ ), ethylene carbonate and dimethyl carbonate. The figure in (c) is reproduced from Zachman, M. J.; Tu, Z.; Choudhury, S.; Archer, L. A.; Kourkoutis, L. F., *Cryo-STEM Mapping of Solid–Liquid Interfaces and Dendrites in Lithium-Metal Batteries*. *Nature* 2018, 560, 345–349, with the permission from Springer Nature<sup>102</sup>.

### 4.3 Kikuchi Pattern

Kikuchi patterns are another crystallographic diffraction technique which can be operated on a TEM. Kikuchi lines are pairs of parallel lines formed by the Bragg diffraction of the inelastically scattered electrons generated from the incident electron beam passing through the sample<sup>103-104</sup>. Kikuchi lines from the same zone axis intersect at a core forming a flowery pattern, called the Kikuchi pattern (as shown in Figures 9.4 and 9.5 in Chapter 9). Kikuchi patterns contains information about crystal structures, and when compared to SAED, Kikuchi patterns are more sensitive to the tilting of the specimen at a small angle<sup>105-106</sup>.

The formation of Kikuchi lines is shown in Figure 4.5. When an electron beam is incident on a crystal specimen, the electrons can be scattered in all directions at a single point. As shown in Figure 4.5 (a), the vector length of a scattered electron path expresses how much possibility of the scattered electrons would pass through this direction, indicating that most of the electrons are scattered with a small angle. However, some of the scattered electrons move along a direction that forms the Bragg angle with the lattice planes, resulting in an occurrence of Bragg diffraction,

which exists on both sides of a lattice plane, as seen in Figure 4.5 (b). Because the scattered electrons traverse in all directions in space, all scattered electron beams that satisfy Bragg's Law form two conical surfaces, called Kossel cones, displaying on both sides of a lattice plane, as shown in Figure 4.5 (c). The projections of two Kossel cones are approximate to two parallel straight lines in the diffraction pattern, where the line close to the direction of the incident beam is dark (deficient line) and the other line is bright (excess line)<sup>98</sup>.

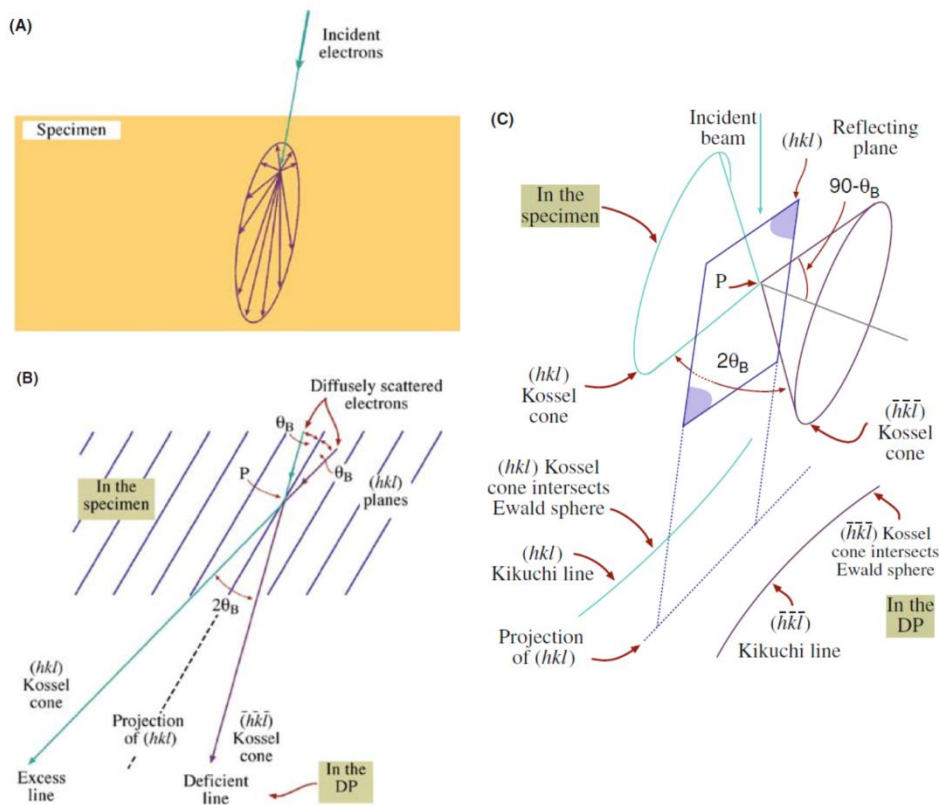


**Figure 4.5.** Depiction of the formation of Kikuchi lines. (a) Incident electrons are scattered in all directions at a point in the specimen. (b) Bragg diffraction occurs when the angle between the scattered electron beam and the lattice plane is equal to the Bragg angle. DP is short for diffraction pattern. (c) All diffracted electron beams caused by Bragg diffraction form two conical surfaces in space, called Kossel cones. Projections of the Kossel cones are approximate to two parallel straight lines. Reproduced from Williams, D. B.; Carter, C. B., 1996, Transmission Electron Microscopy: A Textbook for Materials Science, Kikuchi Diffraction, with the permission from Springer Nature<sup>98</sup>.

When an incident electron beam is scattered at a single point  $O$  on the lattice plane. The point  $O$  is taken as a center to construct a sphere of radius  $1/\lambda$ , where  $\lambda$  is the wavelength of the incident electron beam. This sphere is called Ewald sphere, used

to correspond diffraction spots to their relative lattice planes. As shown in Figure 4.6 (a), when the angle between the incident electron beam and the lattice planes is equal to Bragg angle  $\theta$ , the transmitted electron beam passes through the specimen and reaches at point  $O_2$  in the view screening, and the scattered electron beam goes towards point  $A_2$  in the view screening, deviating from the transmitted electron beam with angle  $2\theta$ . The point  $A_2$  is where the diffraction is observed. Through Ewald sphere, the distance ( $R$ ) between the transmission spot and the diffraction spot can be associated with the interplanar spacing ( $d$ ) of lattice planes<sup>98</sup>.

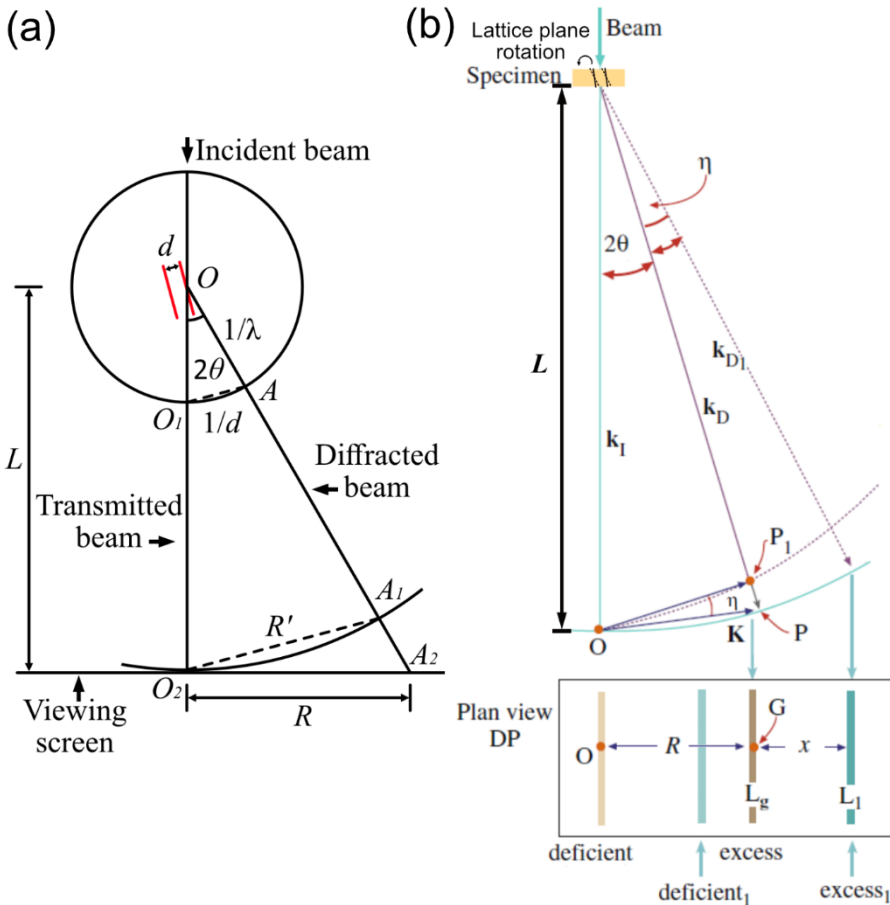


**Figure 4.6.** (a) Ewald sphere related to a diffraction pattern. (b) Displacement of Kikuchi lines caused by a rotation of lattice planes with a small angle  $\eta$ . Diffraction spots do not move by the rotation but their intensities change.  $d$  is the interplanar spacing of lattice planes,  $\lambda$  is the wavelength of the incident beam,  $\theta$  is the Bragg angle and  $L$  is the camera length. DP is short for diffraction pattern. The image in (b) is reproduced from Williams, D. B.; Carter, C. B., 1996, Transmission Electron Microscopy: A Textbook for Materials Science, Kikuchi Diffraction, with the permission from Springer Nature<sup>98</sup>.

First, the distance between  $O_1A$  can be calculate by Bragg's Law with  $n = 1$  (Eq 4.1), which value is  $1/d$ . Camera length  $L$  is the distance between the specimen and the viewing screen. Based on the geometric rules of similar triangles:  $\triangle OO_1A \sim \triangle OO_2A_1$ , an equation can be deduced:

$$R'd = L\lambda \quad (4.2)$$

Since the angle  $\theta$  is generally very small and the camera length  $L$  is relatively large, the points  $A_1$  and  $A_2$  are very close. Therefore, the value of  $R$  is approximate to  $R'$ . The association between  $R$  and  $d$  can be expressed as:

$$Rd = L\lambda \quad (4.3)$$

Ewald sphere can also be applied in Kikuchi lines, where  $R$  is the distance between deficient and excess lines. When the crystal lattice planes rotate in a small angle ( $\eta$ ) along an axis perpendicular to the incident beam, the pair of Kikuchi lines are also shifted a distance of  $x$ , as shown in Figure 4.6 (b)<sup>98</sup>. The distance  $x$  is measured on the diffraction pattern recorded from the viewing screen. Then the rotation angle can be deduced by the equation as below:

$$x = L\eta \quad (4.4)$$

With a combination of Eq 4.3 and Eq 4.4, rotation angle of the lattice planes can also be represented as:

$$\eta = \frac{x\lambda}{Rd} \quad (4.5)$$

This equation was used to determine the bent angle of Au nanorods in Chapter 9.

#### 4.4 Energy Dispersive X-ray Spectroscopy

Energy dispersive X-ray spectroscopy (EDS) is an analytical technique set in a TEM or a scanning electron microscope (SEM), which is used for compositional analysis. As seen in Figure 4.7, when an atom of a specimen is bombarded with high-energy incoming electrons, some of the electrons interact with the inner shell electron of the atom, resulting in an inelastic scattering. The inner shell electron is ejected from the atom after absorbs energy from the incoming electron and left a vacancy. Then an outer shell electron falls into this vacancy and emits a characteristic X-ray signal that contains specific elemental information. These characteristic X-ray signals are detected by specialized EDS detectors and the energies of the X-ray peaks correspond to the elements that exist in the detected region. This technique can provide quantitative compositional information about the detected area<sup>98</sup>.

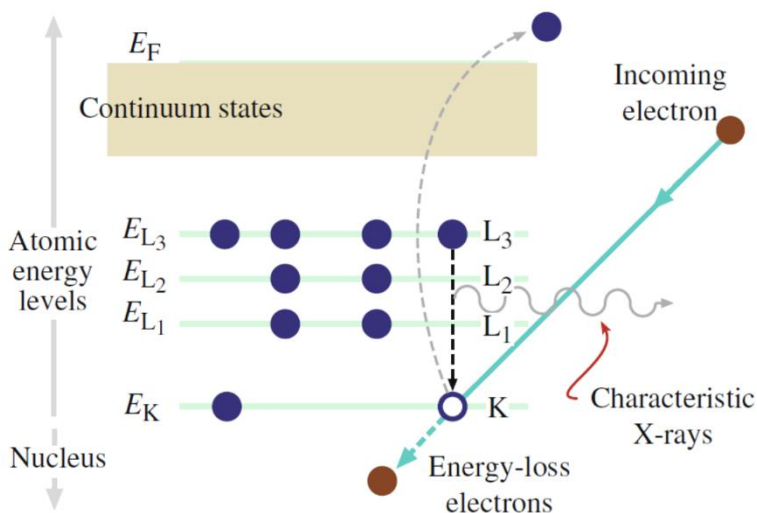


**Figure 4.7.** Schematic of characteristic X-ray emission. Reproduced from Williams, D. B.; Carter, C. B., 1996, *Transmission Electron Microscopy: A Textbook for Materials Science, Inelastic Scattering and Beam Damage*, with the permission from Springer Nature<sup>98</sup>.

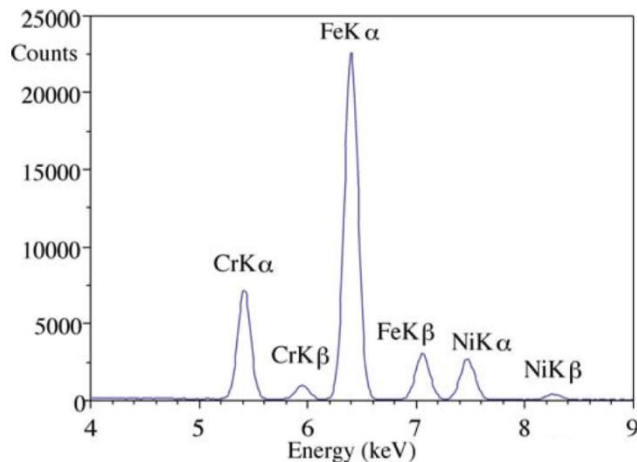


**Figure 4.8.** EDS spectrum from a stainless-steel foil specimen. Reproduced from Williams, D. B.; Carter, C. B., 1996, *Transmission Electron Microscopy: A Textbook for Materials Science, Qualitative X-ray Analysis and Imaging*, with the permission from Springer Nature<sup>98</sup>.

An EDS spectrum is shown in Figure 4.8 as an example, in which the abscissa is energy of characteristic X-ray and the ordinate is X-ray count. Unique peaks of each element are generated at specific energies, which is used to identify the type of elements.  $K_{\alpha}$  and  $K_{\beta}$  represent that the characteristic X-ray signals are emitted by an electron transition from L and M electron shells to K electron shell, respectively. The intensity of characteristic peak is utilized for the chemical composition analysis, which can be completed by EDS analytical software in computer<sup>98</sup>.

## 4.5 Scanning Transmission Electron Microscopy

Scanning transmission electron microscopy (STEM) is based on a conventional TEM equipped with additional scanning accessories. A typical TEM with STEM function is allowed to switch between both modes. In STEM mode, the electron beam is focused to a small spot with size around 0.05 - 0.2 nm on the sample and scans over the sample region spot by spot. The intensity of scanning signals is recorded with an annular detector and imaged in a focal plane. Two of the most common imaging modes are annular dark-field imaging and bright-field imaging. In dark-field imaging, images are generated by the fore-scattered electrons formed from the interaction between incident electrons and the sample, which is collected by an annular detector. Compared to a normal annular dark-field detector, a high-angle annular dark-field detector can provide a higher resolution to form atomic resolution images, where the atomic column contrast corresponds to the atomic numbers of the elements<sup>107</sup>. Therefore, this detector is often used to take high-resolution STEM images. In bright-field imaging, a bright-field detector is set to detect the transmitted electrons after the interaction with the sample, obtaining atomic resolution images, even for light elements such as oxygen<sup>108</sup>.

## 4.6 Electron Beam Damage

Electron beam damage is generally resulted from electron-electron or electron-atom interactions, in which the momentum and energy of a high-energy electron are transferred to an atom in the specimen by collision, resulting the specimen damage. Phenomena of beam damage strongly depend on the material<sup>109</sup>. Radiolysis, displacement and thermal damages are three common damage classes. Radiolysis is resulted from electronic ionization and excitations, forming highly chemical-reactive radicals<sup>110</sup>. Displacement damage causes atom displacement by the electron-atom collision<sup>111</sup>. The electron beam also has heating effects on specimens, leading to a phase transformation or decomposition<sup>112</sup>. Even through these damages are disadvantageous to many TEM experiments, they can be utilized to cause the changes in samples<sup>113-114</sup>.

## 4.7 Miller Indices

Miller indices are widely employed to define lattice planes and orientations of crystals in crystallography. In general, the coordinate system consists of three basic vectors **a**, **b** and **c** towards different directions in space, which can represent any vectors in the space by adding proper indices for basis vectors. For example, a vector **r** originating from the origin of coordinate to a lattice point in space is represented as:

$$\mathbf{r} = u \mathbf{a} + v \mathbf{b} + w \mathbf{c} \quad (4.6)$$

Where  $u$ ,  $v$  and  $w$  are integers.  $[uvw]$  is the Miller index of the vector  $\mathbf{r}$ .

It is more complex to describe Miller indices of a lattice plane. In the first step, three intercept vectors of the lattice plane on three coordinate axes are counted, expressed as  $(\frac{1}{h}\mathbf{a}, \frac{1}{k}\mathbf{b}, \frac{1}{l}\mathbf{c})$ . If the lattice plane is parallel to one of the coordinate axes, the intercept on this axis equals to  $\infty$ . After that, the reciprocals of the indices of three basis vectors are calculated as  $(hkl)$ , which is the Miller index of this lattice plane. There are always integral numbers for Miller indices. A negative value is marked with a bar on top of this number.

A family of orientations that share the same absolute value but different orders of Miller indices are equivalent due to periodic symmetry of crystal structures. This group of orientations is represented as  $\langle uvw \rangle$ , called a family of lattice directions. Likewise, a family of lattice planes which share the same absolute value but different orders of Miller indices are represented as  $\{hkl\}$ . Miller indices form a simple notation system to express complex crystal geometry relations.

Pure Pd, Au and Ag crystals all belong to the face centered cubic (FCC) structure, one of the most common lattice structures. As shown in Figure 4.9, there are atoms at the center of each facet and at the eight corners in a typical FCC unit cell. Three basis vectors ( $\mathbf{a}$ ,  $\mathbf{b}$  and  $\mathbf{c}$ ) corresponding to lattice directions of  $[100]$ ,  $[010]$  and  $[001]$  form a rectangular coordinate system. Miller indices  $[111]$  are denoted with the diagonal direction of the cubic unit starting from the origin of the coordinate. Four lattice planes with low indices are marked by colors: red is  $(111)$ ; yellow is  $(100)$ ; green is  $(010)$  and blue is  $(001)$ .

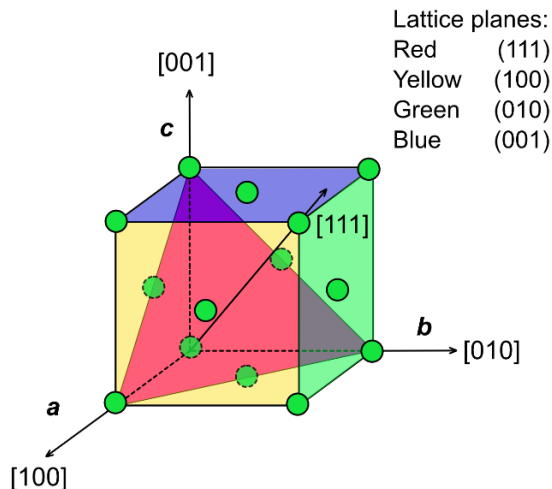


**Figure 4.9.** Unit cell of FCC structure, applicable for Pd, Au and Ag crystals.



# Chapter 5 Experimental Methods

In this chapter, chemicals, synthesis procedures and characteristic techniques related to the experiments are introduced.

## 5.1 Materials

Hexadecyltrimethylammonium bromide (CTAB,  $\geq 99\%$ ), sodium stearate (NaST,  $\geq 99\%$ ), polyvinylpyrrolidone (PVP,  $M_w=55000$ ), hydrogen tetrachloroaurate(III) trihydrate ( $\text{HAuCl}_4$ ,  $\geq 99.9\%$ ), silver nitrate ( $\text{AgNO}_3$ ,  $\geq 99.0\%$ ), silver trifluoroacetate ( $\text{CF}_3\text{COOAg}$ ,  $98\%$ ), palladium (II) chloride ( $\text{PdCl}_2$ ,  $99.999\%$ ), sodium tetrachloropalladate(II) ( $\text{Na}_2\text{PdCl}_4$ ,  $98\%$ ), palladium (II) acetylacetonate ( $\text{Pd}(\text{acac})_2$ ,  $99\%$ ), L-ascorbic acid (AA,  $\geq 99\%$ ), sodium hydroxide ( $\text{NaOH}$ ,  $\geq 97.0\%$ ), sodium hydrosulfide hydrate ( $\text{NaHS}\cdot x\text{H}_2\text{O}$ ) and sodium borohydride ( $\text{NaBH}_4$ ,  $\geq 98.0\%$ ) were purchased from Sigma Aldrich. Hydrochloric acid ( $\text{HCl}$ , 37 wt. % in water) was obtained from VWR Chemicals. Sodium oleate ( $\text{NaOL}$ ,  $> 97.0\%$ ) was purchased from Tokyo Chemical Industry. Hexadecyltrimethylammonium chloride (CTAC,  $99\%$ ) was purchased from Acros Organics of Fisher Scientific. Nitric acid ( $\text{HNO}_3$ , 70 wt. %) was obtained from Fisher Chemical. Acetone ( $\geq 99.8\%$ ) and methanol ( $\geq 99.9\%$ ) were purchased from Fisher Scientific. Ethylene glycol (EG,  $\geq 99\%$ ) was obtained from J. T. Baker Chemical (Avantor Performance Materials, LLC).

All aqueous solutions were prepared with ultrapure water ( $18.2 \text{ M}\Omega$ ), which is purified with a Milli-Q Advantage A10 water purification system from Merck. EPA screw neck glass vials (20 mL) were obtained from Fisherbrand<sup>TM</sup>. All laboratory glassware and magnetic bars used for synthesis were cleaned by freshly prepared aqua regia, the preparation of which is described below.

After preparation, CTAB, CTAC and NaOL aqueous solutions were kept in a water bath at  $40^\circ\text{C}$  before use. NaST aqueous solution was stored in a water bath at  $80^\circ\text{C}$ .  $\text{NaBH}_4$  was freshly prepared and stored in an ice bath before use. In order to avoid degradation due to light,  $\text{AgNO}_3$  and  $\text{CF}_3\text{COOAg}$  were stored in containers covered by aluminum foil.

### 5.1.1 Preparation of $\text{H}_2\text{PdCl}_4$ solution

A 10 mM  $\text{H}_2\text{PdCl}_4$  aqueous solution was prepared by the following steps. First, 0.166 mL of  $\text{HCl}$  (37 wt.%) was diluted into 9.834 mL of ultrapure water to make 10 mL of 0.2 M  $\text{HCl}$  solution. Second, 0.1773 g of  $\text{PdCl}_2$  was added to the  $\text{HCl}$  solution. When the  $\text{PdCl}_2$  solid was completely dissolved, the mixture of  $\text{PdCl}_2$  and

HCl was diluted by adding 90 mL water to form a total of 100 mL of 10 mM  $\text{H}_2\text{PdCl}_4$  solution<sup>115</sup>.

### **5.1.2 Preparation of $\text{Pd}(\text{acac})_2$ solution**

Since  $\text{Pd}(\text{acac})_2$  is insoluble in water but soluble in methanol, 10 mM  $\text{Pd}(\text{acac})_2$  in water was prepared by first mixing 15.23 mg of  $\text{Pd}(\text{acac})_2$  in 5 mL of ultrapure water. Then, 10 mL of methanol was added to assist in the dissolution of  $\text{Pd}(\text{acac})_2$ . The mixture was mixed well on a vortex (Scientific Industries Vortex Genie 2) for 5 minutes and then used in the reaction directly to prevent methanol reduction of the Pd ions.

### **5.1.3 Preparation of aqua regia**

Aqua regia is a mixture of hydrochloric acid and nitric acid, which can dissolve Au and Pd metals<sup>116</sup>. Aqua regia was prepared by adding  $\text{HNO}_3$  (70 wt. %) gradually into HCl (37 wt. %) according to the  $\text{HNO}_3/\text{HCl}$  volume ratio 1:3, forming a yellow-orange fuming liquid which is freshly prepared before use.

## **5.2 Synthesis of Pd Nanodendrites Stabilized by CTAB and NaOL**

### **5.2.1 Seed solution**

10 mL of 12.5 mM CTAB aqueous solution was transferred to a clean 20 mL glass vial in an oil bath at 95 °C and stirring at a speed of 400 rpm. After that, 0.5 mL of 10 mM  $\text{H}_2\text{PdCl}_4$  was added into the CTAB solution. 5 minutes later, 80  $\mu\text{L}$  of 100 mM AA was injected into the CTAB-Pd mixture. The solution stirred continuously and aged at 95 °C for 30 minutes until use. The Pd seed solution was freshly prepared for each synthesis process in order to prevent the seeds from degradation within a few hours after preparation<sup>50</sup>.

### **5.2.2 Growth solution**

Certain volumes of 50 mM CTAB and 50 mM NaOL aqueous solutions were transferred and mixed well in a 20 mL glass vial at room temperature according to different volume proportions of CTAB and NaOL to obtain a mixed solution with a total volume of 5 mL. CTAB and NaOL volumes and their molar ratios are shown in Table 6.1 of Chapter 6. In the following steps, 125  $\mu\text{L}$  of 10 mM  $\text{H}_2\text{PdCl}_4$ , 200  $\mu\text{L}$  of fresh Pd seed solution and 25  $\mu\text{L}$  of 100 mM AA were added, in sequence, into the surfactant solution and mixed intensively on a vortex (Scientific Industries

Vortex Genie 2) after adding each reagent. The mixture was incubated without stirring in a water bath at 40 °C for 14 hours, forming the final solution<sup>50</sup>.

This final solution was washed through centrifugation (VWR Micro Star 12) at 2400 RCF (6000 rpm) for 20 minutes. After removing the supernatant, a specific volume of ultrapure water, depending on the application of the Pd nanodendrites, was added.

The synthesis methods for the CTAC-NaOL and CTAB-NaST surfactant mixtures followed the same synthesis procedure as mentioned above except that the CTAB-NaOL solution was replaced by a mixture of 4 mL of 50 mM CTAC and 1 mL of 50 mM NaOL in CTAC-NaOL system, and a mixture of 4 mL of 50 mM CTAB and 1 mL of 50 mM NaST in CTAB-NaST system.

### **5.2.3 Preparation of TEM sample**

0.5 mL of the nanoparticle solution, which has been centrifuged once and refilled with ultrapure water to the same volume, was added into a 1.5 mL centrifuge tube. After centrifuge at 2400 RCF (6000 rpm) for 10 minutes, the supernatant was removed and a certain volume of ultrapure water (0.25 mL or 0.1 mL), determined by the amount of deposition, was added. After redispersing the Pd nanodendrites in the solution again, 5  $\mu$ L of this solution was dropped on a copper TEM grid with carbon film and dried at room temperature.

## **5.3 Synthesis of Hollow Ag-Pd Nanoparticles Stabilized by CTAC and NaOL**

### **5.3.1 Ag seed solution**

The synthesis of cubic Ag seeds was based on a published method<sup>117-118</sup>. All reagents involved in the synthesis were prepared with EG as the solvent.

In brief, 50 mL of EG was transferred into a 250 mL round bottom flask and kept in an oil bath at 150° for 1 hour while stirring at a speed of 550 rpm. After that, 0.6 mL of 3 mM NaHS (in EG) was injected into the heated solution, followed by adding 5 mL of 3 mM HCl solution (in EG) 4 minutes later, 12.5 mL of PVP solution (20 mg/mL in EG) after another 2 minutes and 4 mL of 282 mM CF<sub>3</sub>COOAg (in EG) after waiting 2 more minutes. This mixture was incubated at 150°C for 30 minutes, while stirring continuously. The flask outlet was covered for the entire synthesis apart from reagent addition. In order to prevent overgrowth of Ag seeds, the reaction container was transferred to an ice bath after the final 30-minute incubation.

Ag seeds required purification before further use. 7.5 ml of the Ag seed solution mixed with 42.5 ml of acetone in a 50 ml centrifuge tube, was centrifuged (Thermo Scientific™ Heraeus™ Multifuge™ X1 Centrifuge) at 4900 rpm (2797 RCF) for 8 minutes. After removing the supernatant, Ag seeds were dispersed in 1.5 ml of ultrapure water using a vortex (Scientific Industries Vortex Genie 2) and sonication (VWR Ultrasonic Cleaner USC600D) and then centrifuged (VWR Micro Star 12) again at 13500 rpm (12300 RCF) for 15 minutes. After the supernatant was removed, the Ag seeds were redispersed in 1 ml of ultrapure water for storage.

### **5.3.2 Growth solution of hollow Ag-Pd nanodendrites**

The method to grow Pd nanodendrites on Ag seeds was adapted from the growth on the Pd seeds<sup>50</sup>. 4 mL of 50 mM CTAC and 1 mL of 50 mM NaOL aqueous solutions were mixed well in a clean 20 mL glass vial. After that, 25  $\mu$ L of the Ag seed, 25  $\mu$ L of 100 mM AA and 125  $\mu$ L of 10 mM H<sub>2</sub>PdCl<sub>4</sub> aqueous solutions were added into CTAC-NaOL mixture in sequence. After thoroughly mixing on the vortex, the mixed solution was kept in a water bath at 40°C for 4 hours without stirring. The final growth solution was centrifuged (VWR Micro Star 12) at 12000 rpm (9700 RCF) for 10 minutes. The hollow Ag-Pd nanodendrites were dispersed in the same volume of ultrapure water for storage after removed the supernatant.

### **5.3.3 Growth solution of hollow Ag-Pd spiky-nanoboxes**

The synthesis of hollow Ag-Pd spiky-nanoboxes was performed by the same method as hollow Ag-Pd nanodendrites (described in 5.3.2) except that 375  $\mu$ L of Pd(acac)<sub>2</sub> solution (in mixture of water and methanol, as described above) was employed as the Pd precursor instead of H<sub>2</sub>PdCl<sub>4</sub>, with an equal mole of Pd. Since Ag-Pd spiky-nanoboxes grew more slowly than nanodendrites, the reagent mixture for spiky-nanoboxes was incubated in a water bath at 40°C for 22 hours instead of 4 hours.

### **5.3.4 Preparation of TEM sample**

1 mL of the growth solution that has been centrifuged once was centrifuged again at 12000 rpm (9700 RCF) for 10 minutes. The Ag-Pd nanoparticles were dispersed in 1 mL of ultrapure water after removing the supernatant. 5  $\mu$ L of this solution was dropped on a copper TEM grid with carbon film and let dry at room temperature.

## 5.4 Synthesis of Pd Nanodendrites Stabilized by PVP and NaOL

In a standard synthesis process, 2 mL of an aqueous solution containing 26.68 mg PVP ( $M_w = 55000$ ), 0.5 mL of 0.12 M NaOL and a certain amount of 2 M HCl or NaOH were added in sequence in a clean glass vial and mixed by stirring at a speed of 300 rpm overnight (>10 hours) at room temperature to form the PVP-NaOL mixture. The addition of HCl or NaOH was for tuning pH environment of the reaction system and its volume for each synthesis is shown in Table 5.1. The pH values were measured by Jenway 570 pH meter. Before the reaction, the glass vial containing the PVP-NaOL mixture was transferred to an oil bath at 80 °C and stirred at a speed of 400 rpm for 10 minutes for heating up. After that, 1 mL of 50 mM  $\text{Na}_2\text{PdCl}_4$  was added. After stirring for another 5 minutes, 85  $\mu\text{L}$  of AA solution was injected. The mixture was kept stirring at a speed of 400 rpm in the oil bath at 80 °C for 3 hours. The final solution was centrifuged (Thermo Scientific™ Heraeus™ Multifuge™ X1 Centrifuge) at 10000 rpm (11648 RCF) for 30 minutes. After removal of the supernatant, Pd nanoparticles were resuspended in ultrapure water to the same volume as before and mixed well in an ultrasonic bath (VWR Ultrasonic Cleaner USC600D) for 1 hour. This solution was stored at room temperature for further use.

**Table 5.1.** The volumes of added HCl and NaOH solutions and corresponding pH values of the PVP-NaOL mixtures.

Addition	2 M NaOH			2 M HCl										
	Volume ( $\mu\text{L}$ )	pH	Volume ( $\mu\text{L}$ )	Volume ( $\mu\text{L}$ )	pH	Volume ( $\mu\text{L}$ )	pH	Volume ( $\mu\text{L}$ )	pH					
Volume ( $\mu\text{L}$ )	275.0	12.36	27.5	0	24.5	7.06	31.5	3.35	42.0	2.03	120.0	1.17	420.0	0.60
pH	12.36		11.75	9.47	7.06		3.35		2.03		1.17		0.60	

### 5.4.1 Preparation of TEM sample

150  $\mu\text{L}$  of the stored Pd nanoparticle solution was added in an Eppendorf tube and centrifuged (VWR Micro Star 12) at 6000 rpm (2400 RCF) for 5 minutes. After removed the supernatant, the deposition was redispersed in 150  $\mu\text{L}$  of ultrapure water. A 5  $\mu\text{L}$  droplet of the Pd nanoparticle solution was dropped and dried on a TEM copper grid with a uniform carbon film.

## 5.5 Synthesis of Au Nanorods Stabilized by CTAB and NaOL

The synthesis of Au nanorods was followed the procedure reported by Xingchen Ye<sup>23</sup>.

### 5.5.1 Seed solution

1.25 mL of 0.5 mM HAuCl<sub>4</sub> and 1.25 mL of 0.2 M CTAB solution were mixed uniformly in a 20 mL glass vial at room temperature. After that, 0.8 mL of freshly prepared 3.75 mM NaBH<sub>4</sub> solution was injected into this Au (III)-CTAB mixture while stirring vigorously (1200 rpm) for 2 minutes. In these 2 minutes, the color of the solution changed from yellow to brownish. The seed solution was aged without stirring at room temperature for 30 min before use. The Au seed solution was always freshly prepared for each synthesis.

### 5.5.2 Growth solution

The Au growth solution was prepared as following steps. 0.875 g of CTAB and 0.154 g of NaOL were added in 31.25 mL of ultrapure water in a 250 mL Erlenmeyer flask, while stirring and heating at 50 °C in a water bath until dissolved completely. Concentrations of CTAB and NaOL in this mixed solution were 76.84 mM and 16.22 mM, respectively. After the solution cooled down to 30 °C, 3 mL of 4 mM AgNO<sub>3</sub> solution was added and kept undisturbed for 15 minutes. Then, 31.25 mL of 1 mM HAuCl<sub>4</sub> solution was added. The mixture was stirred at a speed of 700 rpm for 90 minutes and the solution became colorless. Then the solution was continuously stirred at a speed of 400 rpm for 15 minutes after the addition of 0.45 mL of HCl (37 wt. %). After adding 0.156 mL of 0.064 M AA, the solution was stirred vigorously (700 rpm) for 30 seconds. Lastly, 0.05 mL of seed solution was injected into the mixture. The growth solution was stirred at a speed of 400 rpm for 30 seconds and then kept without stirring in a 30°C water bath for 17.5 hours.

The final growth solution was centrifuged (Sigma laboratory centrifuge 4K15) at 4000 RCF (4340 rpm) for one hour. After removal of the supernatant, the deposition of Au nanorods was dispersed in the same volume of ultrapure water as before centrifugation and stored at room temperature.

### 5.5.3 Preparation of TEM sample

TEM samples for imaging Au nanorods were prepared in a simple way. First, 1 mL of the stored growth solution was centrifuged (VWR Micro Star 12) at 6000 rpm (2400 RCF) for 20 minutes. After removal of the supernatant, the deposition was resuspended in 0.5 mL of ultrapure water by mixing with a vortex (Scientific Industries Vortex Genie 2). A 5 µL droplet of the Au nanorod solution was dropped and dried on a TEM copper grid with lacey carbon film.

The TEM sample for imaging of standing Au nanorods was prepared by the following method. 0.25 mL of the stored Au nanorod solution was centrifuged at

6000 rpm (2400 RCF) for 5 minutes. The supernatant was removed and then 12  $\mu\text{L}$  of 0.04 M CTAB solution was added, mixing with the vortex. After centrifugation at 6000 rpm (2400 RCF) for 2 minutes, the supernatant was removed again and the deposition was vortexed without any additional solvent in order to obtain a very concentrated Au nanorod solution. 0.3  $\mu\text{L}$  of this concentrated Au nanorod solution was dropped at the center of a TEM grid with a uniform carbon film and dried.

## **5.6 Characterization**

The morphology, composition, crystal structure and other physical properties of metal nanoparticles and growth solutions were studied by various techniques including TEM, UV-Vis spectroscopy, dynamic light scattering spectroscopy, X-ray photoelectron spectroscopy and X-ray diffraction. These techniques are briefly introduced below.

### **5.6.1 Transmission electron microscopy**

Transmission electron microscopy (TEM) has been introduced in detail in Chapter 4., A FEI Tecnai T20 TEM operated at 200 kV, a FEI Titan 80-300 TEM operated at 300 kV and a JEM-ARM300F (JEOL Ltd.) operated at 300 kV were used in our experiments to study the morphologies, lattice structures and compositions of the metal nanoparticles in this thesis.

### **5.6.2 Ultraviolet-visible spectroscopy**

Ultraviolet-visible (UV-Vis) spectroscopy is an important technique to measure the absorbance of visible or ultraviolet light after passing a liquid or solid material. It records the intensities of the light before ( $I_0$ ) and after ( $I$ ) passing the sample for each wavelength in the selected range. All the ratios of  $I / I_0$  form a spectrum showing the absorption of the sample at different wavelengths of light. Metal nanoparticles have unique peaks at specific wavelengths in their absorbance spectra due to their LSPR properties which correspond to material, size and shape of the nanoparticles. In this thesis, UV-vis spectroscopy was used to analyze the particles and monitor the growth process of metal nanoparticles.

### **5.6.3 Dynamic light scattering and zeta potential measurements**

Dynamic light scattering (DLS) is an important technique to measure size distribution of small particles in suspensions and the same machine can be used to measure the zeta potential of colloidal dispersions. When the particles have a

smaller diameter than the wavelength of the incident laser light, the particles scatter the light in all directions. The scattering intensities fluctuate over time because of Brownian motion of the particles in solutions. These intensity fluctuations are traced by the equipment to measure the nanoparticle size. The zeta potential is a measurement of the electric potential difference between a bulk liquid medium and the stationary layer of the liquid medium attached to a dispersed particle, which determines the stability of nanoparticles in a suspension. A large absolute value of zeta potential indicates a strong repulsive force between two close particles, resulting a high stability in dispersed particles<sup>119</sup>.

## Chapter 6 Effects of Surfactant Ratios on the Growth of Pd Nanoparticles

In this chapter, a surfactant mixture of cationic CTAB and anionic NaOL was used in the seed-mediated growth of Pd nanodendrites to investigate the effects of surfactant molar ratio on the nanoparticle shape. Cationic CTAB is a conventional surfactant widely used in the growth of Pd nanocubes<sup>115</sup>. In order to modify the shape of Pd nanoparticles to increase their surface area, an anionic surfactant, NaOL, was introduced in the synthesis to rearrange the adsorption of CTAB molecules on the nanoparticle surface through interactions between opposite charges. In this chapter, the influence of the surfactant mixture ratio on the shape and yield of Pd nanoparticles is presented and the optimal ratio to fabricate Pd nanodendrites with relatively narrow size distribution was determined. Additionally, the formation mechanism of dendritic shape is discussed.

In order to study the influence of the CTAB-NaOL surfactant mixture on the yield and shape of Pd nanoparticles, a series of synthesis experiments were carried out with different molar ratios of CTAB and NaOL molecules but the same initial molar concentrations of each surfactant (50 mM) and total volume of the mixture. The amounts of each surfactant added in the growth solution and molar ratio  $\alpha_{\text{CTAB}}$  for each batch are displayed in Table 6.1. As the value of  $\alpha_{\text{CTAB}}$  reduces from 1 to 0, the amount of CTAB decreases and correspondingly, the amount of NaOL increases.

For comparison, zeta potential and conductance results of these mixed surfactant solutions are also reported in Table 6.1. Zeta potential is an important value to reflect the dispersion stability of nanoparticles. When the value of zeta potential is close to zero, nanoparticles are typically not stable in solutions<sup>120-121</sup>. Pure CTAB micelles have a relative zeta potential value of  $+60.9 \pm 5.9$  mV, indicating a strongly positive charges from the cationic head groups. By increasing the amount of NaOL in the solution, NaOL molecules were incorporated with the CTAB in the micelles and decreased the zeta potential. This is mainly because the oppositely charged NaOL head groups neutralize the charge of the CTAB micelles. The zeta potential values change suddenly from  $+8.66 \pm 5.9$  mV to  $-68.6 \pm 0.9$  mV when reducing  $\alpha_{\text{CTAB}}$  from 0.5 to 0.4. This illustrates that there is a critical molar ratio or concentration in this range at which the value of zeta potential becomes zero and the Pd nanoparticles in this solution are unstable.

The value of conductance also displays a maximum at around  $\alpha_{\text{CTAB}} = 0.4$ . The charge neutralization at this molar ratio results in an increase of the degree of counter-ion dissociation and more counterions ( $\text{Br}^-$  and  $\text{Na}^+$  ions) are freed to the solution, which contribute to the conductance. The change of the surfactant molar ratio rarely affects the surface tension of the solution since the initial concentrations of CTAB and NaOL in solution are much higher than their respective CMCs. The

maximum of conductance value was expected to appear at  $\alpha_{\text{CTAB}} = 0.5$  rather than 0.4, however, the existence of a double bond in the alkyl tail and conformational restriction of NaOL molecules may influence their accumulation in the mixed micelles and consequently, the double bond shifts the maximum to a lower  $\alpha_{\text{CTAB}}$  value.

**Table 6.1.** A surfactant mixture of CTAB and NaOL was employed for the preparation of the growth solution. The initial concentration of each surfactant was  $[\text{CTAB}] = [\text{NaOL}] = 50 \text{ mM}$ . The zeta potential and conductance of the mixture were measured at  $40 \text{ }^\circ\text{C}$ . (Reproduced with the permission from Wen, X.; Lerch, S.; Wang, Z.; Aboudiab, B.; Tehrani-Bagha, A. R.; Olsson, E.; Moth-Poulsen, K., Synthesis of Palladium Nanodendrites Using a Mixture of Cationic and Anionic Surfactants. *Langmuir* 2020, 36 (7), 1745-1753. Copyright 2020, American Chemical Society.) Conductance was measured by Bassem Aboudiab.

$\alpha_{\text{CTAB}}^{\text{a}}$	$V_{\text{CTAB}}$ (mL)	$V_{\text{NaOL}}$ (mL)	Zeta potential (mV)	Conductance (mS/cm)	Yield of Pd nanoparticles (mg/mL)
1	5	0	$60.9 \pm 5.9$	1.25	0.057
0.9	4.5	0.5	$55.6 \pm 11.0$	1.52	0.073
0.8	4	1	$38.9 \pm 1.6$	1.75	0.057
0.7	3.5	1.5	$37.5 \pm 1.2$	2.04	0.047
0.6	3	2	$36.2 \pm 7.2$	2.13	0.043
0.5	2.5	2.5	$8.66 \pm 5.9$	1.96	0.04
0.4	2	3	$-68.6 \pm 0.9$	2.4	0.127
0.3	1.5	3.5	$-73.8 \pm 1.0$	2.09	0.117
0.2	1	4	$-78.8 \pm 7.1$	1.86	0.057
0.1	0.5	4.5	$-78.4 \pm 8.8$	1.56	0.063
0	0	5	$-58.3 \pm 0.9$	1.35	0.023

<sup>a</sup>:  $\alpha_{\text{CTAB}}$  stands for the molar ratio between CTAB and CTAB-NaOL surfactant mixture. There is only CTAB at  $\alpha_{\text{CTAB}} = 1$  and only NaOL at  $\alpha_{\text{CTAB}} = 0$ .

Figure 6.1 displays the TEM images of Pd seeds and the nanoparticles synthesized by the surfactant volumes reported in Table 6.1. In the seed solution, nanocubes with an average size of  $24.1 \pm 3.4 \text{ nm}$  were produced, as shown in Figure 6.1 (seeds). These seeds continuously grew into larger nanocubes with an average size of  $56.7 \pm 6.0 \text{ nm}$  when the seed solution was added in the growth solution with only CTAB, following the standard procedure<sup>115, 122</sup>, as displayed in Figure 6.1 ( $\alpha_{\text{CTAB}} = 1$ ). However, by decreasing the molar ratio of in the growth solution, dendritic nanoparticles were formed instead of nanocubes, also shown in Figure 6.1 ( $\alpha_{\text{CTAB}} = 0.9$  to  $0.5$ ). These Pd nanodendrites have diameters in the range from 45 nm to 66 nm. Some of the Pd seed nanocubes can also be observed in the center of Pd nanodendrites through the different contrast in the TEM images, which are highlighted with red arrows in Figure 6.1 ( $\alpha_{\text{CTAB}} = 0.9$ ) and are also visible in Figure 6.1 ( $\alpha_{\text{CTAB}} = 0.8$  to  $0.5$ ). As the CTAB molar ratio is continuously decreased ( $\alpha_{\text{CTAB}}$

< 0.5), nanocubes from the Pd seed solution and much smaller crystals were observed in TEM respectively; however, no larger nanodendrites or nanoparticles were found in these samples, as shown in Figure 6.1 ( $\alpha_{CTAB} = 0.4$  to 0). This result indicates that, when the value of  $\alpha_{CTAB}$  is lower than 0.5, the attachment of reduced Pd<sup>0</sup> at the surface of the Pd seeds becomes inefficient and forms dispersed small crystals. These results illustrate that CTAB molecules, with the positively charged head groups, are crucial in the growth of Pd nanodendrites and nanocubes. When the concentration of CTAB molecules is lower than a critical value ( $\alpha_{CTAB} < 0.5$ ), the zeta potential of the mixed surfactant solution is negative and there is no more growth observed. Additionally, the yield of Pd nanodendrites reduces significantly as  $\alpha_{CTAB}$  approaches 0.5.

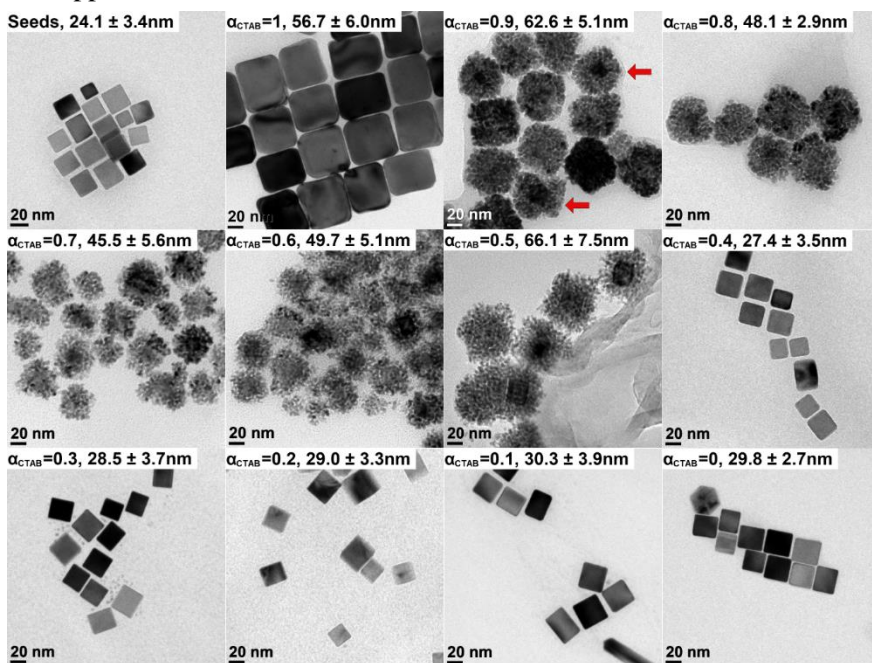


**Figure 6.1.** TEM micrographs of Pd seeds and the nanoparticles synthesized at various  $\alpha_{CTAB}$ . The value of  $\alpha_{CTAB}$  and the average of the particle size are marked on top of each image. (Reproduced with the permission from Wen, X.; Lerch, S.; Wang, Z.; Aboudiab, B.; Tehrani-Bagha, A. R.; Olsson, E.; Moth-Poulsen, K., Synthesis of Palladium Nanodendrites Using a Mixture of Cationic and Anionic Surfactants. *Langmuir* 2020, 36 (7), 1745-1753. Copyright 2020, American Chemical Society.)

By comparison of all molar ratios reported in Table 6.1, it is obvious that the synthesis at the value of  $\alpha_{CTAB}$  between 0.8 and 0.9 is optimal to produce Pd nanodendrites, where the Pd nanodendrites are stable in the growth solution (zeta potential > 30 mV)<sup>123</sup> and have the narrowest size distribution and highest yield, as shown in Figure 6.1.

Additional structural studies of the Pd nanodendrites were performed and shown in Figure 6.2. In Figure 6.2 (a), a TEM image of the Pd nanodendrites ( $\alpha_{\text{CTAB}} = 0.8$ ) at low magnification is displayed to illustrate the narrow size distribution of these Pd nanodendrites. The selected area electron diffraction pattern (SAED) in Figure 6.2 (b), taken from the whole region in Figure 6.2 (a) reveals the diffraction rings from the polycrystalline Pd structure and further verifies the nanodendrites are only composed of metallic Pd crystals. In order to observe the lattice structure of the nanodendrites clearly, high-resolution TEM was performed on a small seedless nanodendrite (diameter 22.7 nm), shown in Figure 6.2 (c) and its corresponding fast Fourier transform (FFT) is displayed in Figure 6.2 (d). Even though this nanodendrite consists of multiple dendritic crystals, the FFT pattern shows a Pd single crystal characterization. It indicates that the crystal lattices of these dendrites in this nanodendrite are following the same order.

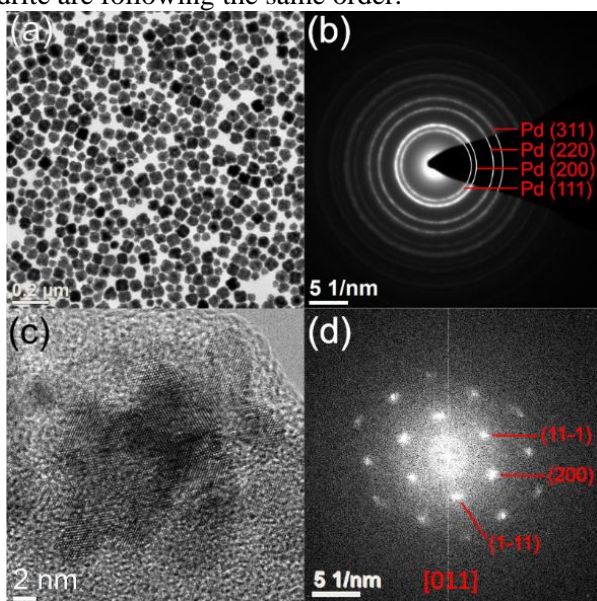


**Figure 6.2.** (a) A TEM image of Pd nanodendrites at low magnification ( $\alpha_{\text{CTAB}} = 0.8$ ); (b) A SAED of Pd nanodendrites; (c) A high-resolution TEM image of an individual nanodendrite; (d) The corresponding FFT image of the particle in (c). (Reproduced with the permission from Wen, X.; Lerch, S.; Wang, Z.; Aboudiab, B.; Tehrani-Bagha, A. R.; Olsson, E.; Moth-Poulsen, K., Synthesis of Palladium Nanodendrites Using a Mixture of Cationic and Anionic Surfactants. *Langmuir* 2020, 36 (7), 1745-1753. Copyright 2020, American Chemical Society.)

In order to study the formation mechanism of nanodendrites on Pd seeds, the growth solution ( $\alpha_{\text{CTAB}} = 0.8$ ) was monitored using the TEM at various time intervals throughout the entire synthesis process (14 hours). TEM images can present the changes related to size and structures of Pd nanodendrites throughout the growth process and the results are shown in Figure 6.3. When the growth was just started, small Pd crystals rapidly grew on the surface of Pd seeds, as shown in Figure 6.3 (0

h), and the average size ( $30.8 \pm 4.9$  nm) is around the same as the seeds previously observed, Figure 6.1 (seeds). After 1 hour, the nanodendrites grew significantly and the size reached to its maximum ( $50.6 \pm 4.8$  nm) in Figure 6.3 (1 h). Over the next several hours, the shape and size of the Pd nanodendrites stabilized without considerable changes. Only the size distribution narrows, seen from Figure 6.3 (2 h) to (14 h).

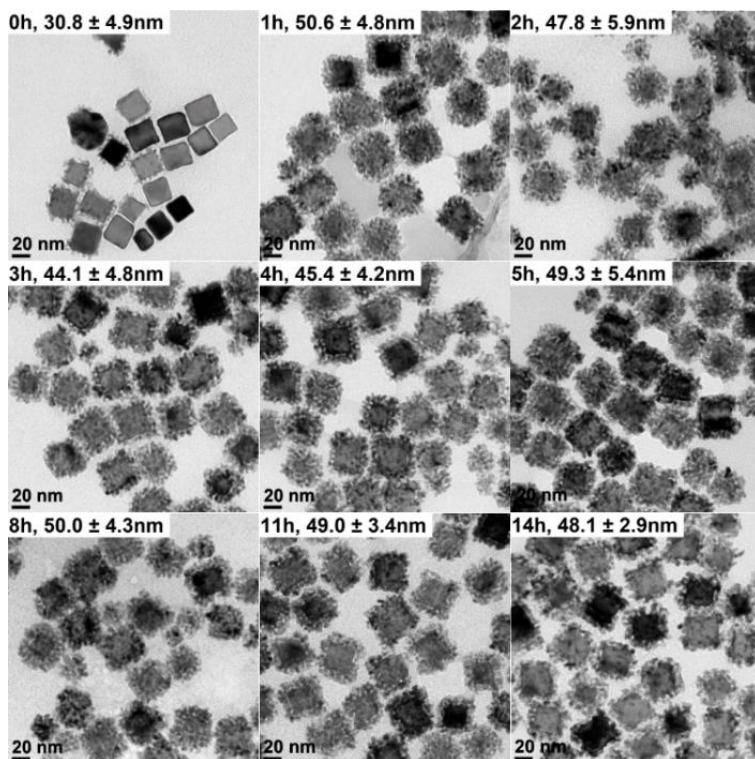


**Figure 6.3.** TEM images of Pd nanodendrites with  $\alpha_{\text{CTAB}} = 0.8$  tracked through the growth process, indicated by hours (h). The growth time and the average size of Pd nanodendrites are recorded on the top left of the images. (Reproduced with the permission from Wen, X.; Lerch, S.; Wang, Z.; Aboudiab, B.; Tehrani-Bagha, A. R.; Olsson, E.; Moth-Poulsen, K., Synthesis of Palladium Nanodendrites Using a Mixture of Cationic and Anionic Surfactants. *Langmuir* 2020, 36 (7), 1745-1753. Copyright 2020, American Chemical Society.)

It is evident that the CTAB-NaOL surfactant mixture plays a significant role in the processes of  $\text{Pd}^{2+}$  reduction and the shape-controlled growth. Hence, surfactant mixtures with various  $\alpha_{\text{CTAB}}$  were investigated with UV-Vis spectroscopy to determine if significant changes within the surfactant mixtures would occur that may influence the formation of nanodendritic shapes. Figure 6.4 displays the absorbance spectra and a photograph of the mixed surfactant solutions. The results verify that, in the surfactant solutions with  $\alpha_{\text{CTAB}} = 0.2$  to  $0.6$ , a phase separation occurred. Generally, a mixture of cationic and anionic surfactants presents instability, precipitation or formation of lamellar liquid crystals or vesicles when the

proportion of two surfactants is close to 1:1<sup>124</sup>. The phase separation results in a reduction of both surfactant concentrations in the solution, which could decrease the efficiency in stabilizing the Pd nanoparticle growth.

Ion-pairing and neutralization of surfactants with opposite charges can occur in the solution as well. Consequently, some of the molecules could precipitate from the solution, especially when the surfactants have a Krafft temperature ( $T_K$ ) above room temperature. The solubility of an ionic surfactant increases rapidly above its  $T_K$ . At temperatures lower than  $T_K$ , the surfactant tends to precipitate from the solution (i.e., the free energy of the precipitation state is higher than that of the micellar solution)<sup>125</sup>. Therefore, surfactants should be employed at or above their  $T_K$  in practice. CTAB and NaOL have  $T_K$  values at 24.5 °C and 20 °C respectively, approximately equal to room temperature (Table 6.2)<sup>126-128</sup>. Therefore, Pd nanoparticles were synthesized in the CTAB-NaOL micellar solution at 40 °C.

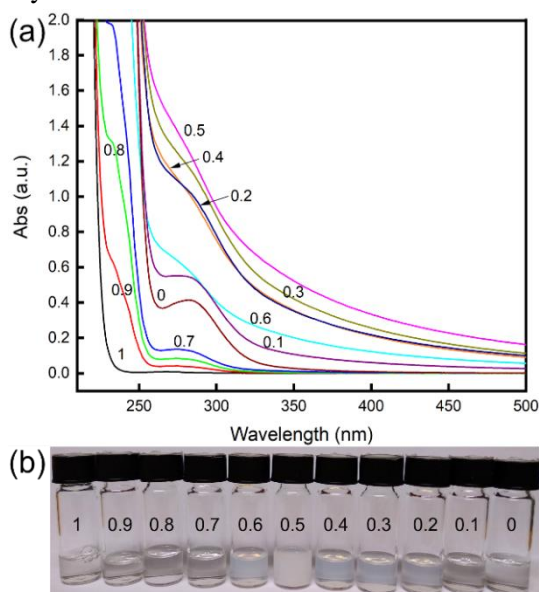


**Figure 6.4.** (a) Absorbance spectra of CTAB-NaOL surfactant solutions with various  $\alpha_{CTAB}$ . Water was used as the base line for each sample; (b) The photo of the CTAB-NaOL mixed solutions at different  $\alpha_{CTAB}$  at room temperature. (Reproduced with the permission from Wen, X.; Lerch, S.; Wang, Z.; Aboudiab, B.; Tehrani-Bagha, A. R.; Olsson, E.; Moth-Poulsen, K., Synthesis of Palladium Nanodendrites Using a Mixture of Cationic and Anionic Surfactants. *Langmuir* 2020, 36 (7), 1745-1753. Copyright 2020, American Chemical Society.)

It is worth noting that the addition of oppositely charged surfactants or inorganic salts to the micellar solution can increase the  $T_K$  of the mixture.  $T_K$  of a mixture of a cationic and an anionic surfactant is usually higher than that of the individual surfactants and the surfactant mixtures will have a higher tendency to precipitate from the solution at temperatures lower than their  $T_K$ . Additionally, the value of

hydrophilic-lipophilic balance (HLB), as an indicator of the CTAB-NaOL micellar composition, presents a minimum at  $\alpha_{\text{CTAB}} = 0.5$ <sup>129</sup>. This illustrates that two surfactants with opposite charges are strongly attracted to each other in the solution and their aggregation behavior is strongly synergistic and non-ideal.

**Table 6.2.** CMCs,  $T_K$  and HLB values of CTAB, NaOL and NaST. (Reproduced with the permission from Wen, X.; Lerch, S.; Wang, Z.; Aboudiab, B.; Tehrani-Bagha, A. R.; Olsson, E.; Moth-Poulsen, K., Synthesis of Palladium Nanodendrites Using a Mixture of Cationic and Anionic Surfactants. *Langmuir* 2020, 36 (7), 1745-1753. Copyright 2020, American Chemical Society.)

	CMC	$T_K$	HLB
CTAB	0.9 mM (25 °C) <sup>130-131</sup>	24.5 °C <sup>126</sup>	21.4 <sup>131</sup>
NaOL	0.4 mM (25 °C) <sup>130-131</sup>	20 °C <sup>127</sup>	18 <sup>132</sup>
	2.15 mM (30 °C) <sup>133</sup>		
NaST	1.8 mM (30 °C) <sup>133</sup>	79 °C <sup>127</sup>	18 <sup>134</sup>

The studies of the Pd nanodendrites synthesized with a variety of surfactant solutions point to the formation of the nanodendrites being related to the adsorption of both CTAB and NaOL molecules on the surface of the Pd seeds. The CPPs, aggregation number of surfactants in micelles and surface tension are among the most critical parameters that affect the growth of nanoparticles. As shown in Table 6.2, the CMCs of CTAB and NaOL at 25 °C are 0.9 mM and 0.4 mM, respectively<sup>129-130</sup>. However, the CMC values of CTAB-NaOL mixtures are lower than the CMCs of the individual surfactants. The lowest CMC (0.2 mM at 25 °C) appears for CTAB-NaOL mixture with the molar ratio 1:1<sup>129-130</sup>. The concentration of individual surfactants used in our synthesis (50 mM) is almost 50 times higher than the CMC values of any of the individual or mixed surfactants. As a result, the CTAB and NaOL molecules form micelles in the growth solutions and adsorb on the surface of Pd seeds. Moreover, the surface tensions of all growth solutions with various  $\alpha_{\text{CTAB}}$  remain relatively constant<sup>129-130</sup>. It is reported that the pure Pd seed surface is negatively charged and hydrophilic<sup>125, 135-136</sup>. When there was only CTAB in the growth solution ( $\alpha_{\text{CTAB}} = 1$ ), a continuous double layer of CTAB molecules were formed on the Pd seed surface<sup>135-136</sup>. However, based on the surface chemistry theory of surfactant adsorption at a hydrophilic surface, the addition of NaOL broke the continuous CTAB double layer through the electrostatic interaction between these two surfactants, forming mixed micelles on the surface of Pd seeds instead, which resulted in a decrease of the interaction strength between the surfactants and the seed surface<sup>88</sup>. The structures of the mixed micelles are affected by the CPP values of CTAB and NaOL molecules. Additionally, Pd precursors prefer to exist as  $\text{PdCl}_4^{2-}$ , a negatively charged complex ion<sup>137</sup>. Therefore, Pd precursors are attracted to the surface of Pd seeds stabilized with cationic CTAB, but repulsed by anionic NaOL molecules. In other words, CTAB assists the Pd precursor ions to move close to the seed and after reduction deposit on the seed surface but NaOL does not favor this, leading to the initial formation of small Pd crystals in the

solution, which can only deposit on the region of seed surface where the surfactant layer attracts to these crystals.

Based on the above discussion, we propose a model for the growth of Pd nanodendrites: with the addition of NaOL molecules in the growth solutions, Pd precursors were first reduced to form tiny Pd crystals in the mixed CTAB-NaOL micelles and then the tiny Pd crystals were adsorbed on the seed surface through the interaction between the surfactants and surfaces. Due to the negative charged associated with both the seed surfaces and Pd precursors, anionic NaOL molecules have much weaker interactions with the Pd seed surface than the cationic CTAB molecules, resulting in the deposition of these small Pd crystals on the Pd seed surface with CTAB molecules. Therefore, as the concentration of NaOL was increased, the interactions between the mixed CTAB-NaOL micelles and the Pd seed surface reduced. When the concentration of NaOL increased above a critical value ( $\alpha_{\text{CTAB}} \leq 0.4$ ), these small Pd crystals were not able to adsorb on the Pd seed surfaces. This model was correlated well to the TEM observation in Figure 6.1 and zeta potential values in Table 6.1. The dendrites of individual particles at  $\alpha_{\text{CTAB}} \geq 0.5$  were tiny and presented crystalline-particle shapes. However, Pd seeds added in the growth solutions with  $\alpha_{\text{CTAB}} \leq 0.4$  did not grow further. Moreover, the zeta potential became negative at the critical value ( $\alpha_{\text{CTAB}} = 0.4$ ).

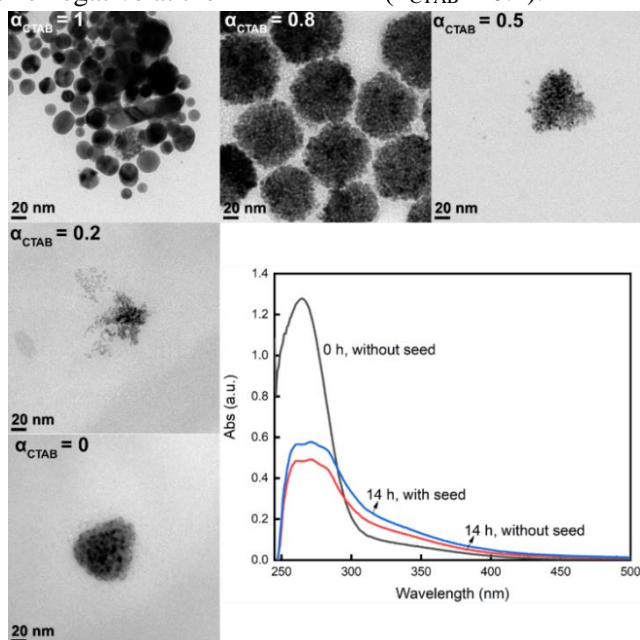


**Figure 6.5.** TEM images of Pd nanoparticles synthesized in the growth solutions without Pd seeds.  $\alpha_{\text{CTAB}}$  for each synthesis is marked on the top left of the images. Absorbance spectra for the growth solutions at  $\alpha_{\text{CTAB}} = 0$ . (Reproduced with the permission from Wen, X.; Lerch, S.; Wang, Z.; Aboudiab, B.; Tehrani-Bagha, A. R.; Olsson, E.; Moth-Poulsen, K., Synthesis of Palladium Nanodendrites Using a Mixture of Cationic and Anionic Surfactants. *Langmuir* 2020, 36 (7), 1745-1753. Copyright 2020, American Chemical Society.)

In order to demonstrate the accuracy of this model, the Pd nanoparticles were grown without the addition of the seed solution. After growth, the final solutions were centrifuged at 12000 rpm (9700 RCF) for 40 minutes to ensure all sizes of Pd nanoparticles were precipitated. Figure 6.5 features the TEM images of the nanoparticles that grew in four seedless growth solutions at various  $\alpha_{\text{CTAB}}$ . When  $\alpha_{\text{CTAB}}$  was equal to 1, Pd nanoparticles formed irregular shapes instead of the cubic shape. This is probably because instead of a continuous double layer, CTAB micelles were formed in the solution without the Pd seeds as cubic solid templates. It is worth noting that in the same synthesis process with the Pd seeds, there was also a small portion of nanoparticles with irregular shapes as well, but they were washed away by centrifugation. With  $\alpha_{\text{CTAB}} = 0.8$ , the optimal ratio, high-yield Pd nanodendrites were still formed in the seedless growth solution. However, when  $\alpha_{\text{CTAB}}$  was equal to 0.5, 0.2 and 0, more smaller crystals and fewer crystal aggregations were discovered. These results illustrate that  $\text{Pd}^{2+}$  ions in these seedless growth solutions were successfully reduced into  $\text{Pd}^0$  atoms and then formed tiny Pd crystals. These tiny crystals aggregated together to form nanodendrites at  $\alpha_{\text{CTAB}} = 0.8$ , but they were not favored to aggregate at  $\alpha_{\text{CTAB}} = 0.5, 0.2$  and 0. Moreover, the absorbance spectra of the growth solutions at  $\alpha_{\text{CTAB}} = 0$ , seen in Figure 6.5, confirmed this result as well. By comparing the black and red spectra, we discover that the intensity of the peak at  $\lambda = 265$  nm from  $\text{H}_2\text{PdCl}_4$  precursor reduced drastically from 0 hours to 14 hours in the seedless growth solution. At the same time, a broad peak at  $\lambda = 272$  nm, from  $\text{Pd}^0$ , was formed gradually, which is at the same wavelength as the peak in the growth solution with seeds after 14-hour growth. Based on these results, we evaluate that the  $\text{Pd}^{2+}$  ions were reduced by AA and formed tiny Pd crystals in the both growth solutions with and without Pd seeds. Therefore, the suggested model is supported by the experimental results in Figure 6.5.

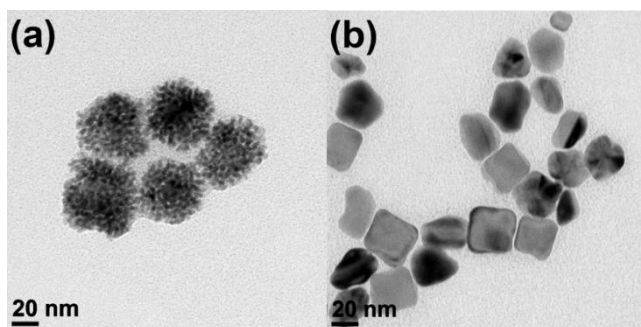


**Figure 6.6.** TEM images: (a) Pd nanodendrites synthesized by CTAC and NaOL; (b) Pd nanoparticles synthesized by CTAB and NaST. (Reproduced with the permission from Wen, X.; Lerch, S.; Wang, Z.; Aboudiab, B.; Tehrani-Bagha, A. R.; Olsson, E.; Moth-Poulsen, K., Synthesis of Palladium Nanodendrites Using a Mixture of Cationic and Anionic Surfactants. *Langmuir* 2020, 36 (7), 1745-1753. Copyright 2020, American Chemical Society.)

The above results and discussion demonstrate that Pd nanodendrites can be formed at  $\alpha_{\text{CTAB}}$  between 0.5 and 0.9. In order to test the importance of both surfactants in

the solutions further, surfactant-replaced experiments were set for the synthesis of Pd nanodendrite at an effective molar ratio ( $\alpha_{\text{CTAB}} = 0.8$ ).

The initial idea is to replace either CTAB or NaOL with another similarly structured surfactant. Since the  $\text{Br}^-$  ions relate to the formation of the facets with  $\{100\}$  indices<sup>138</sup>, it is possible to vary the dendritic shape through the replacement of  $\text{Br}^-$  with  $\text{Cl}^-$  ions. Additionally, the C-C double bonds in the hydrocarbon tails of NaOL influences their physical properties, so the substitution of the double bond may also potentially alter the dendritic shape. In our first experiment, CTAC was employed instead of CTAB in the growth solution. Fine Pd nanodendrites were successfully synthesized using this synthetic procedure, as shown in Figure 6.6 (a). These Pd nanodendrites appear to be a similar dendritic structure and have a comparable size ( $65.2 \pm 6.1$  nm) to the CTAB-NaOL stabilized Pd nanodendrites at the same molar ratio ( $\alpha_{\text{CTAB}} = 0.8$  in Figure 6.1). This illustrates that the dendritic shape of Pd nanoparticles was not changed as  $\text{Br}^-$  ions were substituted by  $\text{Cl}^-$  ions and CTAC played the same role as the CTAB. Therefore,  $\text{CTA}^+$  is a crucial segment in the formation of dendritic shapes. In the second experiment, NaOL molecules were substituted by NaST molecules, which have similar structures to NaOL molecules but lack the double bonds in the hydrocarbon tails. Figure 6.6 (b) shows that the dendritic shape was not achieved when using NaST. Even though the double bond is the only difference between the chemical structures of NaST and NaOL, the absence of a double bond increases the  $T_K$  values of NaST (79 °C in Table 6.2). As a result, NaST has a lower solubility at the reaction temperature (40 °C) in the growth solution. However, the nearly insoluble NaST molecules still interrupts the formation of Pd nanocubes. This indicates that the double bond in the hydrocarbon tail of NaOL affects the formation of nanodendrites.

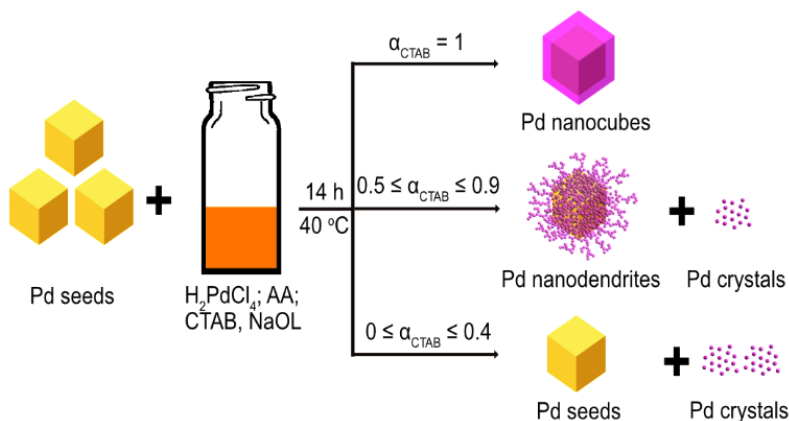


**Figure 6.7.** Schematic of the change of the Pd nanoparticle shapes with different  $\alpha_{\text{CTAB}}$  values. (Reproduced with the permission from Wen, X.; Lerch, S.; Wang, Z.; Aboudiab, B.; Tehrani-Bagha, A. R.; Olsson, E.; Moth-Poulsen, K., Synthesis of Palladium Nanodendrites Using a Mixture of Cationic and Anionic Surfactants. *Langmuir* 2020, 36 (7), 1745-1753. Copyright 2020, American Chemical Society.)

In conclusion, the studies of a two-surfactant synthesis method reveals that the shape of Pd nanoparticles is determined by the surfactant composition, as shown in Figure 6.7. When  $\alpha_{\text{CTAB}}$  equals to 1, Pd nanocubes form from Pd cubic seeds; when  $\alpha_{\text{CTAB}}$  is between 0.5 to 0.9, tiny Pd crystals aggregate to form nanodendrites and a little amount of tiny crystals remains; when  $\alpha_{\text{CTAB}}$  is lower than 0.4, tiny Pd crystals are fabricated in the solution and Pd seeds are not favored to grow larger. Additionally,  $\text{CTA}^+$  and hydrocarbon tails of NaOL with double bonds play crucial roles in the growth of the dendritic shape. Our proposed model for the formation of Pd nanodendrites is supported by the experimental results. The addition of NaOL molecules disrupts the continuous CTAB double layer and results in the formation of mixed CTAB-NaOL micelles on the Pd seed surfaces through the electrostatic interaction. First  $\text{Pd}^{2+}$  ions are reduced and form tiny crystals in the mixed CTAB-NaOL micelles and then the crystals are adsorbed on seed surfaces, which is determined by the interaction strength between the surfactants and the seed surfaces. This interaction decreases with the increase of the NaOL concentration. When  $\alpha_{\text{CTAB}}$  is lower than the critical value 0.4, the interaction is too weak to promote Pd crystal aggregation, resulting in no further growth of the Pd seeds.



## Chapter 7 Effects of Seeds and Precursors on the Growth of Pd Nanoparticles

In this chapter, the effects of seeds and metal precursors were investigated. Hollow Pd nanoparticles are achieved through the use of Ag nanocubes as seeds, rather than Pd nanocubes, resulting in Pd nanoparticles which are advantageous for potential catalytic applications because of the large, accessible surface area. Two different precursors,  $\text{H}_2\text{PdCl}_4$  and  $\text{Pd}(\text{acac})_2$ , were added in same growth processes, but led to the formation of hollow Pd nanodendrites and nanoboxes, respectively. The microstructure and elemental distribution of these two Pd nanostructures are studied in this chapter.

The growth solution for hollow nanodendrites used a mixture of CTAC and NaOL with  $\alpha_{\text{CTAC}} = 0.8$  as the capping agents, AA as a reducing agent and  $\text{H}_2\text{PdCl}_4$  as a Pd precursor. As shown from the experimental results in Chapter 6, this growth solution results in the formation of Pd nanodendrites. Cubic Ag seeds, used as hard templates, were consumed by the Pd precursor ions in a galvanic replacement reaction<sup>58</sup>. In order to understand the influence of the Pd precursors on the shape of final Pd nanoparticles, various Pd salts, including palladium(II) acetate,  $\text{Na}_2\text{PdCl}_4$  and  $\text{Pd}(\text{acac})_2$  were used to replace  $\text{H}_2\text{PdCl}_4$  in the growth solution. Only the solution with  $\text{Pd}(\text{acac})_2$  produced high-yield and uniform Pd nanoparticles in a new shape, nanoboxes.

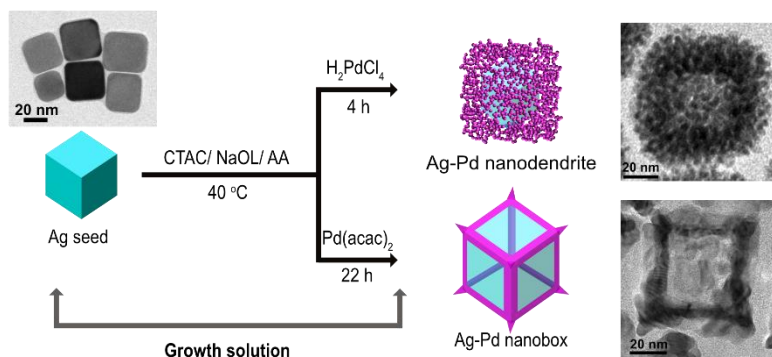


**Figure 7.1.** Schematic of the growth processes of hollow Pd nanodendrites and nanoboxes.

A schematic of the synthesis processes of hollow Pd nanodendrites and nanoboxes from Ag seeds and their TEM images are shown in Figure 7.1. The types, concentrations and volumes of reagents in both growth solutions are the same excepting the Pd precursors:  $\text{H}_2\text{PdCl}_4$  for nanodendrites and  $\text{Pd}(\text{acac})_2$  for nanoboxes. However, the incubation time of the nanoboxes (22 hours) is much longer than the nanodendrites (4 hours), because the low solubility of  $\text{Pd}(\text{acac})_2$  in water hinders its diffusion and reduction rates. The TEM images show the cubic shape of Ag seeds, as well as the dendritic and box-like shapes of the final Pd

nanoparticles. By comparing the contrast in the images, which results from the differing electron densities dependent on the amount of Pd metal present in any given area, the empty cores of both hollow Pd nanodendrite and nanoboxes can be observed. Additionally, the nanoboxes feature additional growth on the corners, forming a spiky-box shape.

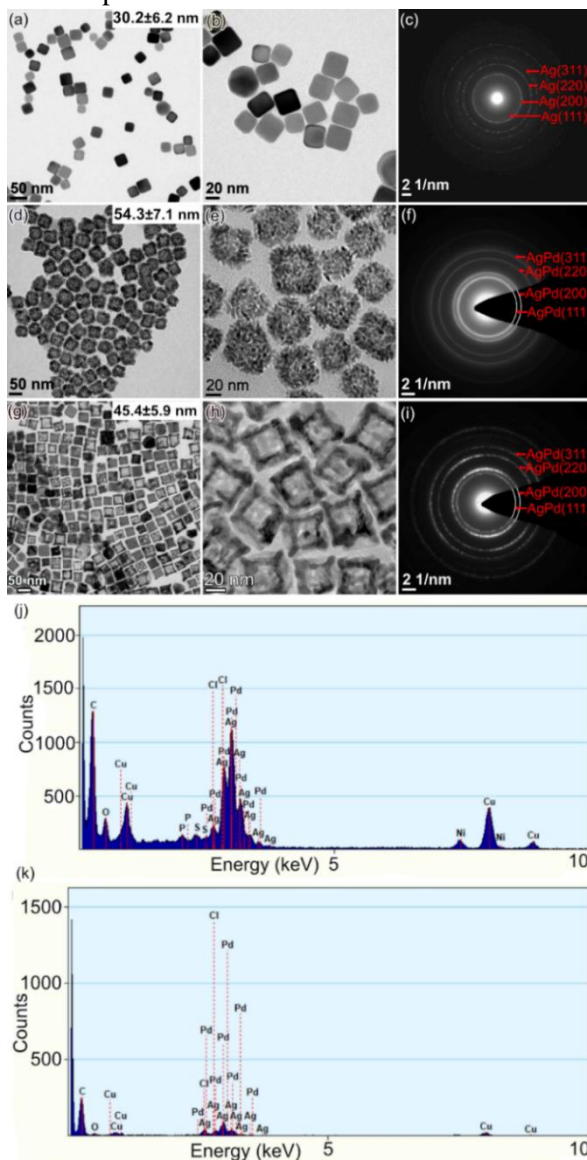


**Figure 7.2.** For Ag seeds: (a) A low magnification TEM image. (b) A high magnification TEM image. (c) SAED. For hollow Ag-Pd nanodendrites: (d) A low magnification TEM image. (e) A high magnification TEM image. (f) SAED. For hollow Ag-Pd nanoboxes: (g) A low magnification TEM image. (h) A high magnification TEM image. (i) SAED. EDS spectrum (j) Hollow Ag-Pd nanodendrites and (k) Hollow Ag-Pd nanoboxes.

Figure 7.2 displays the low and high magnification TEM images and SAED patterns of the Ag seeds, hollow Pd nanodendrites and Pd nanoboxes for a better understanding of these particles. The average size of Ag seeds is around 30.2 nm and both Pd nanodendrites and nanoboxes have grown to 54.3 nm and 45.4 nm, respectively. The SAED of Ag seeds (Figure 7.2 (c)) conforms to the diffraction pattern of face centered cubic (FCC) Ag crystals<sup>139</sup>. The SAEDs in Figures 7.2 (f) and (i) also present classical FCC characterizations, but the interplanar crystal spacings measured from the diffraction rings slightly differ with those of pure Pd crystals, which makes us suspect that a portion of Ag atoms are mixed into the Pd crystals forming Ag-Pd alloys. In order to test this suspicion, EDS spectra were taken from both the hollow Pd nanodendrites and the nanoboxes, as shown in Figure 7.2 (j) and (k). Pd and Ag peaks were detected in both samples, indicating there are Ag atoms in these hollow Pd nanoparticles. By detecting on four areas of each sample, we obtained the average composition by atomic percentage, 43% Pd and 57% Ag for nanodendrites, and 41% Pd and 59% Ag for nanoboxes.

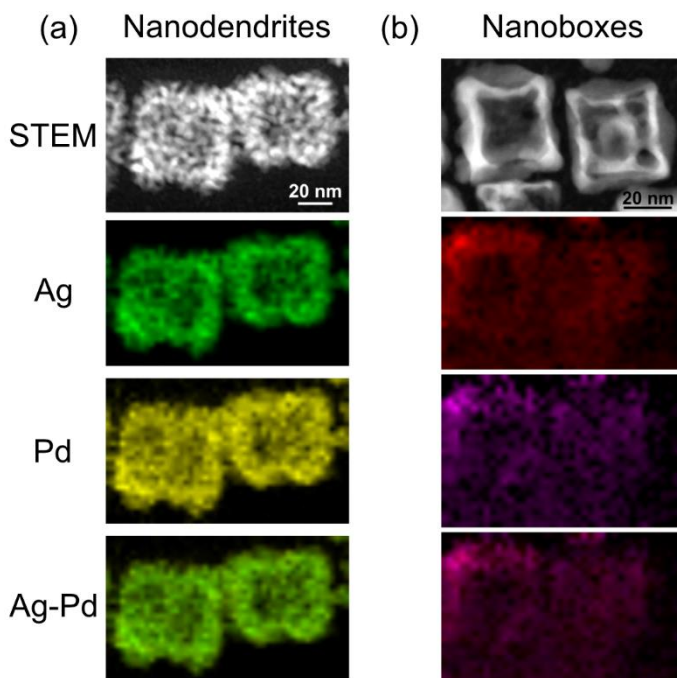


**Figure 7.3.** EDS mappings of Ag and Pd elements for (a) hollow Ag-Pd nanodendrites, (b) hollow Ag-Pd nanoboxes.

Even though the EDS spectra verifies the existence of Ag atoms in hollow Pd nanoparticles, it is still unclear if Ag and Pd form alloys or core-shell structures. Therefore, EDS maps were obtained for both hollow Ag-Pd nanodendrites and Ag-Pd nanoboxes and displayed in Figure 7.3. It is obvious that both Ag and Pd atoms are distributed over the entire particle for both nanodendrites and nanoboxes.

Especially in the figures combining the mappings of Ag and Pd, the two elements appear to mix evenly, which indicates that Ag and Pd form alloys rather than core-shell structures. Additionally, the intensity of color in the mapping represents the intensity of the elemental signals. From the contrast, it can be seen that the signals at the center of Ag-Pd nanodendrites and nanoboxes are weaker than the edges, which is further evidence of the formation of hollow structures.

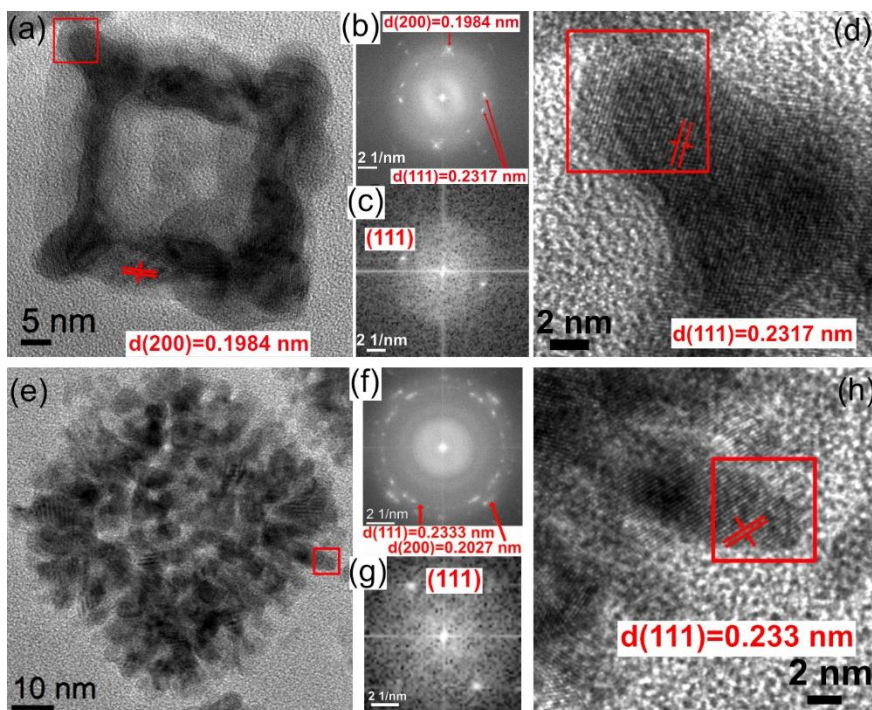


**Figure 7.4.** (a) High-resolution TEM image of an entire hollow Ag-Pd nanobox and (b) the corresponding FFT image. (c) The corresponding FFT image of (d) the magnified high-resolution TEM image of the corner of the nanobox marked by a red square in (a). (e) High-resolution TEM image of an entire hollow Ag-Pd nanodendrite and (f) the corresponding FFT image. (g) The corresponding FFT image of (h) the magnified high-resolution TEM image of the dendrite of the nanodendrite marked by a red square in (e). High-resolution TEM images were taken by Robson Rosa da Silva.

Further, the microstructure of hollow Ag-Pd nanoboxes and nanodendrites was studied in detail by high-resolution TEM. Figures 7.4 (a) and (b) show the high-resolution image of an entire nanobox and its corresponding FFT image. The FFT presents an ordered polycrystal characterization, in which the spots from (200) lattice planes have strong intensities, indicating the nanobox grew following (200) lattices planes, marked by a red line in Figure 7.4 (a). Additionally, the nanobox also has an order along (111) lattice planes. The high-resolution image and the corresponding FFT of the nanobox corner illustrate that this spiky tip just grew along (111) lattice plane, the close-packed plane of FCC structure. Growth along

this direction is known to achieve a stable structure with the lowest energy<sup>140-141</sup>. Moreover, the interplanar crystal spacings of (111) and (200) were measured in Figure 7.4 (b), where,  $d_{(111)} = 0.2317$  nm and  $d_{(200)} = 0.1984$  nm. Based on these values and the rules of FCC structure, we deduce that the crystal structure of the hollow Ag-Pd alloy nanoboxes has a lattice constant 0.3991 nm, which falls between Pd (0.3890 nm) and Ag (0.4086 nm), as expected<sup>142</sup>.

The same analysis was performed on hollow Ag-Pd nanodendrites. Compared to nanoboxes, the FFT of the nanodendrite (Figure 7.4 (f)) presents ring patterns, indicating that these small dendrites grew in all directions in low orders. Nevertheless, the intensity along the rings is not uniform, and the regions with high intensities on the ring of (200) lattice planes are probably caused by the template, which was the cubic Ag seed. The high-resolution TEM image and the corresponding FFT image of the small dendrite in Figures 7.4 (g) and (h) verify that it grew along the close-packed plane of FCC structure, (111) lattice planes as well. Additionally, the interplanar crystal spacings of (111) and (200) were calculated from Figure 7.4 (f), where,  $d_{(111)} = 0.2333$  nm and  $d_{(200)} = 0.2027$  nm. Through these values, we deduce that the hollow Ag-Pd alloy nanodendrites have the FCC crystal structure with the lattice constant 0.4047 nm, which also lies between the lattice constants of Pd and Ag.

In this chapter, we synthesized hollow Ag-Pd alloy nanodendrites and nanoboxes successfully by using different Pd precursors,  $H_2PdCl_4$  and  $Pd(acac)_2$ , respectively. Ag atoms remain in these particles with atomic percentages of 48% in hollow nanodendrites and of 53% in hollow nanoboxes. The lattice constants in the alloy FCC structures of the Ag-Pd nanodendrite (0.4047 nm) and the nanobox (0.3991 nm) are both between the constant values of Pd and Ag crystals. Additionally, both the spiky tips of the nanoboxes and the small dendrites of the nanodendrites grew along (111) lattice planes, the close-packed plane of FCC structure, in order to achieve a stable state with low energy. The formation of different particle shapes by using different Pd precursors was not studied in this chapter, but it may be explained by the different solubilities of the precursors. As the model proposed in Chapter 6, CTAC and NaOL molecules form mixed micelles on the Ag seed surface.  $H_2PdCl_4$  precursor tends to exist as negatively charged  $PdCl_4^{2-}$  in the solution, which is attracted by the positively charged CTAC molecules in the mixed micelles on the surface of Ag seeds and then reduced in the center of the micelles, resulting in the formation of small dendritic clusters. However, compared to  $H_2PdCl_4$ , insoluble  $Pd(acac)_2$  has much weak electrostatic interaction with charged surfactants, leading to free locating of  $Pd(acac)_2$  precursor over the entire seed surface. This results in homogeneous growth of the reduced Pd atoms, forming nanoboxes. Additionally, the reduction rate of  $Pd(acac)_2$  is also restricted due to the insolubility, which extends the growth time of Ag-Pd nanoboxes.



## Chapter 8 Effects of pH on the Growth of Pd Nanoparticles

In this chapter, the effects of pH on the growth of metal nanoparticles were investigated. Nowadays, many studies show that polyvinylpyrrolidone (PVP)-stabilized Pd nanoparticles demonstrate excellent performance for catalytic applications, but the shapes of these Pd nanoparticles are usually confined to simple shapes, such as cubes, spheres and rods<sup>143-144</sup>. This inspires us to utilize a capping agent mixture of PVP and NaOL for the synthesis of dendritic Pd nanoparticles in order to increase the surface area and promote their catalytic efficiency. Since PVP is a nonionic polymer, it has a poor electronic interaction with anionic NaOL molecules. In order to strengthen the interaction between PVP and NaOL, a certain amount of HCl or NaOH solution was introduced into the PVP-NaOL mixture solutions to tune the pH environment. In this chapter, a series of experiments were performed to synthesize Pd nanoparticles at different pH values of the PVP-NaOL mixture solutions and the optimal conditions for the growth of Pd nanodendrites were discovered.

One-step seedless method was applied in the experiments, where the growth solution includes PVP, NaOL, HCl/NaOH, Pd precursors and a reducing agent, AA. The molar ratio of PVP monomers and NaOL molecules was always kept at the same value of 4:1 ( $\alpha_{\text{PVP monomer}} = 0.8$ ) for each synthesis. A series of synthetic experiments were performed at different pH values of the PVP-NaOL mixtures. The initial pH of the PVP-NaOL mixture is 9.47. We increased the pH to 11.75 and 12.36 by adding a proper amount of the NaOH solution and decreased the pH to 7.06, 3.35, 2.03, 1.17 and 0.6 by the addition a certain volume of HCl solution, as reported in Table 5.1 in Chapter 5. The TEM images and an absorbance spectrum of the obtained Pd nanoparticle are shown in Figure 8.1.

When the pH value is above 9 (Figures 8.1 (a) to (c)), tiny Pd crystals are formed with an average size 3.46 nm at pH 12.36, 5.9 nm at pH 11.75 and 6.0 nm at pH 9.47, with size distributions around 17.3% to 21.2%. This illustrates that reduction of Pd precursors occurred drastically, resulting in rapid nucleation at the beginning of the synthesis. However, the increase of pH does not enhance the aggregation of these tiny Pd crystals through the interaction with PVP and NaOL. In fact, as the pH value is reduced, this aggregation is favored and Pd nanodendrites start to form at pH 7.06, 3.35 and 2.03, shown by red arrows in Figures (d) to (f). At these three pH values, the average sizes of Pd nanoparticles increase to a range of 12.6 nm to 17.9 nm, while the size distributions also increase significantly, up to 34.4% to 37.4%, due to the large size difference between the single crystals and the aggregated nanodendrites. When the pH is at 1.17, where the molar ratio of additional  $\text{H}^+$  and PVP monomers is equal to one, most of the Pd crystals aggregated to form nanodendrites with an average size 36.1 nm with a distribution of 10.5%, the lowest

level in the all eight synthetic experiments. However, as the pH continuously decreases to 0.6, large nanoparticles with clear facets are fabricated. Figure 8.1 (i) displays the normalized spectrum of Pd nanoparticles synthesized at the pH where nanodendrites form. In the absorbance curves of pH 7.06 and 3.35, there are two peaks at the wavelengths of 247 nm and 295 nm, indicating the individual Pd crystals and nanodendrites, respectively. At pH of 2.03 and 1.17, the formation of Pd nanodendrites increases the intensity of the nanodendrite peak and decreases the intensity of the individual crystal peak. Based on these results, it is obvious that pH 1.17 is the optimal condition to synthesize Pd nanodendrites with this concentration of PVP and NaOL capping agents.

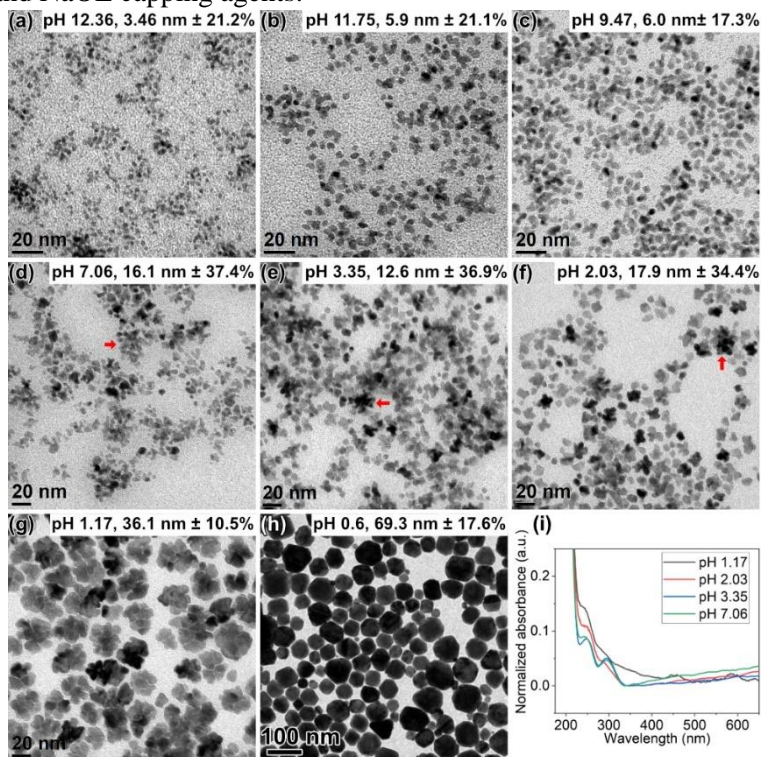


**Figure 8.1.** TEM images of Pd nanoparticles synthesized with PVP and NaOL at different pH values. The pH values and the average size of Pd nanoparticles are marked in each image of (a) to (h). (i) Normalized absorbance spectra of the Pd nanoparticle solutions at pH 7.06, 3.35, 2.03 and 1.17.

High-resolution TEM images, shown in Figure 8.2, provide lattice structure of the Pd nanodendrites in detail. Figure 8.2 (a) displays the high-resolution image of an entire Pd nanodendrites synthesized at pH 1.17 and its corresponding FFT is shown in Figure 8.2 (b). This Pd nanodendrite consists of several smaller crystals, compared to the Pd nanodendrites synthesized with CTAB and NaOL in Chapter 6, which contain a large number of much smaller crystals. Instead of polycrystalline rings, there are still clear spots observed in the FFT, some of which are from (111)

and (200) lattice planes, highlighted by the red rings marked in Figure 8.2 (b). It illustrates that this Pd nanodendrite does consist of several single crystals and even forms twin structures. A twin structure region has been marked by a red square in Figure 8.2 (a) and magnified in Figure 8.2 (c). The twin boundary has been noted by a black arrow, which follows the (1-11) lattice planes. Additionally, the (11-1) and (-1-11) lattice planes from both lattice crystals respectively are marked in the image and the different colors correspond to the colors of the signs in its FFT image in Figure 8.2 (d).

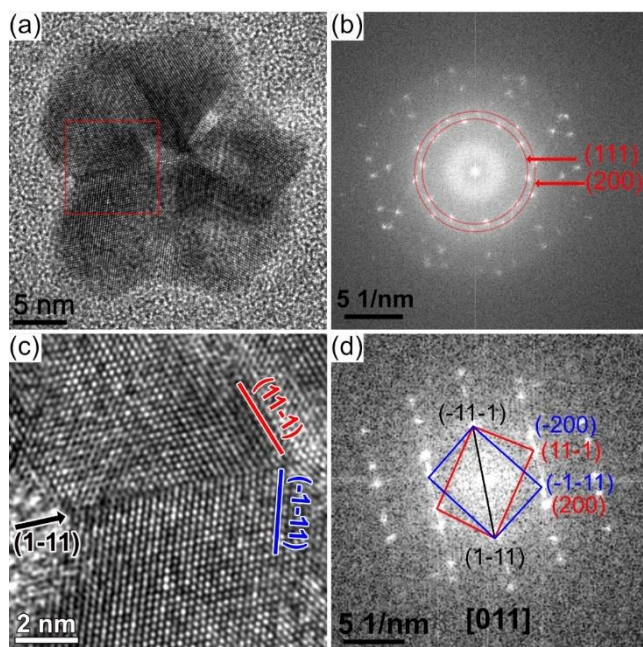
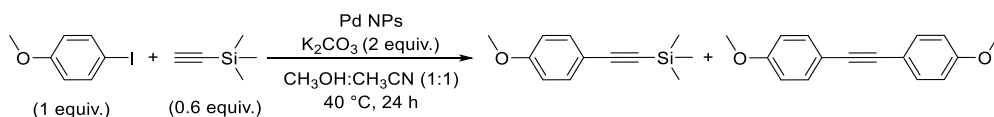


**Figure 8.2.** (a) High-resolution TEM image of an entire Pd nanodendrite. (b) The corresponding FFT of (a). (c) High-resolution TEM image of the region marked by a red square in (a). (11-1), (-1-11) and (1-11) lattice planes are recorded by red, blue and black colors, respectively. (d) The corresponding FFT of (c). The colors of lattice plan indices are consistent with the markers in (c).

The Pd nanodendrites synthesized at pH 1.17 were tested in a preliminary catalytic Sonogashira reaction between 4-Iodoanisole and trimethylsilylacetylene to evaluate the coupling product is either ((4-methoxyphenyl)ethynyl)trimethylsilane (MPE-TMS) or 1,2-bis(4-methoxyphenyl)ethyne (BMPE), as shown in Scheme 8.1.



**Scheme 8.1.** Preliminary test for Sonogashira coupling reaction between 4-Iodoanisole and trimethylsilylacetylene. The reaction was performed by Jessica Orrego Hernandez.

In this preliminary test, the final crude mixture of the reaction was analyzed by nuclear magnetic resonance (NMR) and the result is shown in Figure 8.3. Compared to the individual materials, only the peaks corresponding to the BMPE and the starting material (4-Iodoanisole) are discovered in the mixture of product, which indicates that there is a high selectivity towards the bi-coupling BMPE versus the mono-coupling product MPE-TMS in this reaction.

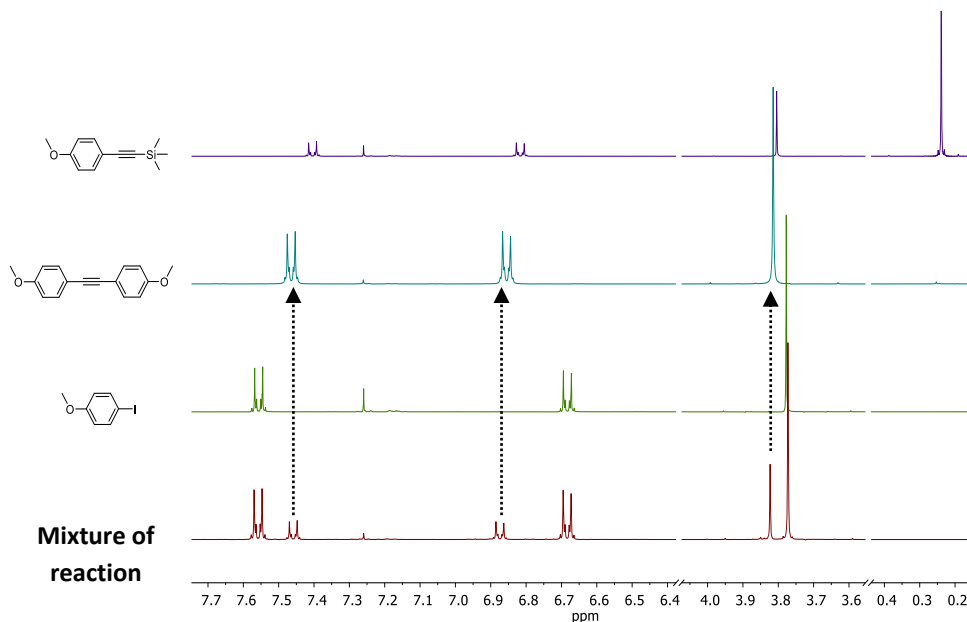


**Figure 8.3.** <sup>1</sup>H NMR spectra of the mixture of reaction compared with starting material and the products: MPE-TMS and BMPE. The measurement was taken by Jessica Orrego Hernandez.

In this chapter, we successfully synthesized Pd nanodendrites with PVP and NaOL mixtures by tuning the pH values. The optimal Pd nanodendrites with a high yield were achieved at pH 1.17. These nanodendrites consist of several single crystals and shows twin structures. Finally, these Pd nanodendrites were tested in a Sonogashira reaction between 4-Iodoanisole and trimethylsilylacetylene, which has catalytic activity towards the bi-coupling product BMPE.

## Chapter 9 Growth-Induced Strain in Au Nanorods

In this chapter, a growth-induced strain was discovered in Au nanorods and the microstructure of Au nanorods were studied in detail. High-yield single crystal Au nanorods were synthesized through the method reported by Xingchen Ye and co-authors<sup>23</sup>, where a mixture of CTAB and NaOL was utilized to improve the nanorod yield and size uniformity. A small amount of  $\text{AgNO}_3$  was added in the growth solution to promote the yield of nanorods as well<sup>39, 145</sup>. However, there is still lack of understanding about the role of the Ag in this synthesis method, especially the ultimate location of the Ag on the final nanorods. In order to clarify this question, an EDS mapping was performed in this chapter. Additionally, the facets of the rods were studied. Surprisingly, we discovered that a large portion of these Au nanorods are strained, which has a significant impact on the catalytic properties of metal nanoparticles<sup>146-147</sup>. In order to understand the detailed structure of these Au nanorods for the future applications, a series of microstructural studies were performed on TEM. The distribution of elements, crystal facets and lattice strain are reported in this chapter. Additionally, the origin of the strain is discussed as well.

Figures 9.1 (a) to (c) provide general information about the Au nanorods. Figure 9.1 (a) shows the absorbance spectrum of the Au nanorod solution with the two peaks, that are characteristic of rod-shaped nanoparticles<sup>148-149</sup>. The peak at 507 nm results from the plasmon resonance along transverse axis and the peak at 1028 nm is caused by the plasmon resonance along the longitudinal axis (discussed in Chapter 2). Since there is no obvious indication of additional peaks from particles with other shapes, this spectrum illustrates that the Au nanorods constitute a high percentage of the nanoparticles in the growth solution. In order to visualize all three dimensions of the Au nanorods, a low magnification SEM image of standing Au nanorods and a TEM image of lying-down Au nanorods are shown in Figures 9.1 (b) and (c). From both perspectives, it can be observed that size and shape of these Au nanorods are relatively uniform. Their average length, width and aspect ratio are  $119 \pm 17$  nm,  $26 \pm 4$  nm and  $4.7 \pm 0.8$ , respectively, indicating a narrow size distribution. Moreover, we notice that in the TEM image of lying-down Au nanorods, many of the nanorods have a variation in contrast within the rod. This was the first indication of the existence of lattice strain.

Before further description of the microstructure, it is important to clarify the chemical composition of the Au nanorods. As mentioned above, in addition to the Au precursors and Au seeds, another metal, Ag, in the form of  $\text{Ag}^+$  ions, was added in the growth solution to assist the formation of rod shapes. This Ag may reduce along with the Au and remain incorporated the Au nanorods. In order to determine this, an EDS map is displayed in Figure 9.1 (d), where the yellow color stands for Ag and blue represents Au. As we hypothesized, Ag is present in the lattice of the

Au nanorods. However, much to our surprise, the intensity distribution indicates that the Ag also forms an outer layer around the Au nanorods. Moreover, an averaged normalized intensity distribution of the region marked by a green square in Figure 9.1 (d) along the transverse axis of the rod (green arrow line) is shown in Figure 9.1 (e). The curve of Au has a low intensity at two edges of the nanorod but increases towards the center of the rod and achieves its highest intensity at the center. Ag is also distributed across the rod, has low intensities at two edges and achieves the highest intensity at the center of the rod. However, there is a key difference between Ag and Au. When moving from one edge to the center, the intensity of Ag increases for a while, then suddenly decreases and then increases again, forming an intensity dip. This result is consistent with the simulation result of a model where it is assumed that Ag mixes into the Au lattice in the middle of the Au nanorod and also is present in an outer layer wrapping the entire Au nanorod, as shown in Figures 9.1 (f) and (g).

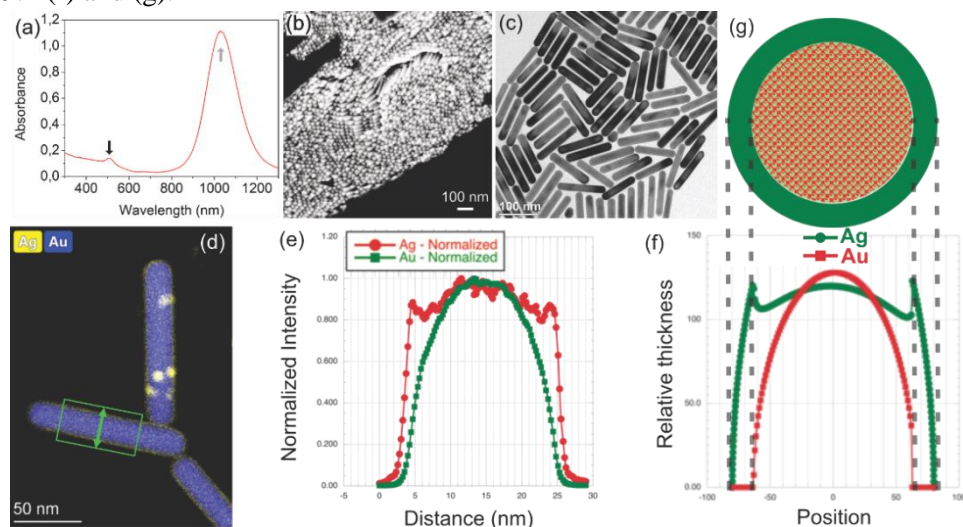


**Figure 9.1.** (a) Absorbance spectrum of the Au nanorod solution. The peak at 507 nm, pointed by a black arrow, results from the plasmon resonance along transverse axis and the peak at 1028 nm, marked by a gray arrow is caused by the plasmon resonance along the longitudinal axis. (b) Low magnification SEM image of standing Au nanorods. (c) Low magnification TEM image of lying-down Au nanorods. (d) EDS mapping of Au nanorods for Ag (yellow) and Au (blue). The Au nanorod contains around 7 wt % of Ag. (e) The corresponding intensity distribution for the region marked by a green square in (a). The distance is along the transverse axis of the Au nanorod, marked by a green arrow line. (f) Simulated intensity distribution along the nanorod transverse axis of a model where the Ag distributes in the lattice of Au and is also present in an outer layer around the Au nanorod as well. (g) Schematic of the model used for simulating the result in (f). This is a cross section of the nanorod, where green represents Ag and red represents Au. The EDS mapping and simulation were performed by Nestor Zaluzec.

In Figure 9.2, we show the lattice index of facets around the longitudinal axis of the Au nanorods. High-resolution STEM images and their corresponding diffraction

patterns were taken from [001], [011] and [013] zone axes and are shown in Figures 9.2 (a) to (c), respectively. The purpose is to obtain the intensity profiles along the transverse axis from these three zone axes. The crystallographic directions of a typical Au nanorod are shown in the schematic in Figure 9.2 (d). The three axes, [001], [011] and [013], are all perpendicular to the longitudinal axis, [100], from which the intensity profiles can give relatively complete shape information. In the intensity profiles from the [001] and [011] zone axes, Figures 9.2 (a) and (b), there is a peak at the center, while, the intensity curve from [013] is more flat at the center, as shown in Figure 9.2 (c). This result indicates that the [001] and [011] zone axes are facing towards a boundary between two adjacent surface facets of the Au nanorod, but [013] is directly facing to a surface facet.

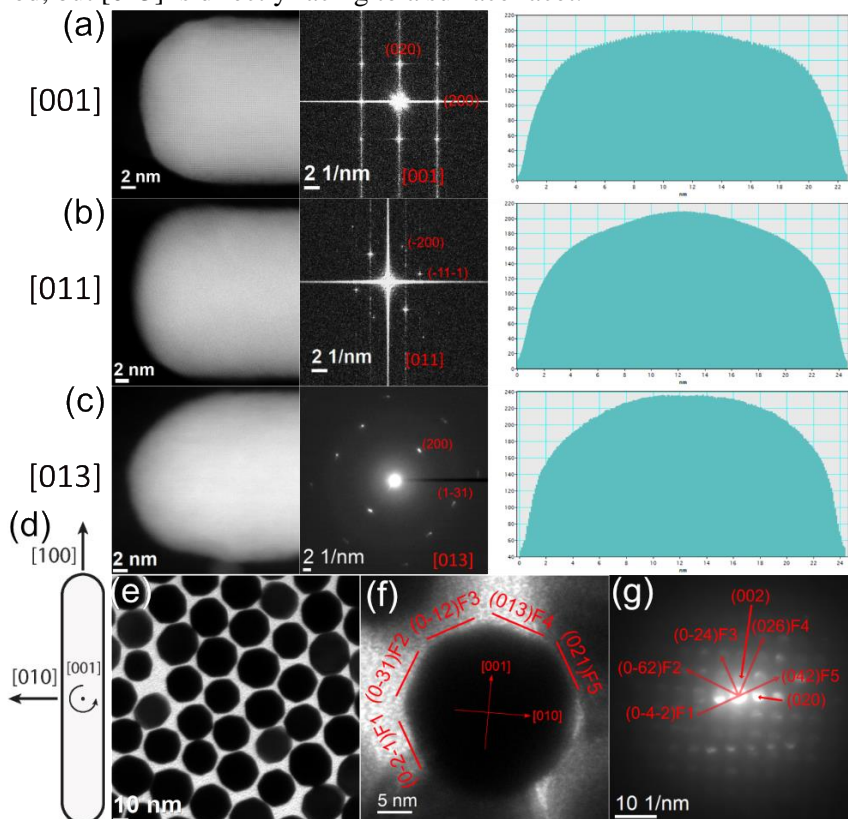


**Figure 9.2.** Annular dark field HRSTEM images, the corresponding fast Fourier transformations (FFTs) or diffraction pattern of nanorods and intensity profiles along the transverse axis of the Au nanorod displayed in sequence. (a) Electron beam is incident along [001] zone axis. (b) Electron beam is incident along [011] zone axis. (c) Electron beam is incident along [013] zone axis. (d) Schematic of the Au nanorod with crystallographic directions. (e) Low magnification bright field TEM image of standing Au nanorods. (f) Bright field TEM image of a standing Au nanorod. (g) The corresponding diffraction pattern of the Au nanorod in (f).  $F_i$  is facet number used to correlate the facet in (f) to the diffraction spot in (g).

In order to support the above conclusion, a low magnification TEM image of the standing Au nanorods was recorded. It shows a clear octagonal shape of the cross section of the Au nanorods in Figure 9.2 (e). A high magnification TEM image of a standing Au nanorod and the corresponding SAED pattern are shown in Figures 9.2 (f) and (g). The zone axis of the SAED pattern is the longitudinal axis of the Au nanorod, [100] crystal direction. The [010] and [001] crystal directions, perpendicular to (010) and (001) lattice planes are marked by red arrows in Figure 9.2 (f). By comparing the normal directions of the rod facets in Figure 9.2 (f) and the lattice orientations related to the diffraction spots in Figure 9.2 (g), we discover that the facets of the nanorods (F1 to F5) all consist of {012} and {013} families of crystal planes, which are relatively low energy lattice planes of FCC crystal structures. The left three facets do not appear to be clear facets and adjacent facet boundaries, but instead, consist of small facet segments of {012} and {013} planes.

We initially performed high-resolution STEM on an entire Au nanorod from [001] zone axis to observe the microstructure on the atomic scale, shown in Figure 9.3 (a), and discovered that the Au nanorod rod was slightly bent. The white dots throughout the Au nanorod are individual atom columns, showing the (100), perpendicular to [100,] and (010), perpendicular to [010], lattice planes in the gold FCC structure. The whole Au nanorod is single crystal and even though the bending is obvious, no defects in the crystal lattice can be identified. Therefore, it is important to study the bending trend and the strain distribution in this rod, as shown in Figures 9.3 (b) and (c). The angle between the connection of adjacent atom columns and the horizontal reference axis, called the bonding angle, was measured to quantify the bending degree through the whole rod<sup>146</sup>. The bonding angle map in Figure 9.3 (b1) shows the bonding angle distribution across the whole nanorod. In this bonding angle, the red color indicates an anticlockwise rotation and blue represents a clockwise rotation. The maximum variation in bonding angle is 5°. The bending degree is increasing gradually from the middle area. The bonding-angle diagram in Figure 9.3 (b2) displays the bending trend along the longitudinal axis. The gradient of this curve is large in the middle area. The distribution of the lattice strain along the longitudinal direction is shown in Figures 9.3 (c). The strain map of the entire Au nanorod in Figure 9.3 (c2) shows a blue color on the upper middle region and red color on the lower middle region, indicating that there is tensile strain in the upper middle region and compressive strain in the lower middle region of the Au nanorod. Moreover, in the strain map of the middle section in Figure 9.3 (c3), based on geometric phase analysis (GPA), this trend becomes even clearer. The upper area shows red color, which indicates tensile strain, while the bottom area displays green and blue color, which indicates compressive strain. However, the lattice strain map of the end region in Figure 9.3 (c4) shows an even green color (compressive strain), indicating there is no strain in this region. These results verify that a strong strain exists in the middle section of the Au nanorod and are consistent with the bonding angle results. The bending leads to a lattice strain in the Au nanorod.

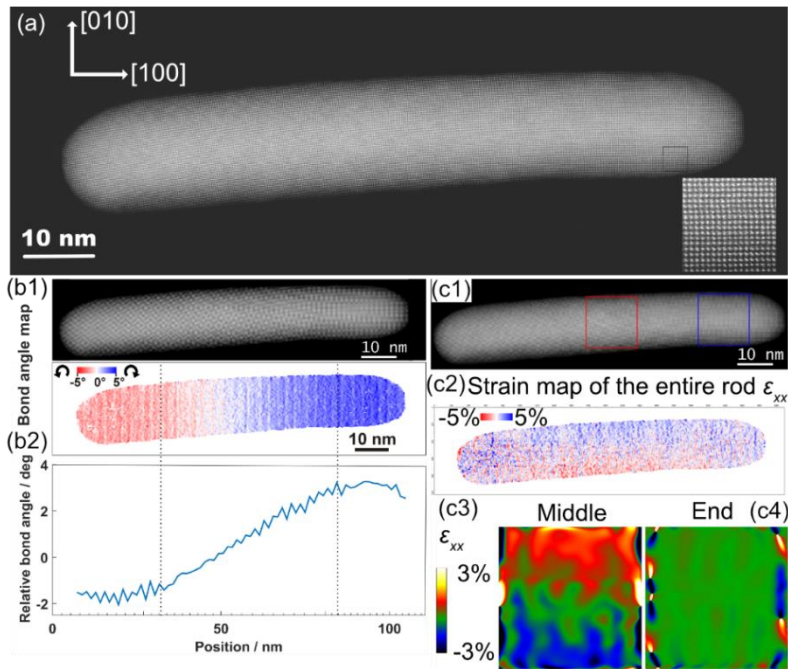


**Figure 9.3.** (a) High-resolution annular dark field STEM image of an Au nanorod. The insert is a magnified image of the region in the black square, showing the arrangement of the individual gold atom columns in a single crystal structure. (b1) Bonding angle map of the entire Au nanorod in (a), where red color stands for anticlockwise rotation and blue color represents clockwise rotation. (b2) Bonding angle distribution curve along the longitudinal axis. The angles in rod range from 3% to -2%. (c1) High-resolution STEM image corresponds to the strain map. The middle and end regions used for geometric phase analysis are marked by red and blue squares, respectively. (c2) Lattice strain map of the entire rod. (c3)  $\epsilon_{xx}$  strain distribution in the middle section of the AuNR. (c4)  $\epsilon_{xx}$  strain distribution in the end section of the AuNR.  $\epsilon_{xx}$  is the strain along longitudinal direction of the Au nanorod. The observed strain ranges from 1% to -1%. Color variation of strain maps for middle and end regions from white to black corresponds to strains from 3% (tensile strain) to -3% (compressive strain). The bonding angle and strain map based on the position of the atom columns were analyzed by Torben Nilsson Pingel, strain maps of the middle and end regions based on geometrical phase analysis were carried out by Lunjie Zeng and the high-resolution annular dark field STEM image was taken by co-authors from The University of Tokyo.

In order to study the bending angle and orientation in more detail, SAED and Kikuchi patterns were recorded. Since Kikuchi patterns are more sensitive to lattice tilting than SAED, we can measure the movement of the symmetry points of the Kikuchi patterns relative to the transmission spot of SAED to quantify the bending angle and local crystal orientation of the rod. The Au nanorod is tilted close to the [001] zone axis to assist observation and analysis. Kikuchi patterns were taken from five different regions of this Au nanorod, marked by A to E in the TEM image in Figure 9.4 (a). Additionally, the corresponding SAED pattern and the dark field image from a (-200) diffraction spot are shown in Figures 9.4 (b) and (c). The SAED

pattern shows a classical single crystal character. The symmetrical contrast caused by lattice strain can be seen clearly in the dark field image, which confirms the results from Figure 9.3. In Figures 9.4 (d) to (h), the symmetry point of the Kikuchi pattern was marked by a red cross and the center of each transmission spot was marked by a red dot as an object of reference. Following the track of the symmetry point of the Kikuchi pattern from Figures 9.4 (d) to (h), we found the symmetry point of the Kikuchi pattern is moving along a pair of Kikuchi lines, which corresponds to the (010) lattice plane. After calibration and calculation, it is concluded that the (100) lattice planes are tilted  $3.45^\circ$  around [010] crystal axis from Regions A to E. The bending of the rod happens continuously and there were no crystal defects observed. Therefore, the Kikuchi pattern results are in accordance with the high-resolution STEM observations in Figure 9.3, illustrating that there are no observable lattice defects in the rods. The Kikuchi patterns were measured for eleven more bent Au nanorods and the lattice tilting angles of these bent Au nanorods are shown in Table 9.1, illustrating the bending angle in the range less than  $10^\circ$ . The bending of all Au nanorods happened on (100) lattice planes around [010] crystal axis.

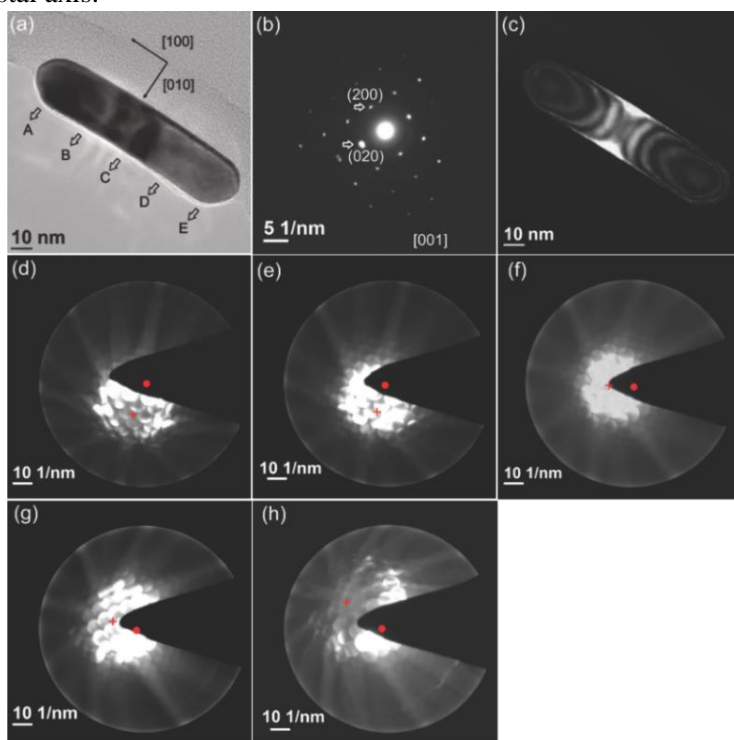


**Figure 9.4.** (a) Bright field TEM image of an Au nanorod, with arrows marking the locations of further electron diffraction analysis. (b) SAED pattern of this Au nanorod, indicating a single crystalline structure throughout the Au nanorod. (c) Dark field TEM image of this Au nanorod from (-200) diffraction spot. (d) to (h) Kikuchi patterns taken from Region A to E on the Au nanorod marked in (a).

In order to study the reason for the bending, many factors were considered. First, we investigated whether the bent edges of the lacey carbon film on the TEM grids led to a bending of the Au nanorods following the curve of the carbon film. However, further research shows that bent Au nanorods appear not only at the edge of lacey carbon film but also on the flat silica substrate in SEM. This indicates that there are other factors resulting in the strain. Second, we suspected there were lattice defects in Au crystals giving rise to the bending, but the combined high-resolution STEM result in Figure 9.3 and TEM studies verified that no obvious defects could be observed, which eliminates our second suspicion. Third, we hypothesized that if the cross section of Au nanorods was asymmetric, indicating additional asymmetry in the growth process, could result in a lattice strain. The observations on the standing Au nanorods in Figures 9.1 and 9.2 indicates that the cross section is symmetric. This eliminates structural components of the Au nanorod itself as the reason for the observed bending. Fourth, if the Ag distribution along the transverse axis was asymmetric, it could result in the strain as well. However, the EDS mapping and the corresponding intensity distribution of Ag and Au elements show that the distribution of both elements are symmetric, denying the fourth suspicion. At last, we propose one possible hypothesis for the lattice strain in the Au nanorods.

**Table 9.1.** Tilting angles of (200) lattice planes in bent Au nanorods and the size information of the Au nanorods.

Number	Tilting angle	Length of the rod (nm)	Width of the rod (nm)	Aspect ratio
1	3.45°	111	25	4.4
2	7.38°	130	23	5.7
3	2.91°	113	25	4.5
4	1.39°	118	28	4.2
5	4.04°	108	21	5.1
6	4.09°	132	23	5.7
7	1.48°	109	21	5.2
8	3.98°	125	23	5.4
9	5.18°	130	25	5.2
10	3.24°	124	24	5.2
11	2.49°	121	22	5.5
12	3.50°	114	21	5.4

As a final hypothesis, we suggest that a change in the distribution of the surfactant layer consisting of CTAB and NaOL, which surrounds the Au nanorods, may cause a bending, giving rise to strain, through an asymmetrical distribution of the surfactant molecules. The surfactant layer could be observed in the EDS map in Figure 9.5 (a). The surfactant layer can be seen clearly by the contrast and has an average thickness of around 3 nm, corresponding to the small angle scattering of

either X-rays or neutrons results from the work of Sergio et al.<sup>150</sup>. The EDS map in Figure 9.5 (a) also presents a bent AuNR. The averaged Ag intensity profile from the bent section, seen in Figure 9.5 (b), shows an asymmetry in the surface layer with the Ag and the surfactant. The layer has a double thickness at the AuNR upper side in tension and the single layer thickness at the lower side in compression.

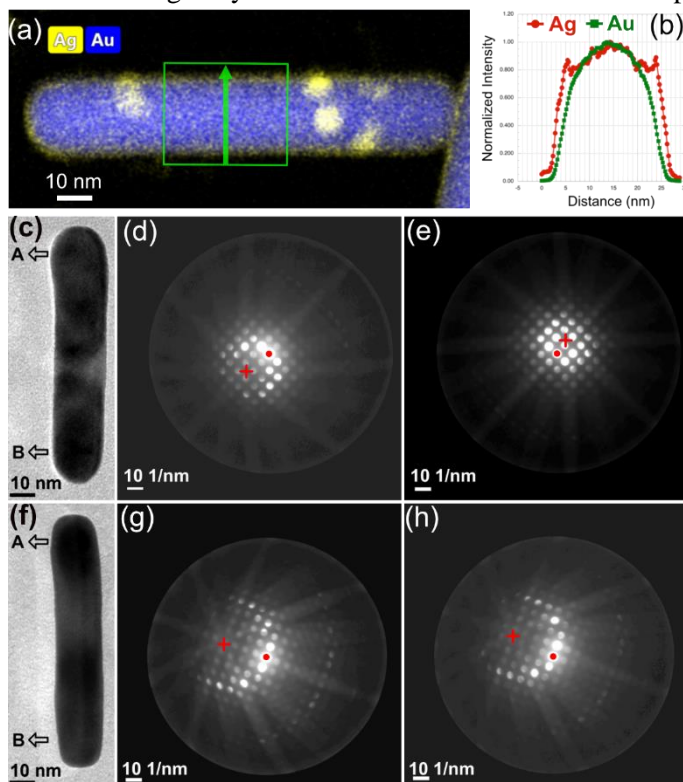


**Figure 9.5.** (a) An EDS map showing the Ag containing surfactant layer around the Au nanorod. Bright Ag dots are random Ag deposition that overlaps with the rod. (b) Averaged intensity line profiles along the transverse axis for Au (green curve) and Ag (red curve) obtained from the region marked by a green square in the EDS map in (a). (c) Au nanorod before exposure to the electron beam. (d) Kikuchi pattern from A in (c). (e) Kikuchi pattern from B in (c). (f) Au nanorod after exposure to the electron beam. Exposure condition: Dose: 36386 e/nm<sup>2</sup>s; Time: 70 minutes. (g) Kikuchi pattern from A in (f). (h) Kikuchi pattern from B in (f). The EDS map and intensity profile were performed by Nestor Zaluzec.

We also used the fact that the surfactant layers can be damaged by the radiation of the high voltage electron beam in a TEM<sup>151-153</sup>. Therefore, we attempted to expose the bent Au nanorod to a high intensity electron beam of the TEM to damage the surfactant layer. If the bending is released after the surfactant layer is damaged, this could illustrate the effect of the surfactant layer on the bending. The tilting angles of the (100) lattice planes in the Au nanorod before and after exposure to the electron beam were measured using Kikuchi patterns and the results are shown in Figures

9.5 (c) to (h). Before exposure, the Au nanorod was bent with an angle of  $2.81^\circ$ , but after exposure, the symmetry point of the Kikuchi patterns does not move when comparing the patterns from the two ends of the Au nanorod, indicating that the bending angle is  $0^\circ$ . This confirms that the bending disappears after the surfactant layer is damaged by the electron beam. Therefore, the results presented in Figure 9.5 verify that the surfactant layer causes the bending and thereby the lattice strain in the Au nanorod.

Even though we verify the surfactant layer gives rise to the bending of the nanorods, the formation mechanism of the bending is still unclear. The TEM images in other published papers<sup>154-157</sup> show that the contrast is changing in individual Au nanorods stabilized only by CTAB, indicating there is lattice strain in those Au nanorods as well. Studies on the growth mechanism of Au nanorods reveal that the headgroup of CTAB molecules preferentially binds to the gold surface where the atom spacing is comparable to the size of the headgroup of CTAB<sup>33, 158</sup>. This results in an uneven distribution of CTAB molecules on the Au seed surfaces with different lattice indexes, leading to anisotropic growth and formation of Au nanorods. The surfactant mixture of NaOL and CTAB with opposite charges leads to a more complex distribution of the surfactant around the Au nanorods in our work<sup>50</sup>. Therefore, it is reasonable to assume that the CTAB molecules are distributed even more unevenly in the presence of NaOL.

In this chapter, we showed that there is a growth-induced strain in the Au nanorods synthesized with a surfactant mixture of CTAB and NaOL. The strain occurs in the middle section of the Au nanorod and leads to a bending. This bending can be released after the surfactant layer is damaged through exposure to a high voltage the electron beam, verifying the effect of the surfactants on the lattice strain. The cross section of the Au nanorods has clear octagonal shapes, with surface facets consisting of {012} and {013} crystal planes. Moreover, the Ag in the growth solution is found to be uniformly present in the Au lattice and is also present in the surfactant layer surrounding the Au nanorod.



## Chapter 10 Discussion and Conclusions

This entire thesis focuses on the effects of binary capping agent system, surfactant-surfactant and surfactant-polymer mixtures, on the shape of nanoparticles in colloidal nanoparticles synthesis. The research questions raised at the start of the thesis are answered by a series of experiments and analysis.

In order to determine that the shape of metal nanoparticles can be controlled by using a mixture of capping agents, a negatively charged surfactant, NaOL was mixed with either CTAB, CTAC and PVP to synthesize Pd and Au nanoparticles. Since the addition of NaOL molecules changes the micellar structure and surface adsorption of the other capping agents through the introduction of different charges, dendritic shapes of Pd nanoparticles were synthesized successfully by using several capping agent combinations including CTAB-NaOL, CTAC-NaOL and PVP-NaOL. Pd nanodendrites have relatively large surface area, resulting in promising structures for catalytic applications. In this thesis, optimal Pd nanodendrites with high yields and narrow size distribution were produced through control of the synthetic conditions, including the molar ratio between the surfactants, the type of seed particle and Pd precursor, and the pH of the capping agent mixture.

The effects of surfactant molar ratios on the shape of metal nanoparticles were investigated on the Pd nanoparticles stabilized by CTAB and NaOL in the seed-mediated growth process, where Pd nanocubes were used as seeds. It revealed that the shape of Pd nanoparticles was dependent on the surfactant composition. When  $\alpha_{\text{CTAB}}$  equals to 1, there is only CTAB, Pd nanocubes form from Pd cubic seeds; when  $\alpha_{\text{CTAB}}$  is between 0.5 to 0.9, tiny Pd crystals aggregate to form nanodendrites; when  $\alpha_{\text{CTAB}}$  is lower than 0.4, tiny Pd crystals are fabricated in the solution but do not contribute to further growth of the Pd seeds. The optimal condition to obtain Pd nanodendrites is at the  $\alpha_{\text{CTAB}}$  value between 0.8 and 0.9. Additionally, it is verified that both the  $\text{CTA}^+$  ion and the hydrocarbon tail of NaOL, featuring a double bond play crucial roles in the growth of the dendritic shape. The proposed model for the formation of Pd nanodendrites is supported by the experimental results. The addition of NaOL molecules disrupts the continuous CTAB double layer and results in the formation of mixed CTAB-NaOL micelles on the Pd seed surfaces through electrostatic interaction. First,  $\text{Pd}^{2+}$  ions are reduced and form tiny crystals in the mixed CTAB-NaOL micelles and then the crystals are adsorbed on the seed surfaces, which is determined by the interaction strength between the surfactants and the seed surfaces. This interaction decreases with the increase of the NaOL concentration. When  $\alpha_{\text{CTAB}}$  is lower than the critical value 0.4, the interaction is too weak to promote Pd crystal aggregation, resulting in no further growth of the Pd seeds.

The studies of hollow Ag-Pd nanoparticles verify that the type of metal precursors and seeds influences nanoparticle shapes as well. One of the optimal molar ratios

( $\alpha_{\text{CTAC}}=0.8$ ) was applied in the growth of Pd nanodendrites on cubic Ag seeds. The Ag atoms were oxidized to ions during the growth process through a galvanic replacement reaction between the Ag seed and the Pd precursor, forming hollow Ag-Pd nanodendrites. Additionally, hollow Ag-Pd nanoboxes were produced when the Pd precursor ( $\text{H}_2\text{PdCl}_4$ ) was replaced by  $\text{Pd}(\text{acac})_2$ . EDS analysis led to the determination that there are still Ag atoms remaining in the hollow Pd nanoparticles. The atomic percentage of Ag atoms is 48% in hollow nanodendrites and 53% in hollow nanoboxes. The mixed Ag and Pd atoms form an alloy in FCC structures. The lattice constant of the alloy FCC crystals is 0.4047 nm for the Ag-Pd nanodendrite and 0.3991 nm for the nanobox, both of which lie between the constant values for individual Pd and Ag crystals. Additionally, both the spiky tips of the nanobox and the small dendrites of the nanodendrite grew along the (111) lattice plane, the close-packed plane of FCC structure, to achieve a stable state with low energy.

In addition to surfactant-surfactant mixtures, a surfactant-polymer mixture can be employed in the synthesis of metal nanoparticles as well. It is also confirmed that a change of pH values of the surfactant-polymer mixture influences the shape of nanoparticles. PVP is a popular polymer capping agent to synthesize Pd nanocubes. When NaOL molecules were added in the growth process, the shape of Pd nanoparticles was changed to nanodendrites as well. However, the formation of Pd nanodendrites is determined by the pH values of PVP-NaOL mixtures. The optimal Pd nanodendrites with a high yield are achieved at pH 1.17. These nanodendrites consist of several single crystals and twin structures can also be observed. These Pd nanodendrites are also confirmed to have catalytic ability in Sonogashira reactions.

The microstructure study was performed on Au nanorods in detail. The binary surfactant mixture of CTAB and NaOL is used for the synthesis of Au nanorods to increase the rod-shape yield and narrow size distribution. We discovered that growth-induced lattice strain exists in these Au nanorods. The strain occurs in the middle region of the Au nanorod and leads to a bending of the rod shape. This bending is released after the surfactant layer is damaged by exposure to an electron beam, verifying the effects of the surfactant on the lattice strain. These Au nanorods have clear octagonal shapes around the longitudinal axis, which consist of {012} and {013} crystal planes. Moreover, the additional Ag elements in the growth solution were mapped and the distribution occurs symmetrically in the Au lattice and also forms an outer layer around the Au nanorod.

The conclusions from all experiments illustrate that the growth of metal nanoparticles in colloidal nanoparticles synthesis is a complex process. It can be governed by controlling the growth parameters such as types of capping agents, metal precursors and seeds, molar ratios of binary capping agents and pH values. In a proper growth condition, metal nanoparticles with a high yield and uniform shape can be fabricated.

In this thesis, the studies on synthetic methods and microstructures of Pd and Au nanoparticles provide a novel and interesting view for the fundamental research and potential applications in chemistry, physics and biology fields, where nanomaterials are now routinely applied and for other new fields, where nanomaterial research is just beginning.



## References

1. Faraday, M., X. The Bakerian Lecture. —Experimental Relations of Gold (and Other Metals) to Light. *Philosophical Transactions* **1857**, *147*, 145-181.
2. Jeevanandam, J.; Barhoum, A.; Chan, Y. S.; Dufresne, A.; Danquah, M. K., Review on Nanoparticles and Nanostructured Materials: History, Sources, Toxicity and Regulations. *Beilstein Journal of Nanotechnology* **2018**, *9*, 1050–1074.
3. Huang, X.; Neretina, S.; El-Sayed, M. A., Gold Nanorods: From Synthesis and Properties to Biological and Biomedical Applications. *Advanced Materials* **2009**, *21*, 4880–4910.
4. Christensen, S. T.; Elam, J. W.; Rabuffetti, F. A.; Ma, Q.; Weigand, S. J.; Lee, B.; Seifert, S.; Stair, P. C.; Poeppelmeier, K. R.; Hersam, M. C.; Bedzyk, M. J., Controlled Growth of Platinum Nanoparticles on Strontium Titanate Nanocubes by Atomic Layer Deposition. *Small* **2009**, *5* (6), 750-757.
5. Mafuné, F.; Kohno, J.-y.; Takeda, Y.; Kondow, T.; Sawabe, H., Formation and Size Control of Silver Nanoparticles by Laser Ablation in Aqueous Solution. *The Journal of Physical Chemistry B* **2000**, *104* (39), 9111-9117.
6. Mueller, R.; Mädler, L.; E.Pratsinis, S., Nanoparticle Synthesis at High Production Rates by Flame Spray Pyrolysis. *Chemical Engineering Science* **2003**, *58* (10), 1969-1976.
7. An, K.; Alayoglu, S.; Ewers, T.; A.Somorjai, G., Colloid Chemistry of Nanocatalysts: A Molecular View. *Journal of Colloid and Interface Science* **2012**, *373* (1), 1-13.
8. K, H. K.; Venkatesh, N.; Bhowmik, H.; Kuila, A., Metallic Nanoparticle: A Review. *Journal of Scientific & Technical Research* **2018**, *4* (2), 3765-3775.
9. Luther, J. M.; Jain, P. K.; Ewers, T.; Alivisatos, A. P., Localized Surface Plasmon Resonances Arising from Free Carriers in Doped Quantum Dots. *Nature Materials* **2011**, *10*, 361–366.
10. Amendola, V.; Pilot, R.; Frasconi, M.; Maragò, O. M.; Iatì, M. A., Surface Plasmon Resonance in Gold Nanoparticles: A Review. *Journal of Physics: Condensed Matter* **2017**, *29* (20), 203002.
11. Watanabe, S.; Sonobe, M.; Arai, M.; Tazume, Y.; Matsuo, T.; Nakamura, T.; Yoshida, K., Enhanced Optical Sensing of Anions with Amide-Functionalized Gold Nanoparticles. *Chemical Communications* **2002**, 2866-2867.
12. Gavia, D. J.; Shon, D. Y. S., Catalytic Properties of Unsupported Palladium Nanoparticle Surfaces Capped with Small Organic Ligands. *ChemCatChem* **2015**, *7* (6), 892-900.

13. Saldan, I.; Semenyuk, Y.; Marchuk, I.; Reshetnyak, O., Chemical Synthesis and Application of Palladium Nanoparticles. *Journal of Materials Science* **2015**, *50*, 2337–2354.
14. Sawoo, S.; Srimani, D.; Dutta, P.; Lahiri, R.; Sarkar, A., Size Controlled Synthesis of Pd Nanoparticles in Water and Their Catalytic Application in C–C Coupling Reactions. *Tetrahedron* **2009**, *65* (22), 4367-4374.
15. Deraedt, C.; Astruc, D., “Homeopathic” Palladium Nanoparticle Catalysis of Cross Carbon–Carbon Coupling Reactions. *Accounts of Chemical Research* **2014**, *47* (2), 494–503.
16. Khambete, H.; Keservani, R. K.; Kesharwani, R. K.; Jain, N. P.; Jain, C. P., *Nanobiomaterials in Hard Tissue Engineering*. Elsevier: 2016; Vol. 4.
17. R., T. A.; Susan, H.; Peidong, Y., Shape control of colloidal metal nanocrystals. *Small* **2008**, *4* (3), 310-325
18. Cao, J.; Sun, T.; T.V.Grattan, K., Gold Nanorod-Based Localized Surface Plasmon Resonance Biosensors: A Review. *Sensors and Actuators B: Chemical* **2014**, *195*, 332-351.
19. Cheong, S.; Watta, J. D.; Tilley, R. D., Shape control of platinum and palladium nanoparticles for catalysis. *Nanoscale* **2010**, *2*, 2045-2053
20. Sau, T. K.; Rogach, A. L., Nonspherical Noble Metal Nanoparticles: Colloid-Chemical Synthesis and Morphology Control. *Advanced Materials* **2010**, *22* (16), 1781-1804.
21. Dong, X.; Ji, X.; Wu, H.; Zhao, L.; Li, J.; Yang, W., Shape Control of Silver Nanoparticles by Stepwise Citrate Reduction. *The Journal of Physical Chemistry C* **2009**, *113* (16), 6573–6576.
22. Becker, R.; Liedberg, B.; Käll, P.-O., CTAB Promoted Synthesis of Au Nanorods – Temperature Effects and Stability Considerations. *Journal of Colloid and Interface Science* **2010**, *343* (1), 25-30.
23. Ye, X.; Zheng, C.; Chen, J.; Gao, Y.; Murray, C. B., Using Binary Surfactant Mixtures to Simultaneously Improve the Dimensional Tunability and Monodispersity in the Seeded Growth of Gold Nanorods. *Nano Letters* **2013**, *13* (2), 765–771.
24. Auffan, M.; Rose, J.; Bottero, J.-Y.; Lowry, G. V.; Jolivet, J.-P.; Wiesner, M. R., Towards a Definition of Inorganic Nanoparticles from an Environmental, Health and Safety Perspective. *Nature Nanotechnology* **2009**, *4*, 634–641.
25. Azharuddin, M.; Zhu, G. H.; Das, D.; Ozgur, E.; Uzun, L.; Turner, A. P. F.; Patra, H. K., A Repertoire of Biomedical Applications of Noble Metal Nanoparticles *Chemical Communications* **2019**, *55*, 6964-6996.
26. Sau, T. K.; Rogach, A. L.; Jäckel, F.; Klar, T. A.; Feldmann, J., Properties and Applications of Colloidal Nonspherical Noble Metal Nanoparticles. *Advanced Materials* **2010**, *22* (16), 1805-1825.

27. Kelly, J. A.; Shopsowitz, K. E.; Ahn, J. M.; Hamad, W. Y.; MacLachlan, M. J., Chiral Nematic Stained Glass: Controlling the Optical Properties of Nanocrystalline Cellulose-Templated Materials. *Langmuir* **2012**, *28* (50), 17256–17262.
28. Chugh, H.; Sood, D.; Chandra, I.; Tomar, V.; Dhawan, G.; Chandra, R., Role of Gold and Silver Nanoparticles in Cancer Nano-Medicine. *Artificial Cells, Nanomedicine, and Biotechnology* **2018**, *46* (1), 1210-1220.
29. Tsai, S. C.; Song, Y. L.; Tsai, C. S.; Yang, C. C.; Chiu, W. Y.; Lin, H. M., Ultrasonic Spray Pyrolysis for Nanoparticles Synthesis. *Journal of Materials Science* **2004**, *39*, 3647-3657.
30. Jana, N. R.; Gearheart, L.; Murphy, C. J., Seed-mediated Growth Approach for Shape-controlled Synthesis of Spheroidal and Rod-like Gold Nanoparticles Using a Surfactant Template. *Advanced Materials* **2001**, *13*, 1389-1393.
31. Ibupoto, Z. H.; Khun, K.; Liu, X.; Willander, M., Low Temperature Synthesis of Seed Mediated CuO Bundle of Nanowires, Their Structural Characterisation and Cholesterol Detection. *Materials Science and Engineering: C* **2013**, *33* (7), 3889-3898.
32. Niu, W.; Zhang, L.; Xu, G., Seed-mediated Growth of Noble Metal Nanocrystals: Crystal Growth and Shape Control. *Nanoscale* **2013**, *5*, 3172-3181.
33. Nikoobakht, B.; El-Sayed, M. A., Preparation and Growth Mechanism of Gold Nanorods (NRs) Using Seed-Mediated Growth Method. *Chemistry of Materials* **2003**, *15* (10), 1957-1962.
34. Wang, Y.-N.; Wei, W.-T.; Yang, C.-W.; Huang, M. H., Seed-Mediated Growth of Ultralong Gold Nanorods and Nanowires with a Wide Range of Length Tunability. *Langmuir* **2013**, *29* (33), 10491-10497.
35. Smith, D. K.; Korgel, B. A., The Importance of the CTAB Surfactant on the Colloidal Seed-Mediated Synthesis of Gold Nanorods. *Langmuir* **2008**, *24*, 644-649.
36. Gavia, D. J.; Shon, Y. S., Catalytic Properties of Unsupported Palladium Nanoparticle Surfaces Capped with Small Organic Ligands. *ChemCatChem* **2015**, *7*, 892-900.
37. Crooks, R. M.; Zhao, M.; Sun, L.; Chechik, V.; Yeung, L. K., Dendrimer-Encapsulated Metal Nanoparticles: Synthesis, Characterization, and Applications to Catalysis. *Accounts of Chemical Research* **2001**, *34* (3), 181-190.
38. Wang, H.; Qiao, X.; Chen, J.; Wang, X.; Ding, S., Mechanisms of PVP in the Preparation of Silver Nanoparticles. *Materials Chemistry and Physics* **2005**, *94* (2-3), 449-453.

39. Xu, Y.; Chen, L.; Ye, X.; Wang, X.; Yu, J.; Zhao, Y.; Cao, M.; Xia, Z.; Sun, B.; Zhang, Q., Cooperative Interactions Among CTA<sup>+</sup>, Br<sup>-</sup> and Ag<sup>+</sup> During Seeded Growth of Gold Nanorods. *Nano Research* **2017**, *10* (6), 2146–2155.
40. Fan, F.-R.; Attia, A.; Sur, U. K.; Chen, J.-B.; Xie, Z.-X.; Li, J.-F.; Ren, B.; Tian, Z.-Q., An Effective Strategy for Room-Temperature Synthesis of Single-Crystalline Palladium Nanocubes and Nanodendrites in Aqueous Solution. *Crystal Growth and Design* **2009**, *9* (5), 2335–2340.
41. Zhang, L.; Wang, L.; Jiang, Z.; Xie, Z., Synthesis of Size-Controlled Monodisperse Pd Nanoparticles via a Non-Aqueous Seed-Mediated Growth. *Nanoscale Research Letters* **2012**, *7*, 312.
42. Koebel, M. M.; Jones, L. C.; Somorjai, G. A., Preparation of Size-Tunable, Highly Monodisperse PVP-Protected Pt-Nanoparticles by Seed-Mediated Growth. *Journal of Nanoparticle Research* **2008**, *10*, 1063–1069.
43. Xia, Y.; Gilroy, K. D.; Peng, H.-C.; Xia, X., Seed-Mediated Growth of Colloidal Metal Nanocrystals. *Angewandte Chemie International Edition* **2017**, *56* (1), 60-95.
44. Gole, A.; Murphy, C. J., Seed-Mediated Synthesis of Gold Nanorods: Role of the Size and Nature of the Seed. *Chemistry of Materials* **2004**, *16* (19), 3633-3640.
45. Xu, Z.; Wei, Z.; He, P.; Duan, X.; Yang, Z.; Zhou, Y.; Jia, D., Seed-mediated growth of ultra-thin triangular magnetite nanoplates *Chemical Communications* **2017**, *53*, 11052--11055.
46. Zhang, Q.; Li, W.; Moran, C.; Zeng, J.; Chen, J.; Wen, L.; Xia, Y., Seed-Mediated Synthesis of Ag Nanocubes with Controllable Edge Lengths in the Range of 30–200 nm and Comparison of Their Optical Properties. *Journal of American Chemical Society* **2010**, *132* (32), 11372-11378.
47. Guerrero-Martínez, A.; Barbosa, S.; Pastoriza-Santos, I.; Liz-Marzán, L. M., Nanostars shine bright for you: Colloidal synthesis, properties and applications of branched metallic nanoparticles. *Current Opinion in Colloid & Interface Science* **2011**, *16* (2), 118-127.
48. Lu, L.; Wang, H.; Zhou, Y.; Xi, S.; Zhang, H.; Hu, J.; BingZhao, Seed-mediated Growth of Large, Monodisperse Core–Shell Gold–Silver Nanoparticles with Ag-Like Optical Properties. *Chemical Communications* **2002**, (2), 144-145.
49. Kumar-Krishnan, S.; Estevez-González, M.; Pérez, R.; Esparza, R.; Meyyappan, M., A General Seed-Mediated Approach to the Synthesis of AgM (M = Au, Pt, and Pd) Core–Shell Nanoplates and Their SERS Properties. *RSC Advances* **2017**, *7* (44), 27170-27176
50. Wen, X.; Lerch, S.; Wang, Z.; Aboudiab, B.; Tehrani-Bagha, A. R.; Olsson, E.; Moth-Poulsen, K., Synthesis of Palladium Nanodendrites Using a Mixture of Cationic and Anionic Surfactants. *Langmuir* **2020**, *36* (7), 1745-1753.

51. Chaudhuri, R. G.; Paria, S., Core/Shell Nanoparticles: Classes, Properties, Synthesis Mechanisms, Characterization, and Applications. *Chemical Reviews* **2012**, *112* (4), 2373–2433.
52. Chaudhuri, R. G.; Paria, S., Core/Shell Nanoparticles: Classes, Properties, Synthesis Mechanisms, Characterization, and Applications. *Chemical Reviews* **2012**, *112* (4), 2373–2433.
53. Chen, L.; Huang, B.; Qiu, X.; Wang, X.; Luque, R.; Li, Y., Seed-Mediated Growth of MOF-Encapsulated Pd@Ag Core–Shell Nanoparticles: Toward Advanced Room Temperature Nanocatalysts. *Chemical Science* **2016**, *7*, 228–233.
54. Huang, C. C.; Yang, Z.; Chang, H. T., Synthesis of Dumbbell-Shaped Au–Ag Core–Shell Nanorods by Seed-Mediated Growth under Alkaline Conditions. *Langmuir* **2004**, *20* (15), 6089–6092.
55. Wang, L.; Yamauchi, Y., Autoprogrammed Synthesis of Triple-Layered Au@Pd@Pt Core–Shell Nanoparticles Consisting of a Au@Pd Bimetallic Core and Nanoporous Pt Shell. *Journal of the American Chemical Society* **2010**, *132* (39), 13636–13638.
56. Liu, X.; Liu, X., Bimetallic Nanoparticles: Kinetic Control Matters. *Angewandte Chemie International Edition* **2012**, *51* (14), 3311–3313.
57. DeSantis, C. J.; Sue, A. C.; Bower, M. M.; Skrabalak, S. E., Seed-Mediated Co-reduction: A Versatile Route to Architecturally Controlled Bimetallic Nanostructures. *ACS Nano* **2012**, *6* (3), 2617–2628.
58. Sui, N.; Wang, K.; Shan, X.; Bai, Q.; Wang, L.; Xiao, H.; Liu, M.; Colvin, V. L.; Yu, W. W., Facile Synthesis of Hollow Dendritic Ag/Pt Alloy Nanoparticles for Enhanced Methanol Oxidation Efficiency. *Dalton Transactions* **2017**, *46* (44), 15541–15548.
59. Richard-Daniel, J.; Boudreau, D., Enhancing Galvanic Replacement in Plasmonic Hollow Nanoparticles: Understanding the Role of the Speciation of Metal Ion Precursors. *Chemistry of Nanomaterials for Energy, Biology and More* **2020**, *6*, 1–10.
60. Liu, H.; Qu, J.; Chen, Y.; Li, J.; Ye, F.; Lee, J. Y.; Yang, J., Hollow and Cage-Bell Structured Nanomaterials of Noble Metals. *Journal of the American Chemical Society* **2012**, *134* (28), 11602–11610.
61. Goodman, A. M.; Cao, Y.; Urban, C.; Neumann, O.; Ayala-Orozco, C.; Knight, M. W.; Joshi, A.; Nordlander, P.; Halas, N. J., The Surprising in Vivo Instability of Near-IR-Absorbing Hollow Au–Ag Nanoshells. *ACS Nano* **2014**, *8* (4), 3222–3231.
62. Kim, S. J.; Ah, C. S.; Jang, D. J., Optical Fabrication of Hollow Platinum Nanospheres by Excavating the Silver Core of Ag@Pt Nanoparticles. *Advanced Materials* **2007**, *19* (8), 1064–1068.

63. Chen, L.; Ji, F.; Xu, Y.; He, L.; Mi, Y.; Bao, F.; Sun, B.; Zhang, X.; Zhang, Q., High-Yield Seedless Synthesis of Triangular Gold Nanoplates through Oxidative Etching. *Nano Letters* **2014**, *14* (12), 7201–7206.
64. Liopo, A.; Wang, S.; Derry, P. J.; Oraevsky, A. A.; Zubarev, E. R., Seedless Synthesis of Gold Nanorods Using Dopamine as a Reducing Agent. *RSC Advances* **2015**, *5*, 91587-91593
65. Ostwald, W., Über die vermeintliche Isomerie des roten und gelben Quecksilberoxyds und die Oberflächenspannung fester Körper. *Z. Phys. Chem.* **1900**, *34*, 495.
66. Volmer, M.; Weber, A., Keimbildung in übersättigten Gebilden. *Z Phys. Chem.* **1926**, *119*, 277-301.
67. Becker, R.; Döring, W., Kinetische behandlung der keimbildung in übersättigten dämpfen. *Annalen der Physik* **1935**, *416* (8), 719-752.
68. Frenkel, Y. I., *Kinetic Theory of Liquids*. Dover: 1955; p 500.
69. LaMer, V. K.; Dinegar, R. H., Theory, Production and Mechanism of Formation of Monodispersed Hydrosols. *Journal of the American Chemical Society* **1950**, *72* (11), 4847–4854.
70. Thanh, N. T. K.; Maclean, N.; Mahiddine, S., Mechanisms of Nucleation and Growth of Nanoparticles in Solution. *Chemical Reviews* **2014**, *114* (15), 7610–7630.
71. Polte, J., Fundamental Growth Principles of Colloidal Metal Nanoparticles – A New Perspective. *CrystEngComm* **2015**, *17*, 6809-6830.
72. Karthika, S.; Radhakrishnan, T. K.; Kalachelvi, P., A Review of Classical and Nonclassical Nucleation Theories. *Crystal Growth & Design* **2016**, *16* (11), 6663–6681.
73. Mer, V. K. L., Nucleation in Phase Transitions. *Industrial and Engineering Chemistry* **1952**, *44* (6), 1270-1277.
74. Niederberger, M.; Cölfen, H., Oriented Attachment and Mesocrystals: Non-Classical Crystallization Mechanisms Based on Nanoparticle Assembly. *Phys. Chem. Chem. Phys.* **2006**, *8*, 3271-3287.
75. Zheng, H.; Smith, R. K.; Jun, Y. w.; Kisielowski, C.; Dahmen, U.; Alivisatos, A. P., Observation of Single Colloidal Platinum Nanocrystal Growth Trajectories. *Science* **2009**, *324* (5932), 1309-1312.
76. Peng, Z. A.; Peng, X., Mechanisms of the Shape Evolution of CdSe Nanocrystals. *Journal of American Chemical Society* **2001**, *123* (7), 1389–1395.
77. Watzky, M. A.; Finke, R. G., Transition Metal Nanocluster Formation Kinetic and Mechanistic Studies. A New Mechanism When Hydrogen Is the Reductant: Slow, Continuous Nucleation and Fast Autocatalytic Surface Growth. *Journal of the American Chemical Society* **1997**, *119* (43), 10382–10400.

78. Watzky, M. A.; Finke, R. G., Nanocluster Size-Control and “Magic Number” Investigations. Experimental Tests of the “Living-Metal Polymer” Concept and of Mechanism-Based Size-Control Predictions Leading to the Syntheses of Iridium(0) Nanoclusters Centering about Four Sequential Magic Numbers†. *Chemistry of Materials* **1997**, *9* (12), 3083–3095.
79. Sherry, L. J.; Jin, R.; Mirkin, C. A.; Schatz, G. C.; Duyne, R. P. V., Localized Surface Plasmon Resonance Spectroscopy of Single Silver Triangular Nanoprisms. *Nano Letters* **2006**, *6* (9), 2060–2065.
80. Petryayeva, E.; Krull, U. J., Localized Surface Plasmon Resonance: Nanostructures, Bioassays and Biosensing—A review. *Analytica Chimica Acta* **2011**, *706* (1), 8-24.
81. Heck, R. F.; Negishi, E.-i.; Suzuki, A., The Nobel Prize. The Royal Swedish Academy of Sciences: Sweden, 2010.
82. Yin, L.; Liebscher, J., Carbon–Carbon Coupling Reactions Catalyzed by Heterogeneous Palladium Catalysts. *Chemical Reviews* **2007**, *107* (1), 133-173.
83. Sonogashira, K., Development of Pd–Cu Catalyzed Cross-Coupling of Terminal Acetylenes with  $sp^2$ -Carbon Halides. *Journal of Organometallic Chemistry* **2002**, *653* (1-2), 46-49.
84. Chinchilla, R.; Nájera, C., The Sonogashira Reaction: A Booming Methodology in Synthetic Organic Chemistry. *Chemical Reviews* **2007**, *107* (3), 874-922.
85. Chinchilla, R.; Nájera, C., Recent Advances in Sonogashira Reactions. *Chem. Soc. Rev.* **2011**, *40*, 5084-5121.
86. Schramm, L. L.; Stasiuk, E. N.; Marangoni, D. G., Surfactants and Their Applications *Annual Reports Section "C" (Physical Chemistry)* **2003**, *99*, 3-48.
87. Hong, C. R.; Park, S. J.; Choi, S. J., Influence of the Hydrophilic Head Size and Hydrophobic Tail Length of Surfactants on the Ability of Micelles to Stabilize Citral. *Journal of the Science of Food and Agriculture* **2016**, *96* (9), 3227-3232.
88. Kronberg, B.; Holmberg, K.; Lindman, B., *Surface Chemistry of Surfactants and Polymers*. Wiley: 2014.
89. Nesměrák, K.; Němcová, I., Determination of Critical Micelle Concentration by Electrochemical Means. *Analytical Letters* **2006**, *39* (6), 1023-1040.
90. A.Khalil, R.; A.Zarari, A.-h., Theoretical Estimation of the Critical Packing Parameter of Amphiphilic Self-Assembled Aggregates. *Applied Surface Science* **2014**, *318*, 85-89.
91. Nakama, Y., *Cosmetic Science and Technology: Theoretical Principles and Applications* Elsevier Science: 2017; p 854.

92. Griffin, W. C., Classification of Surface-Active Agents by 'HLB'. *Journal of the Society of Cosmetic Chemists* **1949**, *1* (5), 311–326.
93. Griffin, W. C., Calculation of HLB Values of Non-Ionic Surfactants. *Journal of the Society of Cosmetic Chemists* **1954**, *5* (4), 249–256.
94. Haaf, F.; Sanner, A.; Straub, F., Polymers of N-Vinylpyrrolidone: Synthesis, Characterization and Uses. *Polymer Journal* **1985**, *17*, 143-152.
95. Guettari, M.; Belaidi, A.; Abel, S.; Tajouri, T., Polyvinylpyrrolidone Behavior in Water/Ethanol Mixed Solvents: Comparison of Modeling Predictions with Experimental Results. *Journal of Solution Chemistry* **2017**, *46*, 1404–1417.
96. Koczur, K. M.; Mourdikoudis, S.; Polavarapu, L.; Skrabalak, S. E., Polyvinylpyrrolidone (PVP) in Nanoparticle Synthesis *Dalton Transactions* **2015**, *44* (41), 17883-17905
97. Ma, C.; Li, C., Interaction between Polyvinylpyrrolidone and Sodium Dodecyl Sulfate at Solid/Liquid Interface. *Journal of Colloid and Interface Science* **1989**, *131* (2), 485-492.
98. Williams, D. B.; Carter, C. B., *Transmission Electron Microscopy: A Textbook for Materials Science*. Springer: 1996; p 775.
99. Hren, J. J.; Goldstein, J. I.; Joy, D. C., *Introduction to Analytical Electron Microscopy*. Springer: 1979; p 601.
100. Kartini, I.; Meredith, P.; Costa, J. C. D. D.; Lu, G. Q., A Novel Route to the Synthesis of Mesoporous Titania with Full Anatase Nanocrystalline Domains. *Journal of Sol-Gel Science and Technology* **2004**, *31*, 185–189.
101. L., R.; Wal, V., Soot Precursor Carbonization: Visualization Using LIF and LII and Comparison Using Bright and Dark Field TEM. *Combustion and Flame* **1998**, *112* (4), 607-616.
102. Zachman, M. J.; Tu, Z.; Choudhury, S.; Archer, L. A.; Kourkoutis, L. F., Cryo-STEM Mapping of Solid–Liquid Interfaces and Dendrites in Lithium-Metal Batteries. *Nature* **2018**, *560*, 345–349.
103. Zaeferrer, S., On the Formation Mechanisms, Spatial Resolution and Intensity of Backscatter Kikuchi Patterns. *Ultramicroscopy* **2007**, *107* (2-3), 254-266.
104. Kainuma, Y., The Theory of Kikuchi Patterns. *Acta Crystallographica* **1955**, *8*, 247-257.
105. Young, C. T.; Steele, J. H.; Lytton, J. L., Characterization of Bicrystals Using Kikuchi Patterns. *Metallurgical Transactions* **1973**, *4*, 2081–2089.
106. Levine, E.; Bell, W. L.; Thomas, G., Further Applications of Kikuchi Diffraction Patterns; Kikuchi Maps *Journal of Applied Physics* **1966**, *37* (5), 2141-2148.
107. Pennycook, S. J.; Jesson, D. E., High-Resolution Z-contrast Imaging of Crystals. *Ultramicroscopy* **1991**, *37* (1-4), 14-38.

108. Findlay, S. D.; Shibata, N.; Sawada, H.; Okunishi, E.; Kondo, Y.; Ikuhara, Y., Dynamics of Annular Bright Field Imaging in Scanning Transmission Electron Microscopy. *Ultramicroscopy* **2010**, *110* (7), 903-923.
109. Jiang, N., Electron Beam Damage in Oxides: A Review. *Reports on Progress in Physics* **2016**, *79* (1), 016501.
110. Egerton, R. F., Outrun Radiation Damage with Electrons? *Advanced Structural and Chemical Imaging* **2015**, *1*, 5.
111. Kotakoski, J.; Jin, C. H.; Lehtinen, O.; Suenaga, K.; Krasheninnikov, A. V., Electron Knock-On Damage in Hexagonal Boron Nitride Monolayers. *Physical Review B* **2010**, *82* (11), 113404.
112. Egerton, R. F.; Li, P.; Malac, M., Radiation Damage in the TEM and SEM. *Micron* **2004**, *35* (6), 399-409.
113. Smeeton, T. M.; Kappers, M. J.; Barnard, J. S.; Vickers, M. E.; Humphreys, C. J., Electron-Beam-Induced Strain within InGaN Quantum Wells: False Indium "Cluster" Detection in the Transmission Electron Microscope *Applied Physics Letters* **2003**, *83*, 5419.
114. Matsui, S.; Ichihashi, T., In Situ Observation on Electron-Beam-Induced Chemical Vapor Deposition by Transmission Electron Microscopy *Applied Physics Letters* **1988**, *53*, 842.
115. Niu, W.; Zhang, L.; Xu, G., Shape-Controlled Synthesis of Single-Crystalline Palladium Nanocrystals. *ACS Nano* **2010**, *4* (4), 1987-1996.
116. Liu, J.; Lu, Y., Preparation of Aptamer-Linked Gold Nanoparticle Purple Aggregates for Colorimetric Sensing of Analytes. *Nature Protocols* **2006**, *1* (1), 246-252.
117. Zhang, Q.; Li, W.; Wen, L.-P.; Chen, J.; Xia, Y., Facile Synthesis of Ag Nanocubes of 30 to 70 nm in Edge Length with CF<sub>3</sub>COOAg as a Precursor. *Chemistry A European Journal* **2010**, *16* (33), 10234-10239.
118. Wang, Y.; Zheng, Y.; Huang, C. Z.; Xia, Y., Synthesis of Ag Nanocubes 18–32 nm in Edge Length: The Effects of Polyol on Reduction Kinetics, Size Control, and Reproducibility. *Journal of the American Chemical Society* **2013**, *135* (5), 1941-1951.
119. Kulkarni, V. S., *Handbook of Non-Invasive Drug Delivery Systems*. Elsevier: 2010.
120. Jiang, J.; Oberdorster, G.; Biswas, P., Characterization of Size, Surface Charge, and Agglomerationstate of Nanoparticle Dispersions for Toxicological Studies. *Journal of Nanoparticle Research* **2009**, *11*, 77-89.
121. Bhattacharjee, S., DLS and Zeta Potential—What They Are and What They Are Not? *Journal of Controlled Release* **2016**, *235*, 337-351.
122. Niu, W.; Li, Z.-Y.; Shi, L.; Liu, X.; Li, H.; Han, S.; Chen, J.; Xu, G., Seed-Mediated Growth of Nearly Monodisperse Palladium Nanocubes with Controllable Sizes. *Crystal Growth & Design* **2008**, *8* (12), 4440-4444.

123. Xu, R.; Wu, C.; Haiyan Xu, Particle Size and Zeta Potential of Carbon Black in Liquid Media. *Carbon* **2007**, *45* (14), 2806-2809.
124. Kume, G.; Gallotti, M.; Nunes, G., Review on Anionic/Cationic Surfactant Mixtures. *Journal of Surfactants and Detergents* **2008**, *11* (1), 1-11.
125. Louie, S. G., Electronic States and Adsorbate-induced Photoemission Structure on the Pd (111) Surface. *Physical Review Letters* **1978**, *40* (23), 1525-1528.
126. Manojlovic, J. Ž., The Krafft Temperature of Surfactant Solutions. *Thermal Science* **2012**, *16*, 631-640.
127. McBain, J. W.; Sierichs, W. C., The Solubility of Sodium and Potassium Soaps and the Phase Diagrams of Aqueous Potassium Soaps. *Journal of the American Oil Chemists Society* **1948**, *25* (6), 221-225.
128. Moroi, Y.; Matuura, R.; Kuwamura, T.; Inokuma, S. I., Anionic Surfactants with Divalent Gegenions of Separate Electric Charge: Solubility and Micelle Formation. *Journal of Colloid and Interface Science* **1986**, *113* (1), 225-231.
129. Miraglia, D. B.; Rodríguez, J. L. R.; Minardi, R. M.; Schulz, P. C., Critical Micelle Concentration and HLB of the Sodium Oleate-Hexadecyltrimethylammonium Bromide Mixed System. *Journal of Surfactants and Detergents* **2011**, *14* (3), 401-408.
130. Kadi, N. E.; Martins, F.; Clausse, D. I.; Schulz, P. C., Critical Micelle Concentrations of Aqueous Hexadecyltrimethylammonium Bromide-sodium Oleate Mixtures. *Colloid and Polymer Science* **2003**, *281*, 353-362.
131. Miraglia, D. B.; Rodríguez, J. L.; Minardi, R. M.; Schulz, P. C., Critical Micelle Concentration and HLB of the Sodium Oleate-Hexadecyltrimethylammonium Bromide Mixed System. *Journal of Surfactants and Detergents* **2011**, *14*, 401-408.
132. Mukerjee, P.; Mysels, K. J., *Critical Micelle Concentrations of Aqueous Surfactant Systems*. Elsevier: Journal of Pharmaceutical Sciences, 1971; Vol. 61.
133. Akhter, M. S., Effect of Acetamide on the Critical Micelle Concentration of Aqueous Solutions of Some Surfactants. *Colloids and Surfaces A: Physicochemical and Engineering Aspects* **1997**, *121* (2-3), 103-109.
134. Pluciński, P. K., The Influence of Solubilization upon the Permeation of Aromatic Hydrocarbons through Liquid Membranes. *Journal of Membrane Science* **1985**, *23*, 105-109.
135. Wei, Z.; Matsui, H., Rational Strategy for Shaped Nanomaterial Synthesis in Reverse Micelle Reactors. *Nature Communications* **2014**, *5* (3870), 1-8.
136. Sun, Y.; Zhang, L.; Zhou, H.; Zhu, Y.; Sutter, E.; Ji, Y.; Rafailovich, M. H.; Sokolov, J. C., Seedless and Templateless Synthesis of Rectangular Palladium Nanoparticles. *Chemistry of Materials* **2007**, *19* (8), 2065-2070.

137. Huang, Y.; Ferhan, A. R.; Dandapat, A.; Yoon, C. S.; Song, J. E.; Cho, E. C.; Kim, D.-H., A Strategy for the Formation of Gold–Palladium Supra-Nanoparticles from Gold Nanoparticles of Various Shapes and Their Application to High-Performance H<sub>2</sub>O<sub>2</sub> Sensing. *The Journal of Physical Chemistry C* **2015**, *119*, 26164–26170.
138. Peng, H.-C.; Xie, S.; Park, J.; Xia, X.; Xia, Y., Quantitative Analysis of the Coverage Density of Br<sup>-</sup> Ions on Pd{100} Facets and Its Role in Controlling the Shape of Pd Nanocrystals. *Journal of the American Chemical Society* **2013**, *135* (10), 3780–3783.
139. Mickymaray, S., One-step Synthesis of Silver Nanoparticles Using Saudi Arabian Desert Seasonal Plant *Sisymbrium irio* and Antibacterial Activity Against Multidrug-Resistant Bacterial Strains. *Biomolecules* **2019**, *9* (11), 662.
140. Fu, B.; Liu, W.; Li, Z., Calculation of the Surface Energy of FCC-Metals with the Empirical Electron Surface Model. *Applied Surface Science* **2010**, *256* (22), 6899-6907.
141. Jian-Min, Z.; Fei, M.; Ke-Wei, X., Calculation of the Surface Energy of FCC Metals with Modified Embedded-Atom Method. *Chinese Physics* **2004**, *13* (7), 1082-1090.
142. Synthesis of Nanocrystalline Ag-Pd Alloys by Chemical Reduction Method. *Nanostructured Materials* **1998**, *10* (8), 1393-1400.
143. Li, Y.; Boone, E.; El-Sayed, M. A., Size Effects of PVP–Pd Nanoparticles on the Catalytic Suzuki Reactions in Aqueous Solution. *Langmuir* **2002**, *18* (12), 4921–4925.
144. Zhao, Y.; Baeza, J. A.; Rao, N. K.; Calvo, L.; Gilarranz, M. A.; Li, Y. D.; Lefferts, L., Unsupported PVA- and PVP-stabilized Pd nanoparticles as catalyst for nitrite hydrogenation in aqueous phase. *Journal of Catalysis* **2014**, *318*, 162-169.
145. Sau, T. K.; Murphy, C. J., Seeded High Yield Synthesis of Short Au Nanorods in Aqueous Solution. *Langmuir* **2004**, *20* (15), 6414–6420.
146. Pingel, T. N.; Jørgensen, M.; Yankovich, A. B.; Grönbeck, H.; Olsson, E., Influence of Atomic Site-Specific Strain on Catalytic Activity of Supported Nanoparticles. *Nature Communications* **2018**, *9*, 2722.
147. Sneed, B. T.; Young, A. P.; Tsung, C.-K., Building Up Strain in Colloidal Metal Nanoparticle Catalysts. *Nanoscale* **2015**, *7* (29), 12248-12265.
148. Link, S.; El-Sayed, M. A., Spectral Properties and Relaxation Dynamics of Surface Plasmon Electronic Oscillations in Gold and Silver Nanodots and Nanorods. *The Journal of Physical Chemistry B* **1999**, *103* (40), 8410-8426.
149. Link, S.; El-Sayed, M. A., Shape and Size Dependence of Radiative, Non-Radiative and Photothermal Properties of Gold Nanocrystals. *International Reviews in Physical Chemistry* **2000**, *19* (3), 409-453.

150. Gómez-Graña, S.; Hubert, F.; Testard, F.; Guerrero-Martínez, A.; Grillo, I.; Liz-Marzán, L. M.; Spalla, O., Surfactant (Bi)Layers on Gold Nanorods. *Langmuir* **2012**, *28* (2), 1453-1459.
151. Albrecht, W.; Glind, A. v. d.; Yoshida, H.; Isozaki, Y.; Imhof, A.; Blaaderen, A. v.; Jongh, P. E. d.; Jong, K. P. d.; Zečević, J.; Takeda, S., Impact of The Electron Beam on The Thermal Stability of Gold Nanorods Studied by Environmental Transmission Electron Microscopy. *Ultramicroscopy* **2018**, *193*, 97-103.
152. Azcárate, J. C.; Fonticelli, M. H.; Zelaya, E., Radiation Damage Mechanisms of Monolayer-Protected Nanoparticles via TEM Analysis. *The Journal of Physical Chemistry C* **2017**, *121* (46), 26108-26116.
153. Egerton, R. F., Mechanisms of Radiation Damage in Beam-Sensitive Specimens, for TEM Accelerating Voltages Between 10 and 300 kV. *Microscopy Research and Technique* **2012**, *75* (11), 1550–1556.
154. Tsung, C.-K.; Kou, X.; Shi, Q.; Zhang, J.; Yeung, M. H.; Wang, J.; Stucky, G. D., Selective Shortening of Single-Crystalline Gold Nanorods by Mild Oxidation. *Journal of the American Chemical Society* **2006**, *128* (16), 5352-5353.
155. Vigdeman, L.; Zubarev, E. R., High-Yield Synthesis of Gold Nanorods with Longitudinal SPR Peak Greater than 1200 nm Using Hydroquinone as a Reducing Agent. *Chemistry of Materials* **2013**, *25* (8), 1450-1457.
156. Ma, X.; Wang, M.-C.; Feng, J.; Zhao, X., Effect of Solution Volume Covariation on the Growth Mechanism of Au Nanorods Using the Seed-Mediated Method. *Acta Materialia* **2015**, *85*, 322-330.
157. Zhang, Q.; Jing, H.; Li, G. G.; Lin, Y.; Blom, D. A.; Wang, H., Intertwining Roles of Silver Ions, Surfactants, and Reducing Agents in Gold Nanorod Overgrowth: Pathway Switch between Silver Underpotential Deposition and Gold–Silver Codeposition. *Chemistry of Materials* **2016**, *28* (8), 2728–2741.
158. Murphy, C. J.; Sau, T. K.; Gole, A. M.; Orendorff, C. J.; Gao, J.; Gou, L.; Hunyadi, S. E.; Li, T., Anisotropic Metal Nanoparticles: Synthesis, Assembly, and Optical Applications. *The Journal of Physical Chemistry B* **2005**, *109* (29), 13857-13870.